ATLAS NOTE

ATLAS-CONF-2016-104

28th September 2016

Search for new phenomena in $t\bar{t}$ final states with additional heavy-flavour jets in 13.2 fb^{-1} of pp collisions at $\sqrt{s}$ = 13 TeV with the ATLAS detector

The ATLAS Collaboration

Abstract

A search for new phenomena in $t\bar{t}$ final states with additional heavy-flavour jets is presented. The search targets a variety of signals, including the pair production of a vector-like top quark (T) with a significant branching ratio to a top quark and either a Standard Model Higgs boson or a Z boson; four-top-quark production, both within the Standard Model and in several new physics scenarios; and heavy Higgs bosons (neutral and charged) produced in association with, and decaying into, third generation quarks. The analysis uses pp collisions at $\sqrt{s}$ = 13 TeV recorded in 2015 and 2016 with the ATLAS detector at the CERN Large Hadron Collider. The dataset corresponds to an integrated luminosity of 13.2 fb^{-1}. Data are analysed in the lepton-plus-jets final state, characterised by an isolated electron or muon with high transverse momentum, large missing transverse momentum and multiple jets, as well as the jets+$E_{\mathrm{T}}^{\mathrm{miss}}$ final state, characterised by multiple jets and large missing transverse momentum. The search exploits the high multiplicity of b-jets, the high scalar sum of transverse momenta of all final state objects, and the presence of boosted, hadronically-decaying resonances reconstructed as large-radius jets characteristic of signal events. In the absence of a significant excess above the Standard Model expectation, 95% CL upper limits are derived for the signal models in a number of benchmark scenarios, in most cases significantly extending the reach of previous searches.

ATLAS-CONF-2016-104
29 September 2016

1. Introduction

The discovery of a new particle consistent with the Standard Model (SM) Higgs boson by the ATLAS [1] and CMS [2] collaborations is a major milestone in high-energy physics. However, the underlying nature of electroweak symmetry breaking (EWSB) remains unknown. Naturalness arguments [3] require that quadratic divergences that arise from radiative corrections to the Higgs boson mass must be cancelled by some new mechanism in order to avoid fine-tuning. To that effect, several explanations have been proposed in theories beyond the SM (BSM). In Supersymmetry [4–6], the cancellation comes from assigning superpartners to the SM bosons and fermions. A common prediction of supersymmetric models, as in many other BSM scenarios, is the presence of an extended Higgs sector.

Alternatively, Little Higgs [7, 8] and Composite Higgs [9, 10] models introduce a spontaneously broken global symmetry, with the Higgs boson emerging as a pseudo–Nambu–Goldstone boson [11]. Such models predict the existence of vector-like quarks, defined as colour-triplet spin-1/2 fermions whose left- and right-handed chiral components have the same transformation properties under the weak-isospin SU(2) gauge group [12, 13]. In these models vector-like quarks are expected to couple preferentially to third-generation quarks [12, 14] and they can have flavour-changing neutral current decays, in addition to the charged-current decays characteristic of chiral quarks. As a result, an up-type quark T with charge $+2/3$ can decay not only to a W boson and a b-quark, but also to a Higgs or Z boson and a top quark ($T \to Wb$, Zt, and Ht). Similarly, a down-type quark B with charge $-1/3$ can decay to a Higgs or Z boson and a b-quark, in addition to decaying to a W boson and a top quark ($B \to Wt$, Zb, and Hb). In order to be consistent with the results from the precision electroweak measurements, a small mass splitting between vector-like quarks belonging to the same SU(2) multiplet is required [15], which forbids cascade decays such as $T \to WB$ and leaves direct decays into SM particles as the only possibility. Couplings between the vector-like quarks and the first and second quark generations, although not favoured, are not excluded [16, 17]. This leads to a rich phenomenology at the LHC, which the experiments are investigating.

Using the Run 1 dataset, the ATLAS and CMS collaborations have carried out a broad program of searches for pair production of a vector-like T quark, $T\bar{T}$, taking into account all three possible decay modes into third-generation SM quarks [18–23]. Considering the most restrictive limits set by any of the Run 1 ATLAS searches, the resulting observed (expected) lower limits on the T quark mass vary between 730 GeV and 950 GeV (715 GeV and 885 GeV), depending on the values of the branching ratios into the three decay modes assumed. The corresponding observed (expected) lower limits from the combination of the Run 1 CMS searches range between 720 GeV and 920 GeV (740 GeV and 900 GeV). The increased centre-of-mass energy of $\sqrt{s} = 13$ TeV in Run 2 results in a significantly larger pair-production cross section compared to Run 1, particularly at high values of the vector-like T-quark mass, enhancing the discovery potential. Early Run 2 searches for $T\bar{T}$ production have been performed by the ATLAS [24–26] and CMS [27] collaborations, respectively using 3.2 fb^{-1} and 2.3 fb^{-1} of pp collisions at $\sqrt{s} = 13$ TeV recorded in 2015. Among them, the ATLAS search for $T\bar{T} \to Ht$+X in the single-lepton channel [24] has obtained observed (expected) 95% CL limits of $m_T > 800\,(900)$ GeV and $m_T > 750\,(780)$ GeV for a weak-isospin doublet and singlet, respectively. The searches presented in this note represent a significant extension, both in integrated luminosity and scope, over that search.

The top quark plays a prominent role in many BSM scenarios, often participating in new interactions related to electroweak symmetry breaking, or preferentially coupling to new degrees of freedom. Such BSM scenarios often predict an enhanced rate of events containing four top quarks ($t\bar{t}t\bar{t}$) in the final state, compared to the SM production via the strong interaction. Examples include top quark compositeness [28–30] or universal extra dimensions [31–33]. Using the full Run 1 dataset, the CMS Collaboration has

performed a search for SM $t\bar{t}t\bar{t}$ production [34], while the ATLAS Collaborations has performed searches for $t\bar{t}t\bar{t}$ production within the SM as well as in several BSM scenarios [18, 20]. Early Run 2 searches [24, 25, 35, 36] have already achieved more restrictive bounds than those obtained in Run 1.

The addition of another SU(2) doublet of fields to the Higgs sector is one of the simplest extensions of the SM and defines a large class of models, which are collectively referred to as two-Higgs-doublet models (2HDMs) (see e.g. Ref. [37] for a review). In the case where the Higgs potential of the 2HDM is CP conserving, the Higgs bosons after electroweak symmetry breaking are two CP-even (h and H), one CP-odd (A) and two charged ($H^{\pm}$) Higgs bosons. In general, the model allows to have the lightest CP-even Higgs boson (h) correspond to the one discovered at the LHC, i.e. it has a mass of 125 GeV. Existing constraints from direct searches for heavy neutral and charged Higgs bosons by the ATLAS and CMS collaborations (for recent results at $\sqrt{s} = 13$ TeV see Refs. [38–44] and [45–49] respectively), as well as those resulting from the measurements of SM Higgs-boson couplings [50–52], restrict the available parameter-space to the so-called "alignment limit". In this limit the couplings of h are the same as for the SM Higgs boson. For masses of the heavy neutral Higgs bosons above twice the top quark mass, the dominant decay mode is $H/A \to t\bar{t}$. Inclusive searches for $H/A \to t\bar{t}$ are challenging because of negative interference effects with the SM background that largely dilute a resonant peak in the $t\bar{t}$ invariant mass spectrum [53], although first results have been obtained by the ATLAS Collaboration [54]. Another possibility is to search for associated production with third generation quarks, $b\bar{b}H/A(\to t\bar{t})$ and $t\bar{t}H/A(\to t\bar{t})$. Charged Higgs bosons are mainly produced via associated production with third-generation quarks, and they decay dominantly into a top quark and a bottom quark as soon as kinematically allowed, $tbH^{\pm}(\to tb)$.[1] Direct searches for $tbH^{\pm}(\to tb)$ have been performed by the ATLAS [44, 55] and CMS [56] collaborations. The importance of these search modes and their complementarity to probe an extended Higgs sector has recently been highlighted in a number of phenomenological studies [57–60].

This note presents a broad search for new phenomena in $t\bar{t}$ final states with additional heavy-flavour jets, resulting from either $T\bar{T}$ production, $t\bar{t}t\bar{t}$ production (both within the SM and in several BSM scenarios), as well as $t\bar{t}H/A \to t\bar{t}t\bar{t}$, $b\bar{b}H/A \to b\bar{b}t\bar{t}$ and $tbH^{\pm} \to tbtb$ production. This search uses 13.2 fb^{-1} of data at $\sqrt{s} = 13$ TeV recorded in 2015 and 2016 by the ATLAS Collaboration, and it follows closely the analysis strategy developed in Ref. [24] for the single-lepton channel (referred to as "1-lepton" in the following). In addition, it includes a new search channel with no leptons and large missing transverse momentum (referred to as "0-lepton" in the following). The two channels are combined, yielding significant improvements in sensitivity to $T\bar{T}$ production compared to the individual searches.

This note is organised as follows. After a brief overview of the ATLAS detector in Section 2, the main reconstructed physics objects used in this search are summarised in Section 3. Section 4 is devoted to a discussion of the dataset and event preselection requirements. Sections 5 and 6 summarise the simulated samples used for signal and background modelling, respectively. A discussion of the analysis strategy, including the final event selection requirements, the event categorisation and final discriminating variable used, is presented in Section 7. A detailed discussion of the systematic uncertainties considered in this search is given in Section 8. The statistical analysis and results obtained are presented in Sections 9 and 10, respectively. Finally, the summary and conclusions are given in Section 11.

[1] In the following, $tbH^{\pm}(\to tb)$ is used to denote $\bar{t}bH^{+}(\to t\bar{b})$ and its charge conjugate, $t\bar{b}H^{-}(\to \bar{t}b)$.

2. ATLAS detector

The ATLAS detector [61] at the LHC covers almost the entire solid angle around the collision point, and consists of an inner tracking detector surrounded by a thin superconducting solenoid magnet producing a 2 T axial magnetic field, electromagnetic and hadronic calorimeters, and a muon spectrometer incorporating three large toroid magnet assemblies. The inner detector consists of a high-granularity silicon pixel detector, including the newly-installed insertable B-layer [62], and a silicon microstrip tracker, together providing a precise reconstruction of tracks of charged particles in the pseudorapidity[2] range $|\eta| < 2.5$, complemented by a transition radiation tracker providing tracking and electron identification information for $|\eta| < 2.0$. The electromagnetic (EM) sampling calorimeter uses lead as the absorber material and liquid-argon (LAr) as the active medium, and is divided into barrel ($|\eta| < 1.475$) and end-cap ($1.375 < |\eta| < 3.2$) regions. Hadron calorimetry is also based on the sampling technique, with either scintillator tiles or LAr as the active medium, and with steel, copper, or tungsten as the absorber material. The calorimeters cover $|\eta| < 4.9$. The muon spectrometer measures the deflection of muons with $|\eta| < 2.7$ using multiple layers of high-precision tracking chambers located in a toroidal field of approximately 0.5 T and 1 T in the central and end-cap regions of ATLAS, respectively. The muon spectrometer is also instrumented with separate trigger chambers covering $|\eta| < 2.4$. A two-level trigger system [63], consisting of a hardware-based Level-1 trigger followed by a software-based High Level Trigger (HLT), is used to reduce the event rate to a maximum of around 1 kHz for offline storage.

3. Object reconstruction

Interaction vertices from the proton-proton collisions are reconstructed from at least two tracks with transverse momentum (p_{T}) larger than 400 MeV that are consistent with originating from the beam collision region in the x–y plane. If more than one primary vertex candidate is found, the one that has the largest sum of the squared p_{T} of its associated tracks [64] is selected as the hard-scatter primary vertex.

Basic selections are applied to define candidates for electrons, muons and jets in the event. An overlap removal procedure is applied to these candidates to prevent double-counting of the objects. Further requirements are then made to select the final leptons and jets from the remaining objects. The details of the object selections and of the overlap removal procedure are given below.

Electron candidates [65–67] are reconstructed from energy clusters in the EM calorimeter that are matched to reconstructed tracks in the inner detector and have $|\eta_{\mathrm{cluster}}| < 2.47$, excluding the transition region $1.37 < |\eta_{\mathrm{cluster}}| < 1.52$ between sections of the EM calorimeter. They are also required to satisfy "medium" quality requirements [65] based on calorimeter, tracking and combined variables that provide good separation between electrons and jets. Muon candidates [68] are reconstructed from track segments in the various layers of the muon spectrometer that are matched with tracks found in the inner detector. The resulting muon candidates are refitted using the complete track information from both detector systems and are required to have $|\eta| < 2.5$. Electron (muon) candidates are matched to the primary vertex by requiring that the significance of their transverse impact parameter, d_0, satisfies $|d_0/\sigma(d_0)| < 5(3)$,

[2] ATLAS uses a right-handed coordinate system with its origin at the nominal interaction point (IP) in the centre of the detector and the z-axis coinciding with the axis of the beam pipe. The x-axis points from the IP to the centre of the LHC ring, and the y-axis points upward. Cylindrical coordinates (r,ϕ) are used in the transverse plane, ϕ being the azimuthal angle around the beam pipe. The pseudorapidity is defined in terms of the polar angle θ as $\eta = -\ln\tan(\theta/2)$. Angular distance is measured in units of $\Delta R \equiv \sqrt{(\Delta\eta)^2 + (\Delta\phi)^2}$.

where $\sigma(d_0)$ is the measured uncertainty on d_0, and their longitudinal impact parameter, z_0, satisfies $|z_0 \sin\theta| < 0.5$ mm. Furthermore, they are required to have $p_{\mathrm{T}} > 10$ GeV and to survive the overlap removal procedure discussed below.

Candidate jets are reconstructed with the anti-k_t algorithm [69–71] with a radius parameter $R = 0.4$ (referred to as "small-R jets"), using topological clusters[3] [72, 73] built from energy deposits in the calorimeters calibrated to the electromagnetic scale. The reconstructed jets are then calibrated to the particle level by the application of a jet energy scale derived from simulation and *in situ* corrections based on $\sqrt{s} = 13$ TeV data [74, 75]. Quality criteria are imposed to reject events that contain any jets arising from non-collision sources or detector noise [76]. To reduce the contamination due to jets originating from pile-up interactions, an additional requirement on the Jet Vertex Tagger (JVT) [77] output to be less than 0.59 is made for jets with $p_{\mathrm{T}} < 60$ GeV and $|\eta| < 2.4$. Candidate jets with $p_{\mathrm{T}} > 25$ GeV and $|\eta| < 2.5$ are used in the overlap removal procedure discussed below.

Jets containing b-hadrons are identified (b-tagged) via an algorithm [78, 79] that uses multivariate techniques to combine information from the impact parameters of displaced tracks as well as topological properties of secondary and tertiary decay vertices reconstructed within the jet. For each jet, a value for the multivariate b-tagging discriminant is calculated. The jet is considered b-tagged if this value is above a given threshold. The threshold used in this search corresponds to an average 77% efficiency to tag a b-quark jet, with a light-jet[4] rejection factor of ∼126 and a charm-jet rejection factor of ∼4.5, as determined for jets with $p_{\mathrm{T}} > 20$ GeV and $|\eta| < 2.5$ in simulated $t\bar{t}$ events.

Overlaps between candidate objects are removed sequentially. Firstly, electron candidates that lie within $\Delta R = 0.01$ of a muon candidate are removed to suppress contributions from muon bremsstrahlung. Overlaps between electron and jet candidates are resolved next, and finally, overlaps between remaining jet candidates and muon candidates are removed. Clusters from identified electrons are not excluded during jet reconstruction. In order to avoid double-counting of electrons as jets, the closest jet whose axis is within $\Delta R < 0.2$ of an electron is discarded. If the electron is within $\Delta R < 0.4$ of the axis of any jet after this initial removal, the jet is retained and the electron is removed. The overlap removal procedure between the remaining jet candidates and muon candidates is designed to remove those muons that are likely to have arisen in the decay chain of hadrons and to retain the overlapping jet instead. Jets and muons may also appear in close proximity when the jet results from high-p_{T} muon bremsstrahlung, and in such cases the jet should be removed and the muon retained. Such jets are characterised by having very few matching inner detector tracks. Therefore, if a muon lies within $\Delta R = 0.4$ of the axis of a jet, the jet is removed if either it has fewer than three matching tracks or it has a p_{T} less than 50% of the p_{T} of the muon. If any of these conditions on the jet are not fulfilled, then the muon is removed and the jet is kept.

The candidate small-R jets surviving the overlap procedure discussed above are used as inputs for further jet re-clustering [80] using the anti-k_t algorithm with a radius parameter $R = 1.0$. In order to suppress contributions from pile-up and soft radiation, the re-clustered large-R jets are trimmed [81] by removing all small-R (sub-)jets within a re-clustered jet that have p_{T} below 5% of the p_{T} of the re-clustered jet (i.e. $f_{\mathrm{cut}} = 0.05$). Due to the pileup suppression and $p_{\mathrm{T}} > 25$ GeV requirements made on the small-R jets, the average fraction of small-R jets removed by the trimming requirement is less than 1%. The resulting large-R jets are used to identify high-p_{T} hadronically-decaying top quark and Higgs boson candidates by requiring them to have $p_{\mathrm{T}} > 300$ GeV, $|\eta| < 2.0$ and mass[5] above 100 GeV. In order to ensure that

[3] Each cluster in the calorimeter is considered a massless object.
[4] Light-jet denotes a jet originating from the hadronisation of a light quark (u, d, s) or a gluon.
[5] The re-clustered jet mass is computed from the sum of the four-momenta of the associated small-R (sub-)jets.

the mass of the large-R jet originates from the p_{T} and angular separation of the sub-jets, instead of from the un-calibrated small-R jet mass, a requirement of $\geq$2 sub-jets is made. In this way it is possible to evaluate the uncertainty on the mass of the large-R jets coming from the calibration of its constituents by varying the energy scale and resolution of small-R jets. The fraction of re-clustered jets rejected by this requirement is about 1% in $t\bar{t}$ simulated events and up to about 10% for the highest-mass simulated signals considered in this search. The resulting large-R jets will be referred to as "mass-tagged" jets.

After resolving the overlaps, the final lepton candidates used in the analysis must have $p_{\mathrm{T}} > 25$ GeV. The resulting electron candidates must also satisfy "tight" quality requirements [65]. Finally, to reduce the background from non-prompt electrons or muons resulting from semileptonic decays of b- or c-hadrons, and from jets with a high fraction of their energy deposited in the EM calorimeter, lepton (electron or muon) candidates are required to be isolated. These criteria include both track and calorimeter information and are designed to give an average efficiency of ≈90% for leptons from Z boson decays with p_{T} of 25 GeV, rising to ≈99% for p_{T} of 60 GeV.

The missing transverse momentum $\vec{p}_{\mathrm{T}}^{\,\mathrm{miss}}$ (with magnitude $E_{\mathrm{T}}^{\mathrm{miss}}$) is defined as the magnitude of the negative vector sum of the p_{T} of all selected and calibrated objects in the event, including a term to account for energy from soft particles in the event that is not associated to any of the selected objects. This soft term is calculated from inner detector tracks matched to the selected primary vertex to make it more resilient to contamination from pileup interactions [82, 83].

Simulated signal and background events are processed through the same reconstruction software as the data. They are corrected so that the object identification efficiencies, energy scales and energy resolutions match those determined from data control samples. Details on signal and background modelling are provided in Sections 5 and 6.

4. Data sample and event preselection

This search is based on pp collision data at $\sqrt{s} = 13$ TeV and with 25 ns bunch spacing collected by the ATLAS experiment between August and November 2015 and between April and July 2016. Only events recorded with a single-electron trigger, a single-muon trigger, or a $E_{\mathrm{T}}^{\mathrm{miss}}$ trigger under stable beam conditions and for which all detector subsystems were operational are considered, corresponding to an integrated luminosity of 13.2 fb^{-1}.

Single-lepton triggers with low p_{T} threshold and lepton isolation requirements are combined in a logical OR with higher-threshold triggers without isolation requirements to give maximum efficiency. For muon triggers, the lowest p_{T} threshold is 20 (24) GeV in 2015 (2016), while the higher p_{T} threshold is 40 (50) GeV. For electrons, isolated triggers with a p_{T} threshold of 24 GeV are used with non-isolated triggers at 60 GeV in both years, along with a 120 (140) GeV trigger which also uses looser identification criteria. The $E_{\mathrm{T}}^{\mathrm{miss}}$ trigger [63] considered uses an $E_{\mathrm{T}}^{\mathrm{miss}}$ threshold at the HLT level of 70 (100) GeV in 2015 (2016).

Events satisfying the trigger selection are required to have at least one primary vertex candidate. They are then classified into the "1-lepton" or "0-lepton" channels depending on the multiplicity of selected leptons. Events in the 1-lepton channel are required to satisfy a single lepton trigger and to have exactly one selected electron or muon that matches, with $\Delta R < 0.15$, the lepton reconstructed by the trigger. In the following, 1-lepton events satisfying either the electron or muon selections are combined and treated as a single analysis channel. Events in the 0-lepton channel are required to satisfy the $E_{\mathrm{T}}^{\mathrm{miss}}$ trigger and

Preselection requirements		
Requirement	1-lepton channel	0-lepton channel
Trigger	Single-lepton trigger	$E_{\mathrm{T}}^{\mathrm{miss}}$ trigger
Leptons	=1 isolated e or μ	=0 isolated e or μ
Jets	≥5 jets	≥6 jets
b-tagging	≥2 b-tagged jets	≥2 b-tagged jets
$E_{\mathrm{T}}^{\mathrm{miss}}$	$E_{\mathrm{T}}^{\mathrm{miss}} > 20$ GeV	$E_{\mathrm{T}}^{\mathrm{miss}} > 200$ GeV
Other $E_{\mathrm{T}}^{\mathrm{miss}}$-related	$E_{\mathrm{T}}^{\mathrm{miss}} + m_{\mathrm{T}}^{W} > 60$ GeV	$\Delta\phi_{\mathrm{min}}^{4j} > 0.4$

Table 1: Summary of preselection requirements for the 1-lepton and 0-lepton channels. Here m_{T}^{W} is the transverse mass of the lepton and the $E_{\mathrm{T}}^{\mathrm{miss}}$ vector, and $\Delta\phi_{\mathrm{min}}^{4j}$ is the minimum azimuthal separation between the $E_{\mathrm{T}}^{\mathrm{miss}}$ vector and the four highest-p_{T} jets.

to have no selected leptons. In addition, events in the 1-lepton (0-lepton) channel are required to have ≥5 (≥6) small-R jets. In the following, all selected small-R jets are considered, including those used to build large-R jets. For both channels, backgrounds not including b-quark jets are suppressed by requiring at least two b-tagged jets.

Additional requirements are made to suppress the background from multijet production. In the case of the 1-lepton channel, requirements are made on $E_{\mathrm{T}}^{\mathrm{miss}}$ as well as on the transverse mass of the lepton and $E_{\mathrm{T}}^{\mathrm{miss}}$ system (m_{T}^{W}):[6] $E_{\mathrm{T}}^{\mathrm{miss}} > 20$ GeV and $E_{\mathrm{T}}^{\mathrm{miss}} + m_{\mathrm{T}}^{W} > 60$ GeV. In the case of the 0-lepton channel, the requirements are $E_{\mathrm{T}}^{\mathrm{miss}} > 200$ GeV (for which the $E_{\mathrm{T}}^{\mathrm{miss}}$ trigger is fully efficient) and $\Delta\phi_{\mathrm{min}}^{4j} > 0.4$, where $\Delta\phi_{\mathrm{min}}^{4j}$ is the minimum azimuthal separation between $\vec{p}_{\mathrm{T}}^{\,\mathrm{miss}}$ and the four highest-p_{T} jets. The later requirement is very effective in the 0-lepton channel to suppress multijet events, where the large $E_{\mathrm{T}}^{\mathrm{miss}}$ results from the mismeasurement of a high-p_{T} jet or the presence of neutrinos emitted close to a jet axis.

The above requirements are referred to as the “preselection" and are summarised in Table 1.

5. Signal modelling

This section describes the different signal scenarios considered in the interpretation of the results, together with details of how they are modelled.

5.1. Vector-like quark pair production

Figure 1 depicts a representative Feynman diagram for the signals probed by the search discussed in this note. More details on the phenomenology of $T\bar{T}$ production and decay can be found in Ref. [24]. Samples of simulated $T\bar{T}$ events are generated with the leading-order (LO) generator Protos 2.2 [13, 84] using the NNPDF2.3 LO [85] PDF set and passed to Pythia 8.186 [86] for parton showering and fragmentation. The A14 [87] set of optimised parameters for the underlying event (UE) description

[6] $m_{\mathrm{T}}^{W} = \sqrt{2p_{\mathrm{T}}^{\ell}E_{\mathrm{T}}^{\mathrm{miss}}(1-\cos\Delta\phi)}$, where p_{T}^{ℓ} is the transverse momentum (energy) of the muon (electron) and $\Delta\phi$ is the azimuthal angle separation between the lepton and the direction of the missing transverse momentum.

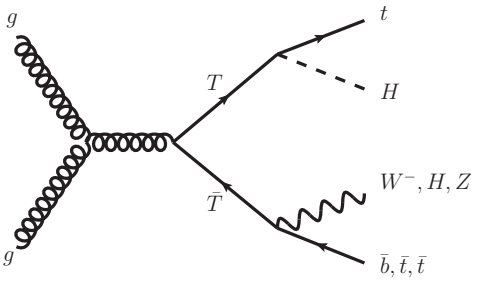

Figure 1: Representative leading-order Feynman diagram for the main $T\bar{T}$ production process probed by this search.

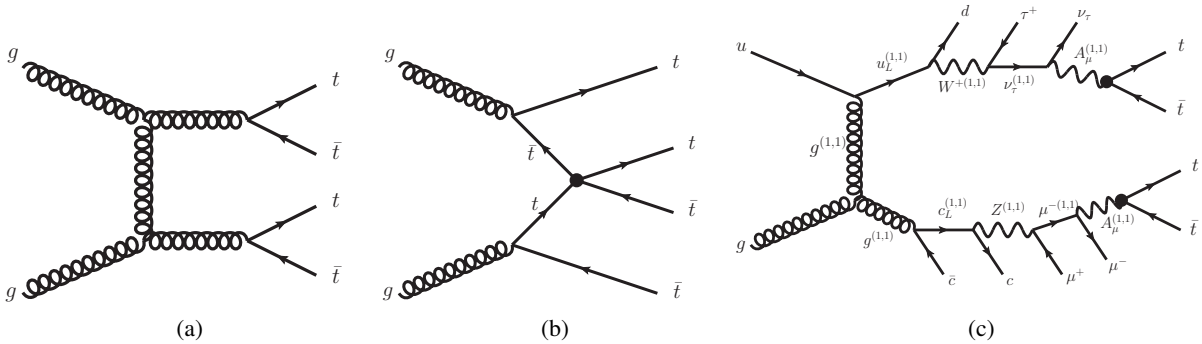

Figure 2: Representative leading-order Feynman diagrams for four-top-quark production (a) within the SM, (b) via an effective four-top-quark interaction in an effective field theory model, and (c) via cascade decays from Kaluza–Klein excitations in a universal extra dimensions model with two extra dimensions compactified using the geometry of the real projective plane.

using the NNPDF2.3 LO PDF set, referred to as the "UE tune", is used. The vector-like quarks are forced to decay with a branching ratio of 1/3 to each of the three modes (W, Z, H). Arbitrary sets of branching ratios consistent with the three decay modes summing to unity are obtained by reweighting the samples using generator-level information. Samples are generated assuming singlet couplings and for heavy-quark masses between 350 GeV and 1500 GeV in steps of 50 GeV. Additional samples are produced at three mass points (700 GeV, 950 GeV and 1200 GeV) assuming doublet couplings, in order to confirm that kinematic differences arising from the different chirality of singlet and doublet couplings, after reweighting the singlet and doublet samples to the same branching ratios, have negligible impact on this analysis. In all samples (both signal and background) used in this search, the top quark and SM Higgs boson masses are set to 172.5 GeV and 125 GeV respectively. The $T\bar{T}$ samples are normalised using the theoretical cross section computed using Top++ v2.0 [88] at next-to-next-to-leading order (NNLO) in QCD, including resummation of next-to-next-to-leading logarithmic (NNLL) soft gluon terms [89–93], and using the MSTW 2008 NNLO [94, 95] set of parton distribution functions (PDF).

5.2. Four-top-quark production

Figure 2 depicts representative LO Feynman diagrams for four-top-quark production within the SM and two different BSM scenarios considered in this analysis: via an effective field theory (EFT) involving

a four-fermion contact interaction among right-handed top quarks [96], and within a Universal Extra Dimensions (UED) model with two extra dimensions that are compactified using the geometry of the real projective plane (2UED/RPP) [31]. More details on these BSM scenarios can be found in Ref. [24].

Samples of simulated four-top-quark events for the three production mechanisms discussed above are generated at LO with the MADGRAPH5_aMC@NLO [97] generator (referred to in the following as MG5_aMC; the versions used are 2.2.2, 2.2.3 and 1.5.14 for SM, EFT and 2UED/RPP, respectively) and the NNPDF2.3 LO PDF set, interfaced to PYTHIA 8 (the versions used are 8.186, 8.205 and 8.186 for SM, EFT and 2UED/RPP, respectively) and the A14 tune [87]. The SM $t\bar{t}t\bar{t}$ sample is normalised to a cross section of 9.2 fb (computed at NLO with MG5_aMC), while the EFT $t\bar{t}t\bar{t}$ sample is normalised assuming $|C_{4t}|/\Lambda^2 = 4\pi$ TeV^{-2}, which yields a cross section of 928 fb. In the case of the 2UED/RPP model, samples are generated for four different values of m_{KK} (1000 to 1800 GeV in steps of 200 GeV) and the BRIDGE [98] generator is used to decay the pair-produced excitations from tier (1,1) generated by MADGRAPH5.

5.3. Associated heavy Higgs boson production

A 2HDM has a very rich phenomenology, depending on the vacuum expectation values of the Higgs doublets (parameterised by $\tan\beta$), the CP properties of the Higgs potential and the values of its parameters, and the Yukawa couplings of the Higgs doublets with the fermions. A CP-conserving 2HDM of either Type-I or Type-II is used as a benchmark scenario in this analysis. Denoting the two Higgs doublet fields in this model as Φ_1 and Φ_2, in a Type-I 2HDM all fermions couple only to Φ_1, whereas in a Type-II 2HDM up-type right-handed fermions couple to Φ_2 and down-type right-handed fermions to Φ_1. For instance, the Higgs sector of the minimal supersymmetric SM (MSSM) [4–6, 99–101] is an example of a Type-II 2HDM. In both 2HDM types the couplings of the h and H Higgs bosons to the vector bosons are the same as the couplings of the SM Higgs boson times $\sin(\beta-\alpha)$ and $\cos(\beta-\alpha)$ respectively, where α is the mixing angle between the two CP-even bosons, whereas for the A Higgs boson these couplings vanish. The alignment limit of the 2HDM is defined as the regime in which $\cos(\beta-\alpha) \to 0$. In this limit, the couplings of the neutral heavy Higgs bosons, H and A, to fermions are proportional to the couplings of the SM Higgs boson times $\cot\beta$, in the case of a Type-I 2HDM, or $\cot\beta$ for up-type fermions and $\tan\beta$ for down-type fermions, in the case of a Type-II 2HDM. In the case of the $H^\pm$ bosons, the couplings to fermions not only depend on their masses and $\tan\beta$, but also on their chirality. For instance, in a Type-I (Type-II) 2HDM the coupling strengths for the $\bar{f}'_R f_L H^+$ and $\bar{f}'_L f_R H^+$ interactions are proportional to $m_{f'}\cot\beta$ and $m_f\cot\beta$ ($m_f\tan\beta$) respectively. See Ref. [37] for the general expressions of these couplings without the restriction of $\cos(\beta-\alpha)=0$.

The above couplings drive the phenomenology of an extended Higgs sector. In the alignment limit, the $H/A \to t\bar{t}$ decay mode is dominant for $m_{H/A} > 2m_t$ at low $\tan\beta$, whereas the $H^+ \to t\bar{b}$ decay mode is dominant for $m_{H^+} > m_t + m_b$ for any value of $\tan\beta$. The cross sections for associated production of heavy Higgs bosons and third generation quarks depend strongly on the coupling strengths. Taking into account the product of cross section times branching ratio, the most promising search modes are $b\bar{b}H/A(\to t\bar{t})$ production (for $\tan\beta \sim 5$ in a Type-II 2HDM), $t\bar{t}H/A(\to t\bar{t})$ production (for $\tan\beta \leq 1$ in both Type-I and Type-II 2HDMs), and $tbH^\pm(\to tb)$ production (for $\tan\beta \leq 1$ in both Type-I and Type-II 2HDMs, and also for high $\tan\beta$ in a Type-II 2HDM). Figure 3 depicts representative LO Feynman diagrams for each of these associated production modes.

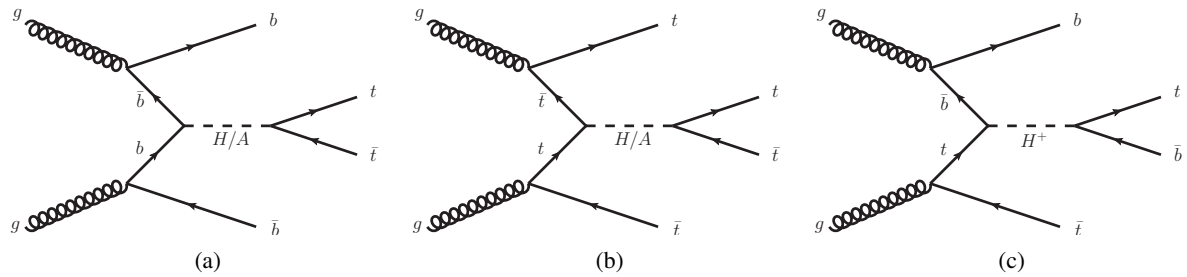

Figure 3: Representative leading-order Feynman diagrams for (a) $b\bar{b}H/A(\rightarrow t\bar{t})$ production, (b) $t\bar{t}H/A(\rightarrow t\bar{t})$ production, and (c) $tbH^{\pm}(\rightarrow tb)$ production, where $H(A)$ and $H^{\pm}$ denote the heavy Higgs bosons appearing in a 2HDM. All diagrams are in the four-flavour number scheme.

Samples of simulated $b\bar{b}H(\rightarrow t\bar{t})$ and $t\bar{t}H(\rightarrow t\bar{t})$ events are generated assuming a Type-II 2HDM model using the MG5_aMC 2.3.3 generator, interfaced to Pythia 8.210 [102] and the A14 tune. The matrix element calculation is performed at LO in QCD in four-flavour-number scheme (4FNS) and the corresponding 4FNS CTEQ6L1 PDF set [103] is used. Spin correlations are taken into account in the decays of top quarks and W bosons. Samples are generated for heavy Higgs boson masses between 400 GeV and 1000 GeV in steps of 100 GeV. These samples can also be used to model $b\bar{b}A(\rightarrow t\bar{t})$ and $t\bar{t}A(\rightarrow t\bar{t})$ production, as generator level studies showed no significant differences in the kinematics of the decay products for processes involving the production of a CP-even or CP-odd Higgs boson of the same mass.

The $tbH^{\pm}(\rightarrow tb)$ samples are generated at next-to-leading-order (NLO) in QCD using MG5_aMC 2.2.2 with the NNPDF2.3 PDF set, interfaced to Pythia 8.212 with the A14 tune. A Type-II 2HDM model is assumed. The width of the charged Higgs boson has been set to zero. Samples are generated for charged Higgs boson masses between 200 GeV and 2000 GeV.

All $b\bar{b}H(\rightarrow t\bar{t})$, $t\bar{t}H(\rightarrow t\bar{t})$, and $tbH^{\pm}(\rightarrow tb)$ samples are normalised to a reference cross section times branching ratio of 1 pb. For the interpretation of results, cross sections and branching ratios are computed separately for Type-I and Type-II 2HDMs, as a function of heavy Higgs boson mass, $\tan\beta$ and $\cos(\beta-\alpha)$. In the case of $b\bar{b}H(\rightarrow t\bar{t})$ and $t\bar{t}H(\rightarrow t\bar{t})$ production, the predictions are obtained using the codes SusHi 1.5.0 [104], which implements calculations from Refs. [105–109], and 2HDMC 1.7.0 [110]. The $t\bar{t}H(\rightarrow t\bar{t})$ cross sections are computed at NLO in QCD, whereas the $b\bar{b}H(\rightarrow t\bar{t})$ cross sections are obtained from the so-called "Santander matching" of NLO cross sections in 4FNS and NNLO cross sections in 5FNS [111]. Similarly, the $tbH^{\pm}(\rightarrow tb)$ cross sections are obtained using the "Santander matching" of 4FNS NLO and 5FNS NNLO cross sections [112–115]. The charged Higgs boson branching ratios are also obtained using 2HDMC.

All simulated signal samples utilise EvtGen [116] to model the decays of heavy flavour hadrons. Events from minimum-bias interactions are simulated with the Pythia 8.186 generator with the MSTW 2008 LO [117] PDF set and the A2 tune [118]. They are overlaid on the simulated signal events according to the luminosity profile of the recorded data. The contributions from these pile-up interactions are modelled both within the same bunch crossing as the hard-scattering process and in neighbouring bunch crossings. Finally, the generated samples are processed through a simulation [119] of the detector geometry and response using Geant4 [120]. In the case of the $b\bar{b}H(\rightarrow t\bar{t})$, $t\bar{t}H(\rightarrow t\bar{t})$ and $tbH^{\pm}(\rightarrow tb)$ samples a fast simulation of the calorimeter response [119] is used.

6. Background modelling

After the event preselection, the main background is $t\bar{t}$ production, often in association with jets, denoted by $t\bar{t}$+jets in the following. Small contributions arise from single-top-quark, W/Z+jets, multijet and diboson (WW, WZ, ZZ) production, as well as from the associated production of a vector boson V ($V = W, Z$) or a Higgs boson and a $t\bar{t}$ pair ($t\bar{t}V$ and $t\bar{t}H$). All backgrounds are estimated using samples of simulated events and initially normalised to their theoretical cross sections, with the exception of the multijet background, which is estimated using data-driven methods. Similarly to the signal samples, the simulated background samples use EvtGen, include the contribution from pile-up interactions, and are processed through a full Geant4 detector simulation. Further details about the modelling of each of the backgrounds are provided below. The background prediction is further improved during the statistical analysis by performing a likelihood fit to data using multiple signal-depleted control regions, as discussed in Section 7.

Samples of $t\bar{t}$+jets events are generated with the next-to-leading-order (NLO) generator[7] Powheg-Box 2.0 [121–124] using the CT10 PDF set [125]. All samples are generated assuming a top quark mass (m_t) of 172.5 GeV and top quarks decaying exclusively through $t \to Wb$. The Powheg-Box model parameter h_{damp}, which controls matrix element to parton shower matching and effectively regulates the high-p_{T} radiation, is set to m_t, a setting which was found to describe the $t\bar{t}$ system p_{T} at $\sqrt{s} = 7$ TeV [126]. The nominal sample is interfaced to Pythia 6.428 [102] with the CTEQ6L PDF set and the Perugia 2012 (P2012) UE tune [127]. Alternative $t\bar{t}$ simulation samples are generated using Powheg-Box interfaced to Herwig++ 2.7.1 [128] and MG5_aMC 2.2.1 [97] interfaced to Herwig++ 2.7.1. The effects of initial- and final-state radiation (ISR/FSR) are explored using two alternative Powheg-Box+Pythia samples, one with h_{damp} set to $2m_t$, the renormalisation and factorisation scales set to half the nominal value and using the P2012 radHi UE tune, giving more radiation (referred to as "radHi"), and one with the P2012 radLo UE tune, $h_{\text{damp}} = m_t$ and the renormalisation and factorisation scales set to twice the nominal value, giving less radiation (referred to as "radLow") [129]. All $t\bar{t}$+jets samples are normalised to the theoretical cross section of 832^{+46}_{-51} pb, obtained using Top++ at NNLO in QCD and including resummation of NNLL soft gluon terms.

The $t\bar{t}$ samples are generated inclusively, but events are categorised depending on the flavour content of additional particle jets not originating from the decay of the $t\bar{t}$ system (see Ref. [24] for details). Events labelled as either $t\bar{t}$+$\geq 1b$ or $t\bar{t}$+$\geq 1c$ are generically referred to below as $t\bar{t}$+HF events, where HF stands for "heavy flavour". A finer categorisation of $t\bar{t}$+HF events is considered for the purpose of applying further corrections and assigning systematic uncertainties associated with the modelling of heavy-flavour production in different topologies (see Refs. [130, 131] for details). The remaining events are labelled as $t\bar{t}$+light-jet events, including those with no additional jets. Small improvements to the modelling are made by reweighting all $t\bar{t}$ samples to match their top quark p_{T} distribution to that predicted at NNLO accuracy in QCD [132, 133]. In previous analyses improved agreement between data and prediction has been observed, particularly for the top quark p_{T} distribution, when comparing to NNLO calculations [134]. This correction is not applied to $t\bar{t}$+$\geq 1b$ events, which instead is reweighted to an NLO prediction in 4FNS of $t\bar{t}$+$\geq 1b$ including parton showering [135], based on Sherpa+OpenLoops [136, 137] (referred to as SherpaOL in the following) using the CT10 PDF set. This reweighting is performed separately for each of the above $t\bar{t}$+$\geq 1b$ topologies in such a way that their inter-normalisation and the shape of the relevant kinematic distributions are at NLO accuracy, while preserving the nominal $t\bar{t}$+$\geq 1b$ cross section in Powheg-Box+Pythia. More details on the modelling of the $t\bar{t}$+jets background can be found in Ref. [131].

[7] In the following, NLO generator should be understood as referring to QCD.

Samples of single-top-quark background corresponding to the t-channel production mechanism are generated using the Powheg-Box 2.0 [138] generator that uses the 4FNS for the NLO matrix element calculations and the fixed four-flavour CT10f4 [125] PDF set. Samples corresponding to the Wt and s-channel production mechanisms are generated with Powheg-Box 2.0 using the CT10 PDF set. Overlaps between the $t\bar{t}$ and Wt final states are avoided using the "diagram removal" scheme [139]. The parton shower, hadronisation and the underlying event are modelled using Pythia 6.425 with the CTEQ6L1 PDF set in combination with the P2012 UE tune. The single-top-quark samples are normalised to the approximate NNLO theoretical cross sections [140–142].

Samples of W/Z+jets events are generated with the Sherpa 2.2 [136] generator. The matrix-element calculation is performed using up to two partons at NLO and up to four partons at LO using Comix [143] and OpenLoops [137]. The matrix element calculation is merged with the Sherpa parton shower [144] using the ME+PS@NLO prescription [145]. The PDF set used for the matrix-element calculation is CT10 with a dedicated parton shower tuning developed for Sherpa. Separate samples are generated for different W/Z+jets categories using filters for a b-jet (W/Z+$\geq$1b+jets), a c-jet and no b-jet (W/Z+$\geq$1c+jets), and with a veto on b and c-jets (W/Z+light-jets), which are combined into the inclusive W/Z+jets samples. Both the W+jets and Z+jets samples are normalised to their respective inclusive NNLO theoretical cross sections in QCD calculated with FEWZ [146].

Samples of $WW/WZ/ZZ$+jets events are generated with Sherpa 2.1.1 using the CT10 PDF set and include processes containing up to four electroweak vertices. The matrix-element includes zero additional partons at NLO and up to three partons at LO using the same procedure as for the W/Z+jets samples. The final states simulated require one of the bosons to decay leptonically and the other hadronically. All diboson samples are normalised to their NLO theoretical cross sections provided by Sherpa.

Samples of $t\bar{t}V$ and $t\bar{t}H$ events are generated with MG5_aMC 2.3.2, using NLO matrix elements and the NNPDF3.0NLO [147] PDF set. Showering is performed using Pythia 8.210 and the A14 UE tune. The $t\bar{t}V$ samples are normalised to the NLO cross section computed with MG5_aMC. The $t\bar{t}H$ sample is normalised using the NLO cross section [148–152] and the Higgs boson decay branching ratios calculated using Hdecay [153].

The background from multijet production ("multijet background" in the following) in the 1-lepton channel contributes to the selected data sample via several production and misreconstruction mechanisms. In the electron channel, it consists of non-prompt electrons (from semileptonic b- or c-hadron decays) as well as misidentified photons (e.g. from a conversion of a photon into an e^+e^- pair) or jets with a high fraction of their energy deposited in the EM calorimeter. In the muon channel, the multijet background is predominantly from non-prompt muons. The multijet background normalisation and shape are estimated directly from data by using the "matrix method" technique [154], which exploits differences in lepton identification and isolation properties between prompt leptons and leptons that are either non-prompt or result from the misidentification of photons or jets. Further details can be found in Ref. [18]. In the case of the 0-lepton channel, the preselection requirements discussed in Section 4 render the multijet background negligible, which is hence not considered in the following.

7. Analysis strategy

The searches discussed in this note are optimised for discovery of $T\bar{T}$ production where at least one of the T quarks decays into a Higgs boson and a top quark resulting in the following processes: $T\bar{T} \rightarrow HtHt$,

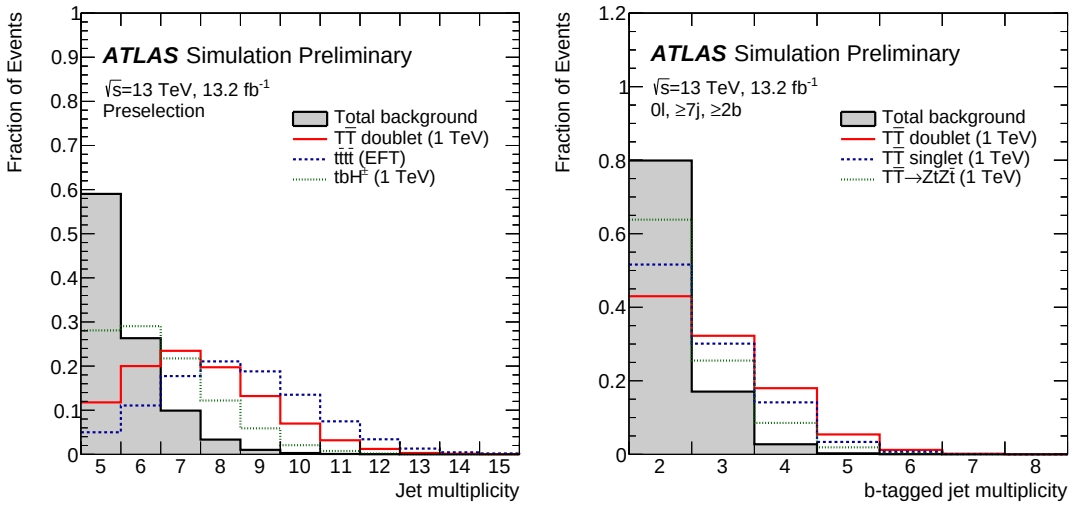

(a) (b)

Figure 4: Comparison of the shape of (a) the jet multiplicity distribution in the 1-lepton channel after preselection, and (b) the b-tag multiplicity distribution in the 0-lepton channel after preselection plus the requirement of ≥7 jets, between the total background (shaded histogram) and several signal scenarios considered in this search. The signals shown are: $T\bar{T}$ production in the weak-isospin doublet and singlet scenarios, and for BR($T \to Zt$) = 1, assuming m_T = 1 TeV; $t\bar{t}t\bar{t}$ production within an EFT model; and $tbH^{\pm}(\to tb)$ production assuming $m_{H^{\pm}}$ = 1 TeV. The last bin in both figures contains the overflow.

$HtZt$ and $HtWb$. For the dominant $H \to b\bar{b}$ decay mode, the final-state signature is characterised by high jet[8] and b-tag multiplicities, which provide a powerful experimental handle to suppress the background. The presence of high-momentum Z bosons decaying into $\nu\bar{\nu}$ or W bosons decaying leptonically, either to an electron or muon that is not reconstructed, or to a hadronically-decaying τ-lepton that is identified as a jet, yields in addition high $E_{\mathrm{T}}^{\mathrm{miss}}$, which is exploited by the 0-lepton search. Both searches have also some sensitivity to $T\bar{T} \to ZtZt$ and $ZtWb$, with $Z \to b\bar{b}$. High jet and b-tag multiplicities are also characteristic of $t\bar{t}t\bar{t}$ events (both within the SM and in BSM extensions), as well as of $b\bar{b}H(\to t\bar{t})$ $t\bar{t}H(\to t\bar{t})$ and $tbH^{\pm}(\to tb)$ production. Since most of these signal scenarios do not feature large $E_{\mathrm{T}}^{\mathrm{miss}}$, only the 1-lepton search is used to probe them, without a dedicated re-optimisation.

In Figure 4(a) the shape of the jet multiplicity distribution in the 1-lepton channel after preselection (described in Section 4) is compared between the total background and several signal scenarios, chosen to illustrate differences among various types of signals the search is sensitive to. In both the 1-lepton and 0-lepton channels, signal events have, on average, higher jet multiplicity than the background, which after preselection is dominated by $t\bar{t}$+jets processes. The higher b-quark content of signal events results in a higher b-tag multiplicity than for the background, as illustrated in Figure 4(b) for events in the 0-lepton channel after preselection plus the requirement of ≥7 jets.

Compared to Run 1, the larger centre-of-mass energy in Run 2 allows probing of higher-mass signals, which decay into boosted heavy SM particles (W and Z bosons, Higgs bosons, and top quarks), potentially giving rise to a high multiplicity of large-R jets capturing their decay products. This fact can be exploited

[8] In the following, the term "jet" is used to refer to a small-R jet, while the term "mass-tagged jet" denotes a large-R jet satisfying several kinematic criteria described in Section 3.

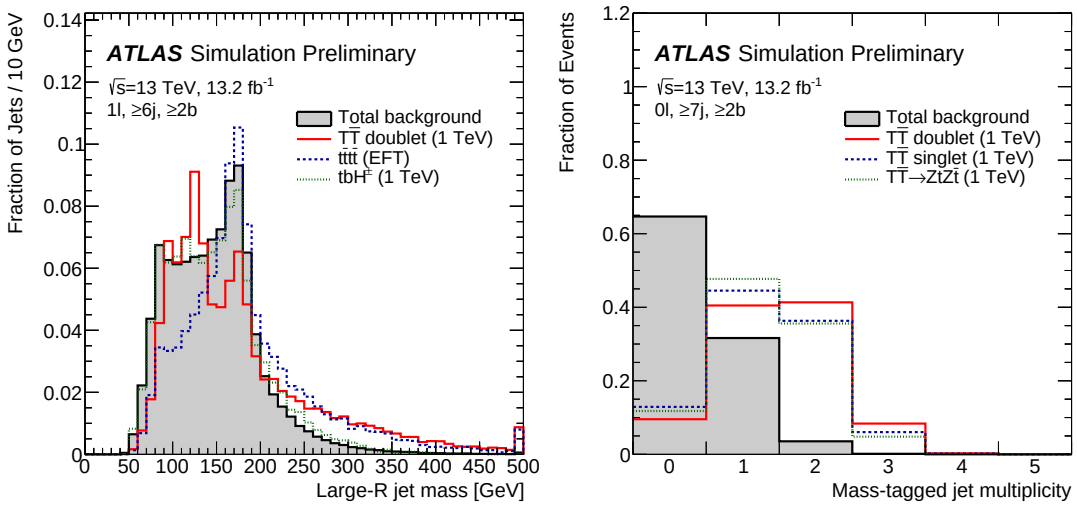

(a) (b)

Figure 5: Comparison of the shape of (a) the invariant mass distribution of selected large-R jets (prior to mass-tagging requirements), and (b) the mass-tagged jet multiplicity distribution, between the total background (shaded histogram) and several signal scenarios considered in this search. The signals shown are: $T\bar{T}$ production in the weak-isospin doublet and singlet scenarios, and for BR($T \to Zt$) = 1, assuming m_T = 1 TeV; $t\bar{t}t\bar{t}$ production within an EFT model; and $tbH^{\pm}(\to tb)$ production assuming $m_{H^{\pm}}$ = 1 TeV. The selection used in (a) corresponds to events in the 1-lepton channel satisfying the preselection requirements and ≥6 jets, whereas the selection used in (b) corresponds to events in the 0-lepton channel satisfying the preselection requirements and ≥7 jets. The last bin in both figures contains the overflow.

to further discriminate signal from background events. Figure 5(a) compares the shape of the invariant mass distribution of large-R jets satisfying the kinematic requirements described in Section 3, except for the mass requirement, between the total background and several signal scenarios. The requirement that the large-R jet mass is above 100 GeV is used in this analysis to identify boosted top-quark and Higgs-boson candidates. While $t\bar{t}$+jets events in the 1-lepton and 0-lepton channels are expected to contain up to one mass-tagged jet from a boosted, hadronically-decaying top quark, the signal events of interest are characterised by higher mass-tagged jet multiplicity, as illustrated in Figure 5(b).

In order to optimise the sensitivity of the searches, the selected events are categorised into different regions depending on the jet multiplicity (5 and ≥6 jets in the 1-lepton channel; 6 and ≥7 jets in the 0-lepton channel), b-tag multiplicity (2, 3 and ≥4) and mass-tagged jet multiplicity (0, 1 and ≥2). In the following, channels with N mass-tagged jets, n jets, and m b-tagged jets are denoted as (NJ, nj, mb). In addition, events in particular regions are further categorised by exploiting the kinematic features of the signal and the background. In the case of the $T\bar{T} \to Ht$+X signal at high values of m_T, the Higgs boson from the $T \to Ht$ decay has high p_{T}, and the $b\bar{b}$ pair from the Higgs boson decay has smaller angular separation than pairs resulting from combinatorial background. Figure 6(a) shows the distribution of the invariant mass of the two b-tagged jets with lowest ΔR separation, $m_{bb}^{\mathrm{min}\Delta R}$, for events in the (1J, ≥6j, ≥4b) region of the 1-lepton channel. This distribution, which for signal shows a clear peak near 125 GeV, allows the classification of events into two regions depleted or enriched in $T \to Ht$, $H \to b\bar{b}$ decays, by requiring $m_{bb}^{\mathrm{min}\Delta R} < 100$ GeV (referred to as "LM", standing for "low mass") or $m_{bb}^{\mathrm{min}\Delta R} > 100$ GeV (referred to as "HM", standing for "high mass"). The $m_{bb}^{\mathrm{min}\Delta R}$ variable is only used in the 1-lepton channel. In the

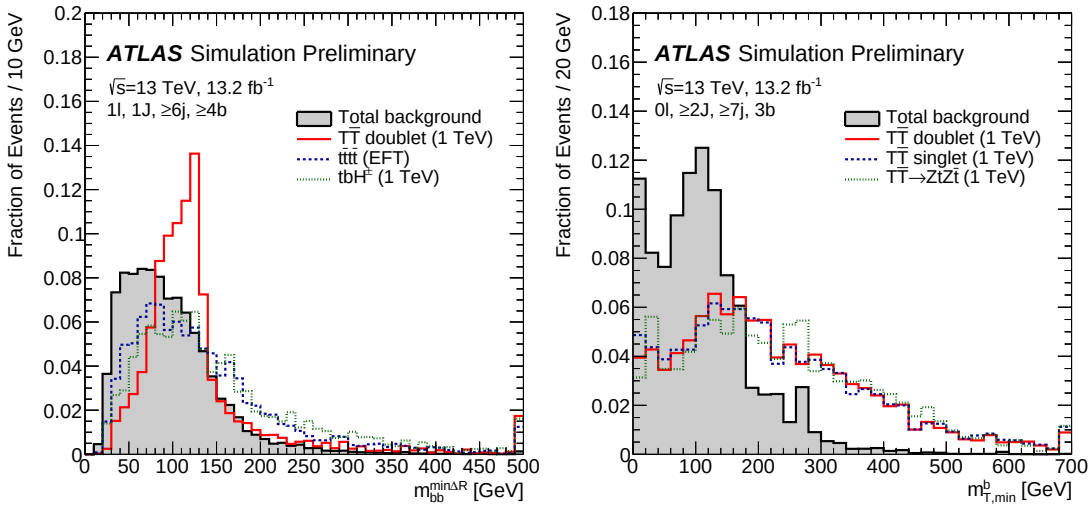

(a) (b)

Figure 6: Comparison of the shape of (a) the invariant mass distribution of the two b-tagged jets with lowest ΔR separation ($m_{bb}^{\min\Delta R}$), and (b) the distribution of the minimum transverse mass between $E_{\mathrm{T}}^{\mathrm{miss}}$ and any of the three leading b-tagged jets in the event ($m_{\mathrm{T,min}}^{b}$), between the total background (shaded histogram) and several signal scenarios considered in this search. The signals shown are: $T\bar{T}$ production in the weak-isospin doublet and singlet scenarios, and for $\mathrm{BR}(T \to Zt) = 1$, assuming $m_T = 1$ TeV; $t\bar{t}t\bar{t}$ production within an EFT model; and $tbH^{\pm}(\to tb)$ production assuming $m_{H^{\pm}} = 1$ TeV. The selection used in (a) corresponds to events in the (1J, ≥6j, ≥4b) region of the 1-lepton channel, whereas the selection used in (b) corresponds to events in the (≥2J, ≥7j, 3b) region of the 0-lepton channel. The last bin in both figures contains the overflow.

0-lepton channel, a different variable is used: $m_{\mathrm{T,min}}^{b}$, the minimum transverse mass between $E_{\mathrm{T}}^{\mathrm{miss}}$ and any of the three leading b-tagged jets in the event. This variable exhibits excellent separation between signal and background, which shows a jabobian peak around the top quark mass, as shown in Figure 6(b) for events in the (≥2J, ≥7j, ≥3b) region of the 0-lepton channel. Therefore, two regions are defined: $m_{\mathrm{T,min}}^{b} < 160$ GeV (referred to as "LM", standing for "low mass") and $m_{\mathrm{T,min}}^{b} > 160$ GeV (referred to as "HM", standing for "high mass"), the latter having a higher signal-to-background ratio than the former.

The regions with ≥6 jets (≥7 jets) are used to perform the actual search in the 1-lepton (0-lepton) channel, whereas the regions with exactly 5 jets (6 jets) are used to validate the background modelling in different regimes of event kinematics and heavy-flavour content. A total of eight search regions and six validation regions are considered in the 1-lepton channel, whereas twelve search regions and nine validation regions are considered in the 0-lepton channel, defined in Tables 2 and 3 respectively.

To further improve the separation between the $T\bar{T}$ signal and background, the distinct kinematic features of the signal are exploited. In the case of $T\bar{T}$ signal, the large T quark mass results in leptons and jets with large energy in the final state and the effective mass (m_{eff}), defined as the scalar sum of the transverse momenta of the lepton, the selected jets and the missing transverse momentum, provides a powerful discriminating variable between signal and background. In this case, the m_{eff} distribution peaks at approximately $2m_T$ for signal events and at lower values for the $t\bar{t}$+jets background. The different $t\bar{t}t\bar{t}$ signals, particularly those from BSM scenarios, also populate high values of m_{eff}, whereas signals from associated heavy Higgs boson production are typically softer in this variable. The m_{eff} distribution is used in all regions

Search regions (≥6 jets)				
Mass-tagged jet multiplicity	b-jet multiplicity	$m_{bb}^{\min\Delta R}$	m_{eff}	Channel name
0	3	-	> 400 GeV	0J, ≥6j, 3b
0	≥4	-	> 400 GeV	0J, ≥6j, ≥4b
1	3	< 100 GeV	> 700 GeV	1J, ≥6j, 3b, LM
1	3	> 100 GeV	> 700 GeV	1J, ≥6j, 3b, HM
1	≥4	< 100 GeV	> 700 GeV	1J, ≥6j, ≥4b, LM
1	≥4	> 100 GeV	> 700 GeV	1J, ≥6j, ≥4b, HM
≥2	3	-	-	≥2J, ≥6j, 3b
≥2	≥4	-	-	≥2J, ≥6j, ≥4b
Validation regions (5 jets)				
Mass-tagged jet multiplicity	b-jet multiplicity	$m_{bb}^{\min\Delta R}$	m_{eff}	Channel name
0	3	-	> 400 GeV	0J, 5j, 3b
0	≥4	-	> 400 GeV	0J, 5j, ≥4b
1	3	-	> 700 GeV	1J, 5j, 3b
1	≥4	-	> 700 GeV	1J, 5j, ≥4b
≥2	3	-	-	≥2J, 5j, 3b
≥2	≥4	-	-	≥2J, 5j, ≥4b

Table 2: Definition of the search and validation regions (see text for details) in the 1-lepton channel.

considered in this search. In the 1-lepton channel, an additional selection requirement of $m_{\text{eff}} > 400$ GeV ($m_{\text{eff}} > 700$ GeV) is made for regions with exactly zero (one) mass-tagged jets, in order to minimise the effect of a possible mismodelling of the m_{eff} distribution at low values originating from small backgrounds with large systematic uncertainties, such as multijet production. Since the $T\bar{T}$ signal is characterised by having at least one mass-tagged jet and large values of m_{eff}, this minimum requirement on m_{eff} has no impact on the search sensitivity. As an example, Figure 7 compares the m_{eff} distribution between signal and background for events in two signal-rich regions of the 0-lepton and 1-lepton channels. The kinematic requirements in these regions result in a significantly harder m_{eff} spectrum for the background than in regions without mass-tagged jets, but this variable still presents good discrimination between signal and background.

The overall rate and composition of the $t\bar{t}$+jets background strongly depends on the jet and b-tag multiplicities, as illustrated in Figure 8. The $t\bar{t}$+light-jets background is dominant in events with exactly two or three b-tagged jets. The former typically consists of events with the two b-quarks from the top quark decays being tagged, while the latter is dominated by events where in addition a charm quark from the hadronic W boson decay is tagged. Contributions from $t\bar{t}$+≥1c and $t\bar{t}$+≥1b become significant as the b-tag multiplicity increases, with the $t\bar{t}$+≥1b background being dominant for events with ≥4 b-tagged jets. The regions with different mass-tagged jet multiplicities allow probing different kinematic regimes, both soft (e.g. low-mass T quark, SM $t\bar{t}t\bar{t}$) and hard (e.g. high-mass T quark or BSM $t\bar{t}t\bar{t}$ production). The search regions with the higher multiplicities of mass-tagged jets and b-tagged jets typically have the largest signal-to-background ratio, and therefore drive the sensitivity of the search. The rest of search regions have significantly lower signal-to-background ratios, but they are useful for checking and correct-

Search regions (≥7 jets)			
Mass-tagged jet multiplicity	b-jet multiplicity	$m^b_{\mathrm{T,min}}$	Channel name
0	2	-	0J, ≥7j, 2b
0	3	-	0J, ≥7j, 3b
0	≥4	-	0J, ≥7j, ≥4b
1	2	-	1J, ≥7j, 2b
1	3	< 160 GeV	1J, ≥7j, 3b, LM
1	3	> 160 GeV	1J, ≥7j, 3b, HM
1	≥4	< 160 GeV	1J, ≥7j, ≥4b, LM
1	≥4	> 160 GeV	1J, ≥7j, ≥4b, HM
≥2	2	-	≥2J, ≥7j, 2b
≥2	3	< 160 GeV	≥2J, ≥7j, 3b, LM
≥2	3	> 160 GeV	≥2J, ≥7j, 3b, HM
≥2	≥4	-	≥2J, ≥7j, ≥4b
Validation regions (6 jets)			
Mass-tagged jet multiplicity	b-jet multiplicity	$m^b_{\mathrm{T,min}}$	Channel name
0	2	-	0J, 6j, 2b
0	3	-	0J, 6j, 3b
0	≥4	-	0J, 6j, ≥4b
1	2	-	1J, 6j, 2b
1	3	-	1J, 6j, 3b
1	≥4	-	1J, 6j, ≥4b
≥2	2	-	≥2J, 6j, 2b
≥2	3	-	≥2J, 6j, 3b
≥2	≥4	-	≥2J, 6j, ≥4b

Table 3: Definition of the search and validation regions (see text for details) in the 0-lepton channel.

ing the $t\bar{t}$+jets background prediction and constraining the related systematic uncertainties (see Section 8) through a likelihood fit to data (see Section 9). This is particularly important in the context of the $t\bar{t}$+≥1b normalisation, which is underestimated by the simulation, leading to a deficit in the prediction relative to the data that is most apparent in the channels with ≥4 b-tagged jets (see Figure 8). Such a fitting strategy was followed in the Run 1 search in the 1-lepton channel [18].[9] A summary of the observed and expected yields before the fit to data in four of the most sensitive search regions in the 1-lepton and 0-lepton channels can be found in Tables 4 and 5 respectively. The search regions shown in Table 4 for the 1-lepton channel, all requiring ≥4 b-tagged jets but with different requirements on mass-tagged multiplicity, are a selection of some of the regions with the highest $S/\sqrt{B}$ ratio (where S and B are the expected signal and background yields respectively) across several signal benchmark scenarios considered ($T\bar{T}$ in the T doublet scenario, $t\bar{t}t\bar{t}$ within SM and BSM, associated heavy Higgs boson production). Similarly, the search regions shown in Table 5 for the 0-lepton channel are a superset of the regions with the highest $S/\sqrt{B}$ ratio for different $T\bar{T}$ signal benchmark scenarios (T doublet, T singlet and BR($Z \to Ht$) = 1).

[9] In this analysis, a difference is that regions with exactly 5 jets are not included in the fit but instead used as validation regions.

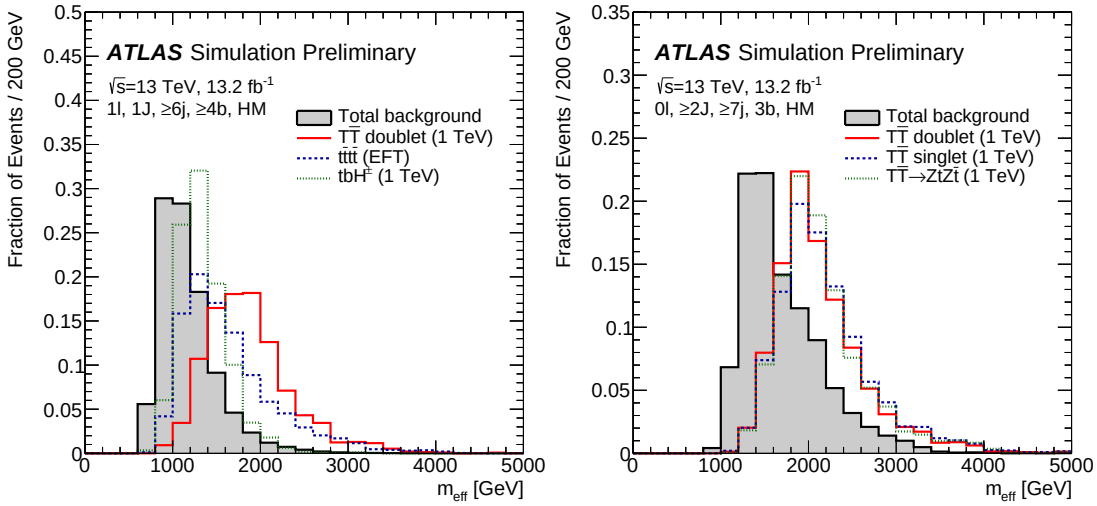

(a) (b)

Figure 7: Comparison of the shape of the distribution of the scalar sum of the transverse momenta of the lepton, the selected jets and the missing transverse momentum (m_{eff}) between the total background (shaded histogram) and several signal scenarios considered in this search. The signals shown are: $T\bar{T}$ production in the weak-isospin doublet and singlet scenarios, and for BR($T \to Zt$) = 1, assuming m_T = 1 TeV; $t\bar{t}t\bar{t}$ production within an EFT model; and $tbH^{\pm}(\to tb)$ production assuming $m_{H^{\pm}}$ = 1 TeV. The selection used in (a) corresponds to events in the (1J, ≥6j, ≥4b, HM) region of the 1-lepton channel, whereas the selection used in (b) corresponds to events in the (≥2J, ≥7j, 3b, HM) region of the 0-lepton channel. The last bin in both figures contains the overflow.

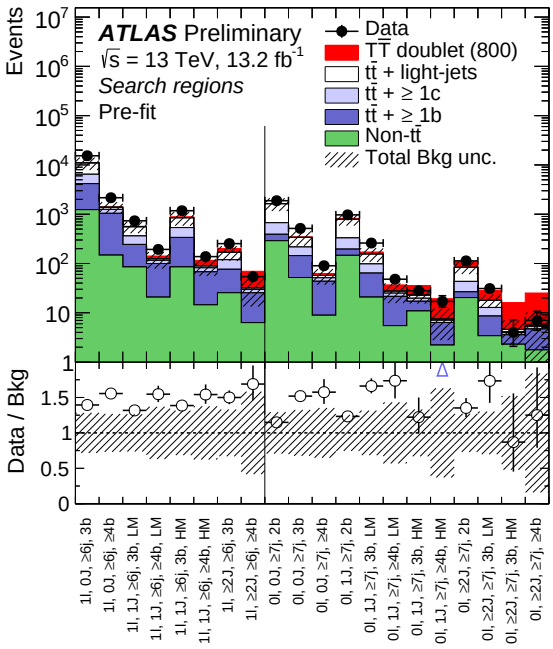

Figure 8: Comparison between the data and the background prediction for the yields in the search regions considered in the 1-lepton and 0-lepton channels, before the fit to data ("Pre-fit"). The small contributions from $t\bar{t}V$, $t\bar{t}H$, single top, W/Z+jets, diboson, and multijet backgrounds are combined into a single background source referred to as "Non-$t\bar{t}$". The expected $T\bar{T}$ signal (solid red) corresponding to $m_T = 800$ GeV in the T doublet scenario is also shown, added on top of the background prediction. The bottom panel displays the ratio of data to the SM background ("Bkg") prediction. The blue triangles indicate points that are outside the vertical range of the figure. The hashed area represents the total uncertainty on the background, excluding the normalisation uncertainty on the $t\bar{t}+ \geq 1b$ background.

1-lepton channel	0J, ≥6j, ≥4b	1J, ≥6j, ≥4b LM	1J, ≥6j, ≥4b HM	≥2J, ≥6j, ≥4b
$T\bar{T}$ (m_T = 1 TeV)				
BR($T \to Ht$) = 1	3.13 ± 0.67	4.0 ± 1.0	8.7 ± 1.6	19.2 ± 3.1
(T, B) or (X, T) doublet	2.38 ± 0.47	2.98 ± 0.56	5.04 ± 0.94	9.6 ± 1.7
T Singlet	1.24 ± 0.25	1.27 ± 0.25	2.46 ± 0.51	3.83 ± 0.73
$t\bar{t}t\bar{t}$				
EFT ($\lvert C_{4t}\rvert/\Lambda^2 = 4\pi$ TeV^{-2})	205 ± 34	105 ± 18	155 ± 29	181 ± 34
2UED/RPP (m_{KK} = 1.4 TeV)	0.31 ± 0.09	0.48 ± 0.11	2.08 ± 0.52	9.7 ± 1.9
Heavy Higgs bosons ($m_{H^\pm,H}$ = 1 TeV, σ = 1 pb)				
$b\bar{b}H(\to t\bar{t})$	42.0 ± 7.5	23.2 ± 4.2	31.2 ± 6.0	5.3 ± 1.3
$t\bar{t}H(\to t\bar{t})$	210 ± 34	162 ± 27	205 ± 35	220 ± 38
$tbH^\pm(\to tb)$	90 ± 16	29.6 ± 5.7	56 ± 11	19.7 ± 4.5
$t\bar{t}$+light-jets	136 ± 82	9.0 ± 5.3	7.8 ± 5.1	2.3 ± 1.6
$t\bar{t}$+≥1c	210 ± 130	16 ± 10	14 ± 10	4.2 ± 3.2
$t\bar{t}$+≥1b	890 ± 210	79 ± 38	53 ± 24	19 ± 14
$t\bar{t}V$	25.4 ± 9.0	4.2 ± 1.5	2.19 ± 0.80	1.21 ± 0.44
$t\bar{t}H$	51 ± 18	5.7 ± 2.0	5.7 ± 2.0	2.27 ± 0.83
W+jets	19 ± 10	3.7 ± 2.0	1.08 ± 0.56	0.56 ± 0.32
Z+jets	4.0 ± 2.2	0.41 ± 0.38	0.11 ± 0.07	0.08 ± 0.06
Single top	42 ± 15	5.0 ± 1.7	4.3 ± 1.6	1.04 ± 0.57
Diboson	3.9 ± 2.2	0.62 ± 0.47	0.06 ± 0.19	0.09 ± 0.06
$t\bar{t}t\bar{t}$ (SM)	2.88 ± 0.47	1.04 ± 0.18	1.03 ± 0.18	1.08 ± 0.19
Total background	1390 ± 370	125 ± 45	89 ± 31	32 ± 16
Data	2160	193	138	54

Table 4: Predicted and observed yields in the 1-lepton channel in four of the most-sensitive search regions (depending on the signal scenario) considered. The multijet background is estimated to be negligible in these regions and thus not shown. The background prediction is shown before the fit to data. Also shown are the signal predictions for different benchmark scenarios considered. The quoted uncertainties are the sum in quadrature of statistical and systematic uncertainties on the yields, excluding the normalisation uncertainty on the $t\bar{t}+ \geq 1b$ background.

0-lepton channel	1J, ≥7j, ≥4b HM	2J, ≥7j, ≥2b	≥2J, ≥7j, 3b HM	≥2J, ≥7j, ≥4b
$T\bar{T}$ (m_T = 1 TeV)				
BR($T \to Zt$) = 1	1.58 ± 0.42	10.2 ± 1.4	2.92 ± 0.58	1.96 ± 0.61
(T, B) or (X, T) doublet	2.44 ± 0.50	7.56 ± 0.78	3.94 ± 0.48	6.0 ± 1.1
T Singlet	0.94 ± 0.29	3.98 ± 0.41	1.62 ± 0.21	2.17 ± 0.41
$t\bar{t}$+light-jets	0.44 ± 0.26	40 ± 12	0.48 ± 0.19	0.30 ± 0.18
$t\bar{t}$+≥1c	0.70 ± 0.46	17 ± 10	0.54 ± 0.33	0.60 ± 0.40
$t\bar{t}$+≥1b	4.1 ± 3.0	6.3 ± 2.6	1.28 ± 0.45	2.93 ± 0.90
$t\bar{t}V$	0.40 ± 0.11	3.80 ± 0.80	0.40 ± 0.10	0.28 ± 0.08
$t\bar{t}H$	0.46 ± 0.11	0.66 ± 0.14	0.11 ± 0.03	0.29 ± 0.09
W+jets	0.37 ± 0.20	5.2 ± 2.4	0.32 ± 0.16	0.21 ± 0.14
Z+jets	0.32 ± 0.22	3.5 ± 1.7	0.29 ± 0.15	0.08 ± 0.11
Single top	0.37 ± 0.27	4.9 ± 3.2	0.62 ± 0.47	0.21 ± 0.19
Diboson	0.19 ± 0.21	2.1 ± 1.7	0.50 ± 0.76	0.48 ± 0.49
$t\bar{t}t\bar{t}$ (SM)	0.10 ± 0.04	0.22 ± 0.08	0.05 ± 0.02	0.20 ± 0.07
Total background	7.5 ± 3.5	84 ± 21	4.6 ± 1.5	5.6 ± 1.6
Data	17	113	4	7

Table 5: Predicted and observed yields in the 0-lepton channel in four of the most-sensitive search regions (depending on the signal scenario) considered. The multijet background is assumed to be negligible in these regions and thus not shown. The background prediction is shown before the fit to data. Also shown are the signal predictions for different benchmark scenarios considered. The quoted uncertainties are the sum in quadrature of statistical and systematic uncertainties on the yields, excluding the normalisation uncertainty on the $t\bar{t}+ \geq 1b$ background.

8. Systematic uncertainties

Several sources of systematic uncertainty are considered that affect the normalisation of signal and background and/or the shape of their m_{eff} distributions. Each source of systematic uncertainty is considered to be uncorrelated with the other sources. Correlations for a given systematic uncertainty are maintained across processes and channels.

The leading sources of systematic uncertainty vary depending on the analysis region considered. For example, the total systematic uncertainty on the background normalisation in the highest-sensitivity search region in the 1-lepton channel (≥2J, ≥6j, ≥4b) is approximately 50%, with the largest contributions originating from uncertainties on $t\bar{t}$+jets modelling (including $t\bar{t}$+HF), b-tagging efficiency, c-tagging efficiency, and light-jet tagging efficiency. The above uncertainty does not include the uncertainty on the $t\bar{t}+ \geq 1b$ normalisation, which is left free in the fit to data. However, as discussed previously, the fit to data in the eight search channels considered in the 1-lepton channel allows the overall background uncertainty to be reduced significantly, in this particular case down to approximately 16% (including the uncertainty on the $t\bar{t}+ \geq 1b$ normalisation), from the initial 50%. Such a reduction results from the significant constraints provided by the data on some systematic uncertainties, which gives rise to anti-correlations among sources of systematic uncertainty.

The following sections describe the systematic uncertainties considered in this analysis.

8.1. Luminosity

The uncertainty on the integrated luminosity is 2.9%, affecting the overall normalisation of all processes estimated from the simulation. It is derived, following a methodology similar to that detailed in Ref. [155], from a preliminary calibration of the luminosity scale using x–y beam-separation scans performed in August 2015 and May 2016.

8.2. Reconstructed objects

Uncertainties associated with leptons arise from the trigger, reconstruction, identification, and isolation efficiencies, as well as the lepton momentum scale and resolution. These are measured in data using Z, J/ψ and W events [156, 157]. The combined effect of all these uncertainties results in an overall normalisation uncertainty on signal and background of approximately 1%.

Uncertainties associated with jets arise from the jet energy scale and resolution, and the efficiency to pass the JVT requirement. The largest contribution results from the jet energy scale, whose uncertainty dependence on jet p_{T} and η is split into 18 uncorrelated sources that are treated independently in the analysis [74, 75]. It represents one of the leading sources of uncertainty associated with reconstructed objects, affecting the normalisations of $t\bar{t}$ backgrounds by approximately 12% and 16% in the most sensitive signal regions considered in the 1-lepton and 0-lepton channels, respectively.

The leading uncertainties associated with reconstructed objects in this analysis originate from the modelling of the b-, c-, and light-jet-tagging efficiencies in the simulation, which is corrected to match the efficiencies measured in data control samples [78] through dedicated scale factors. Uncertainties on these factors include a total of five independent sources affecting b-jets and four independent sources affecting c-jets. Each of these uncertainties has a different jet-p_{T} dependence. Fourteen sources of uncertainty

affecting light jets are considered, which depend on jet p_{T} and η. The above sources of systematic uncertainty are taken as uncorrelated between b-jets, c-jets, and light-jets. An additional uncertainty is included due to the extrapolation of these scale factors to jets with p_{T} beyond the kinematic reach of the data calibration samples used ($p_{\mathrm{T}} > 300$ GeV for b- and c-jets, and $p_{\mathrm{T}} > 750$ GeV for light-jets); it is taken to be correlated among the three jet flavours. Finally, an uncertainty related to the application of c-jet scale factors to τ-jets is considered, but it has a negligible impact in this analysis.

8.3. Background modelling

A number of sources of systematic uncertainty affecting the modelling of $t\bar{t}$+jets are considered. An uncertainty of +5.5%/−6.1% is assigned to the inclusive $t\bar{t}$ production cross section [88], including contributions from varying the factorisation and renormalisation scales, and from uncertainties on the PDF, α_{S}, and the top quark mass. As shown in Fig. 8, the background prediction underestimates the data in the regions dominated by $t\bar{t}$+≥1b. Although the excess is compatible with the prediction given the large uncertainties associated with $t\bar{t}$+≥1b production [158, 159], to avoid biasing the fitted $t\bar{t}$+≥1b normalisation, the associated nuisance parameter is allowed to float freely in the fit, with no prior uncertainty assumed. In the case of the $t\bar{t}$+≥1c normalisation, since the fit is unable to determine it from data and the analysis has very limited sensitivity to this uncertainty, a normalisation uncertainty of 50% is assumed.

Uncertainties affecting the modelling of $t\bar{t}$+≥1b production include shape uncertainties (including inter-category migration effects) associated with the NLO prediction from SherpaOL which is used for re-weighting the nominal Powheg-Box+Pythia $t\bar{t}$+≥1b prediction. These include three different scale variations, a different shower-recoil model scheme, and two alternative PDF sets (MSTW and NNPDF). An uncertainty on the choice of generator is assessed by comparing the $t\bar{t}$+≥1b predictions obtained after reweighting Powheg-Box+Pythia to the NLO calculation from SherpaOL and to an equivalent NLO calculation from MG5_aMC+Pythia 8. The uncertainty from the parton shower and hadronisation model is taken from the difference between the MG5_aMC calculation showered with either Pythia 8 or Herwig++. Additional uncertainties are assessed for the contributions to the $t\bar{t}$+≥1b background originating from multiple parton interactions or final-state radiation from top-quark decay products, which are not part of the NLO prediction. The latter are assessed via the alternative "radHi" and "radLow" samples, as discussed below. The nominal NLO corrections, as well as their variations used to propagate the theoretical uncertainties on the NLO prediction, are adjusted so that the particle-level cross section of the $t\bar{t}$+≥1b background (i.e. prior to reconstruction-level selection requirements) is fixed to the nominal prediction, i.e. effectively only migrations across categories and distortions to the shape of the kinematic distributions are considered. For a more detailed discussion on the above uncertainties see Ref. [131].

In the following, uncertainties affecting all $t\bar{t}$+jets processes are discussed. Uncertainties associated with the modelling of ISR/FSR are obtained from the comparison of the Powheg-Box+Pythia "radHi" and "radLow" samples (see Section 6) with the nominal Powheg-Box+Pythia sample. An uncertainty associated with the choice of NLO generator is derived by comparing two $t\bar{t}$ samples, one generated with Powheg-Box+Herwig++ and another generated with MG5_aMC+Herwig++, and propagating the resulting fractional difference to the nominal Powheg-Box+Pythia prediction. An uncertainty due to the choice of parton shower and hadronisation model is derived by comparing events produced by Powheg-Box interfaced to Pythia or Herwig++. Finally, the uncertainty on the modelling of the top-quark p_{T} is evaluated by taking the full difference between applying and not applying the reweighting to match

the NNLO prediction.[10] The above uncertainties are taken as uncorrelated between the $t\bar{t}$+light-jets, $t\bar{t}$+$\geq 1c$ and $t\bar{t}$+$\geq 1b$ processes. In the case of $t\bar{t}$+$\geq 1b$, in all instances the various HF categories and the corresponding partonic kinematics for the alternative MC samples are reweighted to match the NLO prediction of SherpaOL so that only effects other than distortions to the inter-normalisation of the various $t\bar{t}$+$\geq 1b$ topologies and their parton-level kinematics are propagated. In the case of $t\bar{t}$+light-jets and $t\bar{t}$+$\geq 1c$, the full effect of these uncertainties is propagated. Similarly to the treatment of the NLO corrections and uncertainties on $t\bar{t}$+$\geq 1b$ discussed above, in the case of the additional uncertainties derived by comparing alternative $t\bar{t}$ samples, the overall normalisation of the $t\bar{t}$+$\geq 1b$ and $t\bar{t}$+$\geq 1c$ background at the particle level is fixed to the nominal prediction. In this way, only migrations across categories and distortions to the shape of the kinematic distributions are considered. In order to maintain the inclusive $t\bar{t}$ cross section, the $t\bar{t}$+light-jets background is adjusted accordingly.

Uncertainties affecting the modelling of the single-top-quark background include a +5%/−4% uncertainty on the total cross section estimated as a weighted average of the theoretical uncertainties on t-, Wt- and s-channel production [140–142]. Additional uncertainties associated with the modelling of ISR/FSR are assessed by comparing the nominal samples with alternative samples where generator parameters have been varied (i.e. "radHi" and "radLow"). For the t- and Wt-channel processes, an uncertainty due to the choice of parton shower and hadronisation model is derived by comparing events produced by Powheg-Box interfaced to Pythia or Herwig++ (both fast simulation). These uncertainties are treated as fully correlated among single top production processes, but uncorrelated with the corresponding uncertainty on the $t\bar{t}$+jets background. An additional systematic uncertainty on Wt-channel production concerning the separation between $t\bar{t}$ and Wt at NLO [160] is assessed by comparing the nominal sample, which uses the so-called "diagram subtraction" scheme, with an alternative sample using the "diagram removal" scheme. The sum in quadrature of the above uncertainties on the single top normalisation at the preselection level is estimated to amount to 24% and 52% for the 1-lepton and 0-lepton channels, respectively. Due to the small size, and hence limited statistical precision, of the simulated samples, this uncertainty cannot be estimated in each analysis region and so the above uncertainties at the preselection level are used instead. They are treated as uncorrelated across mass-tagged multiplicity bins, resulting in a total of three independent nuisance parameters considered.

Uncertainties affecting the normalisation of the V+jets background are estimated for the sum of W+jets and Z+jets, and separately for V+light-jets, V+$\geq 1c$+jets, and V+$\geq 1b$+jets subprocesses. Agreement between data and total background prediction in the different analysis regions considered, but requiring exactly 0 b-tagged jets, which are dominated by V+light-jets, is found to be within approximately 30%, which is taken to be the total normalisation uncertainty correlated across all V+jets subprocesses. Additional 30% normalisation uncertainties are assumed for V+$\geq 1c$+jets and V+$\geq 1b$+jets subprocesses, and taken to be uncorrelated between them. These uncertainties are treated as uncorrelated across mass-tagged multiplicity bins and between the 1-lepton and 0-lepton channels. Therefore, a total of nine independent nuisance parameters per channel are considered.

Uncertainties on the diboson background normalisation include 5% from the inclusive NLO theoretical cross sections [161], which are expected to apply to events with ≥2 jets resulting from either $WV \to \ell\nu jj$ or $ZV \to \nu\bar{\nu}jj$. To extrapolate the uncertainty to higher jet multiplicities, an additional 24% normalisation uncertainty is added in quadrature for each additional inclusive jet-multiplicity bin beyond ≥2 jets, based on a comparison among different algorithms for merging LO matrix elements and parton showers [162]. Therefore, a total normalisation uncertainty of 48% is assigned for events with ≥6 jets. This uncertainty

[10] This uncertainty only affects the $t\bar{t}$+light-jets and $t\bar{t}$+$\geq 1c$ processes.

is taken to be uncorrelated across mass-tagged multiplicity bins and between the 1-lepton and 0-lepton channels. Therefore, a total of three independent nuisance parameters per channel are considered.

Uncertainties on the $t\bar{t}V$ and $t\bar{t}H$ cross sections are 15% and +9%/−13% respectively, from the uncertainties on their respective NLO theoretical cross sections [163–165]. However, in the case of the 0-lepton channel, a total uncertainty of 30% per process is assumed to account for the extrapolation to the extreme phase space of this analysis. Finally, an uncertainty of 30% is estimated for the NLO prediction of the SM $t\bar{t}t\bar{t}$ cross section [97]. Since no additional modelling uncertainties are taken into account for these backgrounds, and the 1-lepton and 0-lepton channels cover different kinematic phase space, the above uncertainties on the $t\bar{t}V$, $t\bar{t}H$, and SM $t\bar{t}t\bar{t}$ cross sections are taken to be uncorrelated between both channels.

Uncertainties on the data-driven multijet background estimate receive contributions from the limited sample size in data, particularly at high jet and b-tag multiplicities, as well as from the uncertainty on the misidentified-lepton rate, measured in different control regions (e.g. selected with a requirement on either the maximum $E_{\mathrm{T}}^{\mathrm{miss}}$ or m_{T}^{W}). The uncertainty on the misidentified-lepton rate results in a normalisation uncertainty of 50%, which is taken as correlated across jet and b-tag multiplicity bins. No explicit shape uncertainty is assigned since the large statistical uncertainties associated with the multijet background prediction, which are uncorrelated between bins in the final discriminant distribution, effectively cover possible shape uncertainties.

9. Statistical analysis

For a given search, the m_{eff} distributions across all search regions considered are jointly analysed to test for the presence of a signal in each of the benchmark scenarios being tested. The statistical analysis is based on a binned likelihood function $\mathcal{L}(\mu, \theta)$ constructed as a product of Poisson probability terms over all bins considered in the analysis. This function depends on the signal-strength parameter μ, a multiplicative factor to the predicted production cross section for signal, and θ, a set of nuisance parameters that encode the effect of systematic uncertainties on the signal and background expectations and are implemented in the likelihood function as Gaussian or log-normal constraints. Therefore, the total number of expected events in a given bin depends on μ and θ. The nuisance parameters θ allow variations of the expectations for signal and background according to the corresponding systematic uncertainties, and their fitted values correspond to the deviations from the nominal expectations that globally provide the best fit to the data. This procedure allows a reduction of the impact of systematic uncertainties on the search sensitivity by taking advantage of the highly populated background-dominated channels included in the likelihood fit. It requires a good understanding of the systematic effects affecting the shapes of the m_{eff} distributions. Detailed validation studies of the fitting procedure have been performed using the simulation. To verify the improved background prediction, fits under the background-only hypothesis are performed, and differences between the data and the post-fit background prediction are checked for kinematic variables other than the ones used in the fit, as well as for the m_{eff} distributions in validation regions not used in the fit. Uncertainties in each bin of the predicted m_{eff} distributions due to the finite statistical precision of the simulated samples are also taken into account by dedicated parameters in the fit.

The test statistic q_μ is defined as the profile likelihood ratio: $q_\mu = -2\ln(\mathcal{L}(\mu, \hat{\hat{\theta}}_\mu)/\mathcal{L}(\hat{\mu}, \hat{\theta}))$, where $\hat{\mu}$ and $\hat{\theta}$ are the values of the parameters that maximise the likelihood function (with the constraint $0 \leq \hat{\mu} \leq \mu$), and $\hat{\hat{\theta}}_\mu$ are the values of the nuisance parameters that maximise the likelihood function for a given value of μ. The test statistic q_μ is evaluated with the RooFit package [166, 167] and is used to measure the

compatibility of the observed data with the background-only hypothesis (i.e. the discovery test) by setting $\mu = 0$ in the profile likelihood ratio: $q_0 = -2\ln(\mathcal{L}(0,\hat{\hat{\theta}}_0)/\mathcal{L}(\hat{\mu},\hat{\theta}))$. The p-value (referred to as p_0) representing the compatibility of the data with the background-only hypothesis is estimated by integrating the distribution of q_0 from background-only pseudo-experiments, approximated using the asymptotic formulae given in Ref. [168, 169], above the observed value of q_0. Some model dependence exists in the estimation of the p_0, as a given signal scenario needs to be assumed in the calculation of the denominator of q_μ, even if the overall signal normalisation is left floating and fitted to data. The observed p_0 is checked for each explored signal scenario. Upper limits on the signal production cross section for each of the signal scenarios considered are derived by using q_μ in the CL_s method [170, 171]. For a given signal scenario, values of the production cross section (parameterised by μ) yielding CL_s<0.05, where CL_s is computed using the asymptotic approximation [168, 169], are excluded at ≥95% CL.

10. Results

This section presents the results obtained for searches in the 1-lepton and 0-lepton channel, as well as their combination, following the statistical analysis discussed in Section 9. The 1-lepton and 0-lepton channels are combined to more sensitively search for $T\bar{T}$ production. Only the 1-lepton search is used to probe the different $t\bar{t}t\bar{t}$ and associated heavy Higgs boson production signals.

10.1. Likelihood fits to data

A binned likelihood fit under the background-only hypothesis is performed on the m_{eff} distributions in all search regions considered. In this section, the results of the simultaneous likelihood fit to the search regions in the 1-lepton and 0-lepton channels, which is used to obtain combined results on $T\bar{T}$ production, are discussed. In this combined fit all common systematic uncertainties are considered fully correlated between the 1-lepton and 0-lepton channels, with the exception of those affecting non-$t\bar{t}$ backgrounds. The reason is that both channels cover a different kinematic phase space and non-$t\bar{t}$ backgrounds have a more simplified description of their modelling uncertainties. To obtain the results in the individual channels, separate fits are performed. In general, good consistency is found among the fitted nuisance parameters in the individual and combined fits.

A comparison of the distribution of observed and expected yields in the search regions in the 1-lepton and 0-lepton after the combined fit, is shown in Figure 9. For comparison, the corresponding comparison before the combined fit can be found in Figure 8. The post-fit yields in four of the most sensitive search regions in the 1-lepton and 0-lepton channels can be found in Tables 6 and 7 respectively. For the same search regions, the corresponding m_{eff} distributions, both pre- and post-fit to data, are shown in Figures 10-13. The large number of events in the signal-depleted regions, together with their different background compositions, and the assumptions of the fit model, allows to constrain the combined effect of several sources of systematic uncertainty. As a result, an improved background prediction is obtained with significantly reduced uncertainty, not only in the signal-depleted channels, but also in the signal-rich channels such as (≥2J, ≥6j, ≥4b) in the 1-lepton channel. In the combined fit, the channels with two b-tagged jets are used to constrain the leading uncertainties affecting the $t\bar{t}$+light-jets background prediction, while the channels with ≥3 b-tagged jets are sensitive to the uncertainties affecting the $t\bar{t}$+HF background prediction. In particular, one of the main corrections applied by the fit is an increase of the $t\bar{t}$+≥1b normalisation by a factor of 1.2 ± 0.3 relative to the nominal prediction by adjusting the corresponding

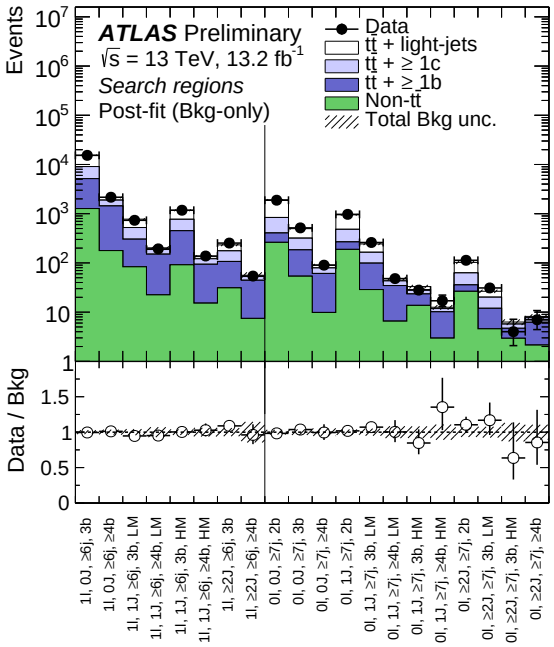

Figure 9: Comparison between the data and the background prediction for the yields in the search regions considered in the 1-lepton and 0-lepton channels, after the combined fit to data ("Post-fit") under the background-only hypothesis. The small contributions from $t\bar{t}V$, $t\bar{t}H$, single top, W/Z+jets, diboson, and multijet backgrounds are combined into a single background source referred to as "Non-$t\bar{t}$". The bottom panel displays the ratio of data to the SM background ("Bkg") prediction. The hashed area represents the total uncertainty on the background.

nuisance parameter.[11] In addition, the nuisance parameter controlling the $t\bar{t}$+≥1c normalisation is adjusted to scale this background by a factor of 1.5 ± 0.4 relative to its nominal prediction. The fit results in an improved agreement between data and prediction in the channels with ≥3 b-tagged jets, where the $t\bar{t}$+HF background dominates. Detailed studies have been performed to verify the stability of the fit against variations in the treatment of the systematic uncertainties affecting the $t\bar{t}$+HF background (e.g. by decorrelating normalisation and shape uncertainties between different $t\bar{t}$+≥1b categories, or by scaling the $t\bar{t}$+≥1b and $t\bar{t}$+≥1c backgrounds by a common factor), finding in all instances a robust post-fit background prediction. Though there is no explicit term directly responsible for the normalisation of $t\bar{t}$+light-jets background, the yields for this contribution within each region are affected by systematic uncertainties on the $t\bar{t}$ modelling and the jet flavour tagging, and thus change after the fit.

A comparison of the distribution of observed and expected yields in all validation regions considered, before and after the combined fit in the search regions, is shown in Figure 14. The agreement between data and prediction in normalisation and shape of the m_{eff} distribution for these regions, which are not used in the fit, is generally improved after the fit, giving confidence in the overall procedure. Comparisons between data and background prediction, before and after the fit, for a number of kinematic variables used to define the analysis strategy can be found in Appendix A. Although these variables are not directly used in the fit, a significantly improved description of the data by the post-fit background prediction is observed, which further validates the fitting procedure.

[11] The overall change in $t\bar{t}$+≥1b normalisation can be different across channels due to the different impact of other nuisance parameters affecting the $t\bar{t}$+≥1b background, such as those related to $t\bar{t}$+≥1b modelling.

1-lepton channel	0J, ≥6j, ≥4b	1J, ≥6j, ≥4b LM	1J, ≥6j, ≥4b HM	≥2J, ≥6j, ≥4b
$t\bar{t}$+light-jets	250 ± 100	15.7 ± 6.6	13.0 ± 6.2	3.3 ± 1.7
$t\bar{t}$+≥1c	450 ± 150	37 ± 12	28 ± 10	8.5 ± 3.3
$t\bar{t}$+≥1b	1260 ± 130	128 ± 17	79 ± 10	36.9 ± 7.7
$t\bar{t}V$	30 ± 10	4.7 ± 1.5	2.54 ± 0.85	1.33 ± 0.44
$t\bar{t}H$	57 ± 18	6.3 ± 2.1	5.9 ± 2.0	2.28 ± 0.76
W+jets	26 ± 11	3.6 ± 1.6	1.05 ± 0.45	0.85 ± 0.41
Z+jets	5.3 ± 2.3	0.49 ± 0.37	0.12 ± 0.06	0.16 ± 0.09
Single top	52 ± 14	5.4 ± 1.5	4.4 ± 1.3	1.61 ± 0.70
Diboson	4.6 ± 2.4	0.76 ± 0.51	0.09 ± 0.20	0.10 ± 0.06
$t\bar{t}t\bar{t}$ (SM)	3.2 ± 1.0	1.17 ± 0.38	1.09 ± 0.36	1.11 ± 0.36
Total background	2135 ± 79	203 ± 15	134.3 ± 8.7	56.2 ± 8.3
Data	2160	193	138	54

Table 6: Predicted and observed yields in the 1-lepton channel in four of the most-sensitive search regions considered. The multijet background is considered negligible in these regions and thus not shown. The background prediction is shown after the combined fit to data in the 0-lepton and 1-lepton channels under the background-only hypothesis. The quoted uncertainties are the sum in quadrature of statistical and systematic uncertainties on the yields, computed taking into account correlations among nuisance parameters and among processes.

0-lepton channel	1J, ≥7j, ≥4b HM	2J, ≥7j, ≥2b	≥2J, ≥7j, 3b HM	≥2J, ≥7j, ≥4b
$t\bar{t}$+light-jets	0.76 ± 0.31	39.7 ± 6.7	0.58 ± 0.16	0.50 ± 0.21
$t\bar{t}$+≥1c	1.66 ± 0.55	27 ± 10	1.02 ± 0.36	1.47 ± 0.52
$t\bar{t}$+≥1b	7.2 ± 1.5	9.3 ± 2.8	1.75 ± 0.47	4.08 ± 0.83
$t\bar{t}V$	0.52 ± 0.11	3.86 ± 0.63	0.48 ± 0.09	0.33 ± 0.07
$t\bar{t}H$	0.50 ± 0.09	0.71 ± 0.10	0.12 ± 0.02	0.33 ± 0.07
W+jets	0.58 ± 0.25	7.0 ± 2.6	0.44 ± 0.18	0.30 ± 0.16
Z+jets	0.56 ± 0.25	4.9 ± 1.9	0.40 ± 0.17	0.10 ± 0.12
Single top	0.55 ± 0.31	6.6 ± 3.4	0.90 ± 0.54	0.36 ± 0.24
Diboson	0.13 ± 0.15	3.2 ± 2.0	0.55 ± 0.63	0.49 ± 0.47
$t\bar{t}t\bar{t}$ (SM)	0.11 ± 0.04	0.23 ± 0.08	0.05 ± 0.02	0.22 ± 0.07
Total background	12.6 ± 1.4	102.3 ± 7.0	6.3 ± 1.0	8.2 ± 1.0
Data	17	113	4	7

Table 7: Predicted and observed yields in the 0-lepton channel in four of the most-sensitive search regions considered. The multijet background is considered negligible in these regions and thus not shown. The background prediction is shown after the combined fit to data in the 0-lepton and 1-lepton channels under the background-only hypothesis. The quoted uncertainties are the sum in quadrature of statistical and systematic uncertainties on the yields, computed taking into account correlations among nuisance parameters and among processes.

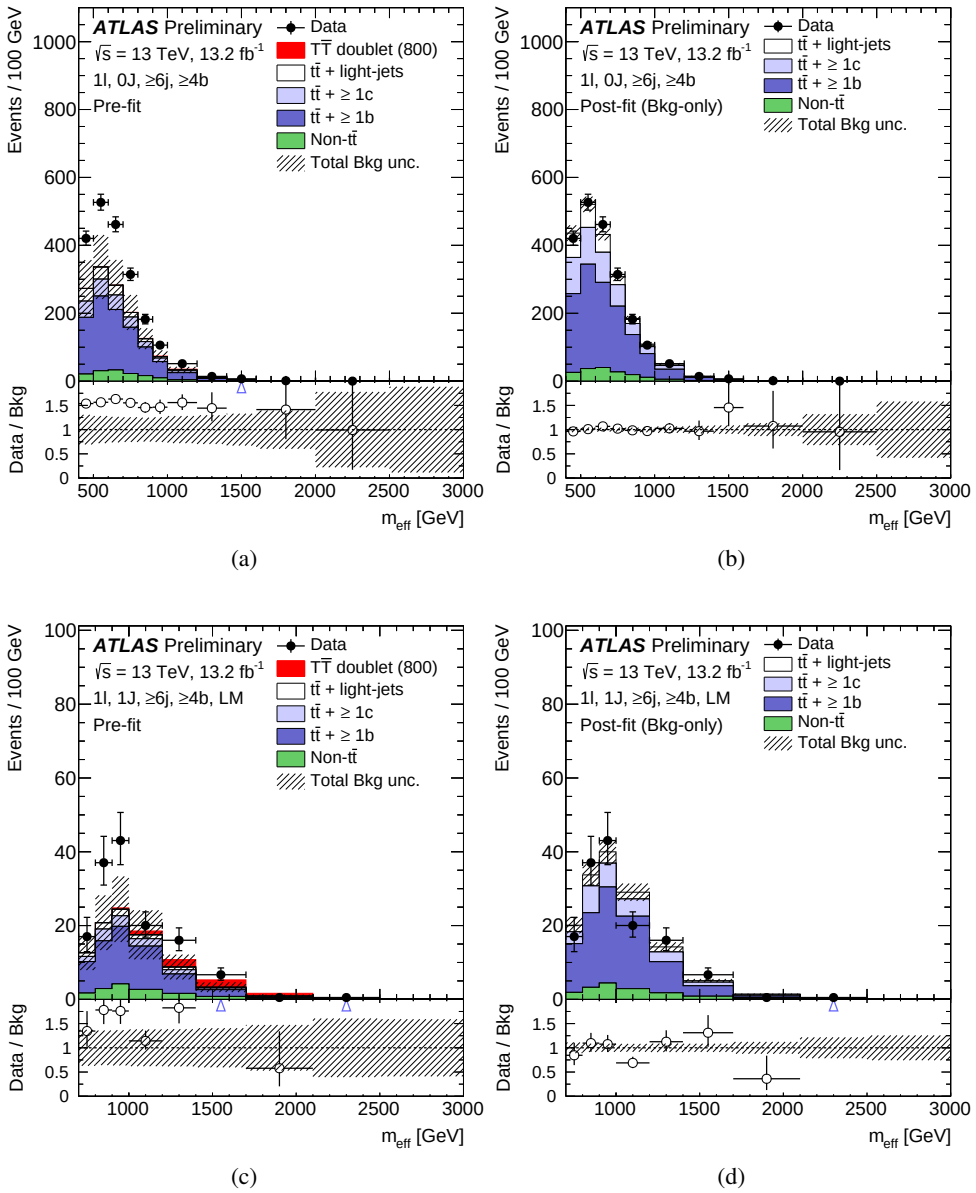

Figure 10: Comparison between the data and prediction for the m_{eff} distribution in some of the most-sensitive search regions in the 1-lepton channel, before and after performing the combined fit to data in the 0-lepton and 1-lepton channels ("Pre-fit" and "Post-fit", respectively) under the background-only hypothesis. Shown are the (0J, ≥6j, ≥4b) region (a) pre-fit and (b) post-fit, and the (1J, ≥6j, ≥4b, LM) region (c) pre-fit and (d) post-fit. In the pre-fit figures the expected $T\bar{T}$ signal (solid red) corresponding to $m_T = 800$ GeV in the T doublet scenario is also shown, added on top of the background prediction. The small contributions from $t\bar{t}V$, $t\bar{t}H$, single top, W/Z+jets, diboson, and multijet backgrounds are combined into a single background source referred to as "Non-$t\bar{t}$". The last bin in all figures contains the overflow. The bottom panels display the ratios of data to the total background prediction ("Bkg"). The blue triangles indicate points that are outside the vertical range of the figure. The hashed area represents the total uncertainty on the background. In the case of the pre-fit background uncertainty, the normalisation uncertainty on the $t\bar{t}+ \geq 1b$ background is not included.

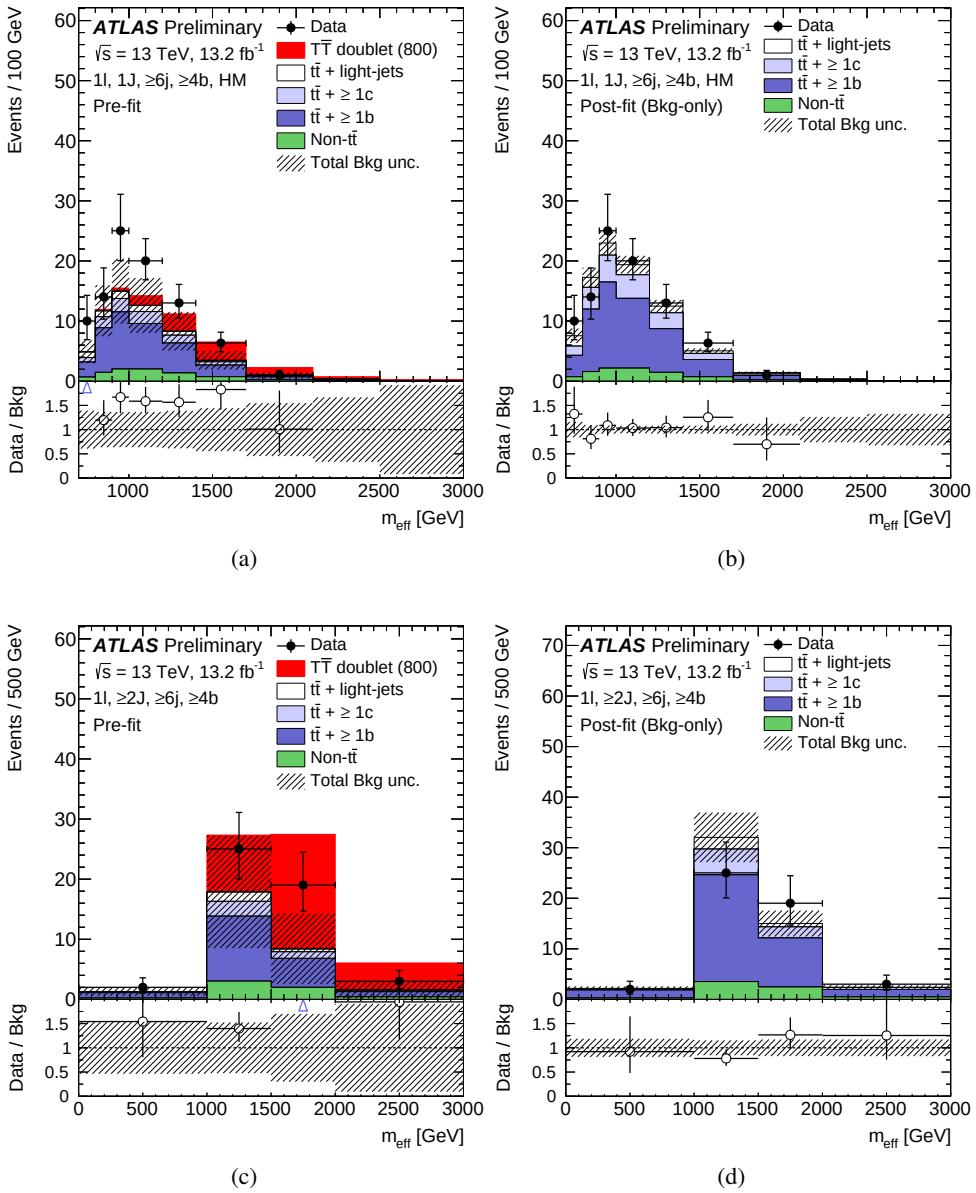

Figure 11: Comparison between the data and prediction for the m_{eff} distribution in some of the most-sensitive search regions in the 1-lepton channel, before and after performing the combined fit to data in the 0-lepton and 1-lepton channels ("Pre-fit" and "Post-fit", respectively) under the background-only hypothesis. Shown are the (1J, ≥6j, ≥4b, HM) region (a) pre-fit and (b) post-fit, and the (≥2J, ≥6j, ≥4b) region (c) pre-fit and (d) post-fit. In the pre-fit figures the expected $T\bar{T}$ signal (solid red) corresponding to $m_T = 800$ GeV in the T doublet scenario is also shown, added on top of the background prediction. The small contributions from $t\bar{t}V$, $t\bar{t}H$, single top, W/Z+jets, diboson, and multijet backgrounds are combined into a single background source referred to as "Non-$t\bar{t}$". The last bin in all figures contains the overflow. The bottom panels display the ratios of data to the total background prediction ("Bkg"). The blue triangles indicate points that are outside the vertical range of the figure. The hashed area represents the total uncertainty on the background. In the case of the pre-fit background uncertainty, the normalisation uncertainty on the $t\bar{t}+ \geq 1b$ background is not included.

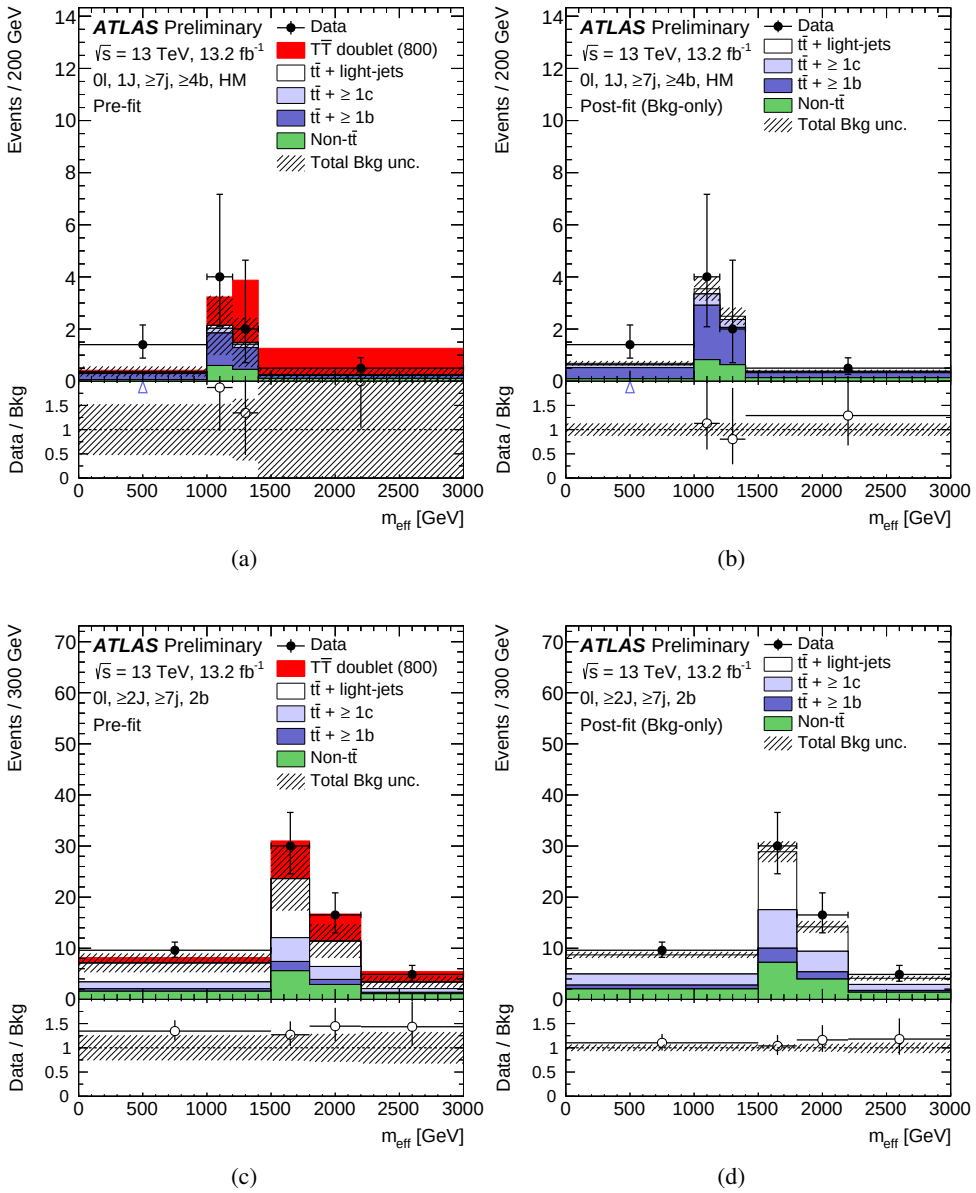

Figure 12: Comparison between the data and prediction for the m_{eff} distribution in some of the most-sensitive search regions in the 0-lepton channel, before and after performing the combined fit to data in the 0-lepton and 1-lepton channels ("Pre-fit" and "Post-fit", respectively) under the background-only hypothesis. Shown are the (1J, ≥7j, ≥4b, HM) region (a) pre-fit and (b) post-fit, and the (≥2J, ≥7j, ≥2b) region (c) pre-fit and (d) post-fit. In the pre-fit figures the expected $T\bar{T}$ signal (solid red) corresponding to $m_T = 800$ GeV in the T doublet scenario is also shown, added on top of the background prediction. The small contributions from $t\bar{t}V$, $t\bar{t}H$, single top, W/Z+jets, diboson, and multijet backgrounds are combined into a single background source referred to as "Non-$t\bar{t}$". The last bin in all figures contains the overflow. The bottom panels display the ratios of data to the total background prediction ("Bkg"). The blue triangles indicate points that are outside the vertical range of the figure. The hashed area represents the total uncertainty on the background. In the case of the pre-fit background uncertainty, the normalisation uncertainty on the $t\bar{t}+ \geq 1b$ background is not included.

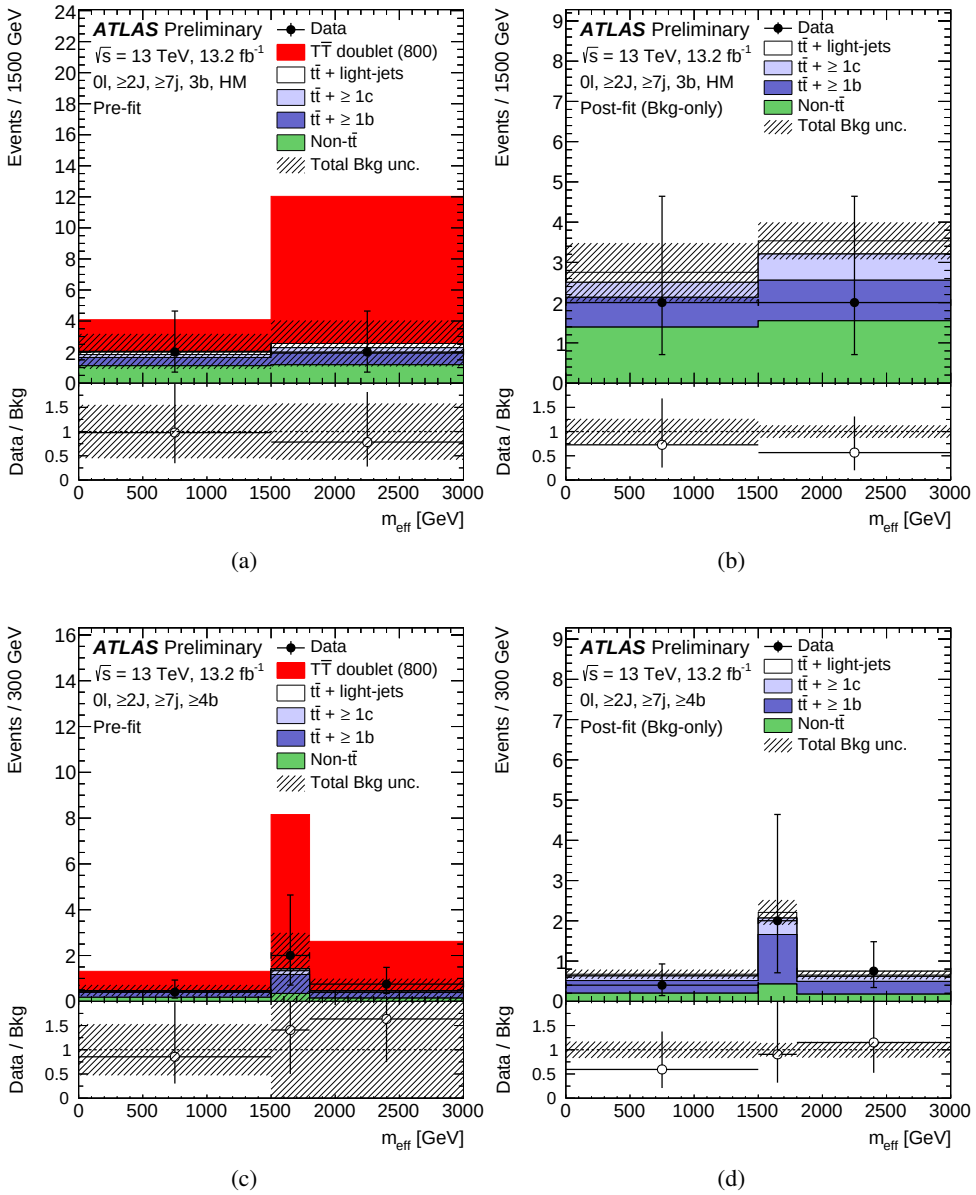

Figure 13: Comparison between the data and prediction for the m_{eff} distribution in some of the most-sensitive search regions in the 0-lepton channel, before and after performing the combined fit to data in the 0-lepton and 1-lepton channels ("Pre-fit" and "Post-fit", respectively) under the background-only hypothesis. Shown are the (≥2J, ≥7j, ≥3b, HM) region (a) pre-fit and (b) post-fit, and the (≥2J, ≥7j, ≥4b) region (c) pre-fit and (d) post-fit. In the pre-fit figures the expected $T\bar{T}$ signal (solid red) corresponding to $m_T = 800$ GeV in the T doublet scenario is also shown, added on top of the background prediction. The small contributions from $t\bar{t}V$, $t\bar{t}H$, single top, W/Z+jets, diboson, and multijet backgrounds are combined into a single background source referred to as "Non-$t\bar{t}$". The last bin in all figures contains the overflow. The bottom panels display the ratios of data to the total background prediction ("Bkg"). The hashed area represents the total uncertainty on the background. In the case of the pre-fit background uncertainty, the normalisation uncertainty on the $t\bar{t}+ \geq 1b$ background is not included.

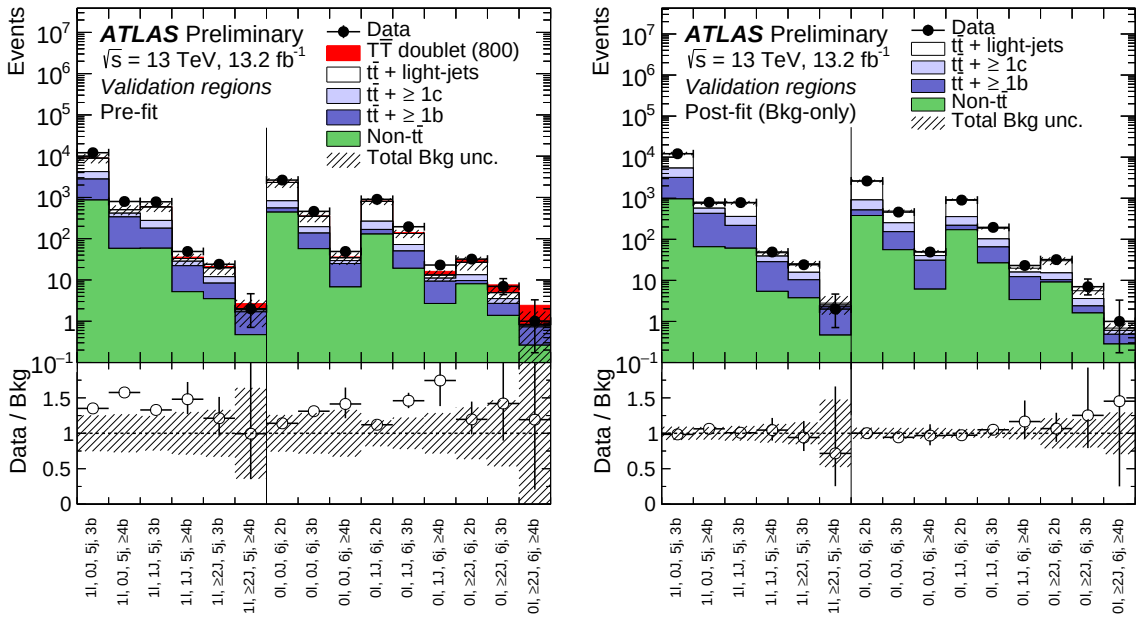

(a) (b)

Figure 14: Comparison between the data and background prediction for the yields in each of the validation regions considered in the 1-lepton and 0-lepton channels (a) before the fit ("Pre-fit") and (b) after the fit ("Post-fit"). The fit is performed on the data in 1-lepton and 0-lepton channels under the background-only hypothesis considering only the search regions. In the pre-fit figure the expected $T\bar{T}$ signal (solid red) corresponding to $m_T = 800$ GeV in the T doublet scenario is also shown, added on top of the background prediction. The small contributions from $t\bar{t}V$, $t\bar{t}H$, single top, W/Z+jets, diboson, and multijet backgrounds are combined into a single background source referred to as "Non-$t\bar{t}$". The bottom panels display the ratios of data to the total background prediction ("Bkg"). The hashed area represents the total uncertainty on the background. In the case of the pre-fit background uncertainty, the normalisation uncertainty on the $t\bar{t}+ \geq 1b$ background is not included.

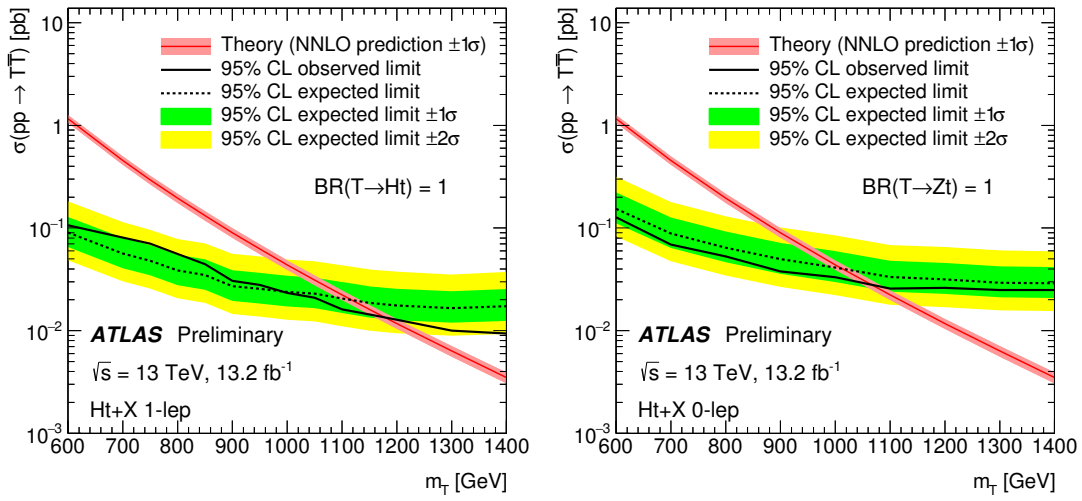

(a) (b)

Figure 15: Observed (solid line) and expected (dashed line) 95% CL upper limits on the $T\bar{T}$ cross section as a function of the T quark mass for (a) the 1-lepton search under the assumption BR($T \to Ht$) = 1, and (b) the 0-lepton search under the assumption BR($T \to Zt$) = 1. The surrounding shaded bands correspond to ±1 and ±2 standard deviations around the expected limit. The thin red line and band show the theoretical prediction and its ±1 standard deviation uncertainty.

10.2. Limits on vector-like quark pair production

Upper limits at 95% CL on the $T\bar{T}$ production cross section are set in several benchmark scenarios as a function of the T quark mass m_T and are compared to the theoretical prediction from Top++. The resulting lower limits on m_T correspond to the central value of the theoretical cross section. The scenarios considered involve different assumptions on the decay branching ratios. The search in the 1-lepton (0-lepton) channel is particularly sensitive to the benchmark scenario of BR($T \to Ht$) = 1 (BR($T \to Zt$) = 1). The cross section limits obtained as a function of mass for the above benchmark scenarios are shown as a function of the T quark mass in Figure 15. Both the 1-lepton and the 0-lepton searches have comparable sensitivity to the weak-isospin doublet and singlet scenarios. Therefore, their combination represents an improvement of 50–70 GeV on the expected T quark mass exclusion over the individual searches. The corresponding limits obtained for the combination are shown in Figure 16. A summary of the observed and expected upper limits on the T quark mass in the different benchmark scenarios is given in Table 8, including a comparison to the limits obtained by previous $T\bar{T} \to Ht$+X searches in the 1-lepton channel. As can be appreciated, the current results extend the sensitivity of previous searches by ~200–300 GeV, depending on the assumed benchmark scenario.

The same analyses are used to derive exclusion limits on vector-like T quark production, for different values of m_T and as a function of BR($T \to Wb$) and BR($T \to Ht$). To probe this branching ratio plane, the signal samples are reweighted by the ratio of the desired branching ratio to the original branching ratio in Protos, and the complete analysis is repeated. Figure 17 shows the 95% CL exclusion limits obtained by the individual 1-lepton and 0-lepton searches for different values of m_T, overlaid to highlight their complementarity in probing the branching ratio plane. As a result, their combination represents a significant improvement over the individual results, as illustrated in Figure 18. In this case, the observed

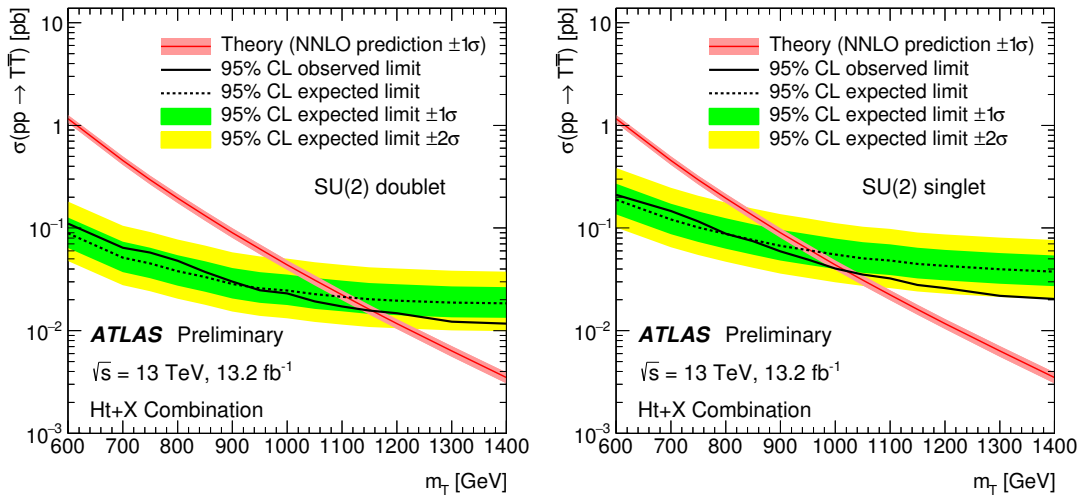

(a) (b)

Figure 16: Observed (solid line) and expected (dashed line) 95% CL upper limits on the $T\bar{T}$ cross section as a function of the T quark mass for the combination of the 1-lepton and 0-lepton searches (a) for a T quark doublet, and (b) for a T quark singlet. The surrounding shaded bands correspond to ±1 and ±2 standard deviations around the expected limit. The thin red line and band show the theoretical prediction and its ±1 standard deviation uncertainty.

95% CL lower limits on T quark mass [GeV]				
Search	BR($T \to Ht$) = 1	BR($T \to Zt$) = 1	Doublet	Singlet
1-lepton channel	1180 (1120)	740 (820)	1060 (1000)	900 (880)
0-lepton channel	1090 (1070)	1060 (1010)	1090 (1060)	950 (890)
Combination	**1200 (1160)**	**1100 (1040)**	**1160 (1110)**	**1020 (960)**

Previous ATLAS $T\bar{T} \to Ht$+X searches (1-lepton)					Ref.
Run 2 (3.2 fb^{-1})	900 (980)	700 (740)	800 (900)	750 (780)	[24]
Run 1	950 (880)	750 (690)	860 (820)	760 (720)	[18]

Table 8: Summary of observed (expected) 95% CL lower limits on T quark mass (in GeV) for the 1-lepton and 0-lepton channels, as well as their combination, under different assumptions on the decay branching ratios. Also shown are the corresponding limits obtained by previous ATLAS $T\bar{T} \to Ht$+X searches in the 1-lepton channel [18, 24].

lower limits on the T quark mass range between 810 GeV and 1200 GeV depending on the values of the branching ratios into the three decay modes. In particular, a vector-like T quark with mass below 810 GeV is excluded for any values of the branching ratios into the three decay modes. The corresponding range of expected lower limits is between 730 GeV and 1160 GeV. Figure 19 present the corresponding observed and expected T quark mass limits in the plane of BR($T \to Ht$) versus BR($T \to Wb$), obtained by linear interpolation of the calculated CL_s versus m_T.

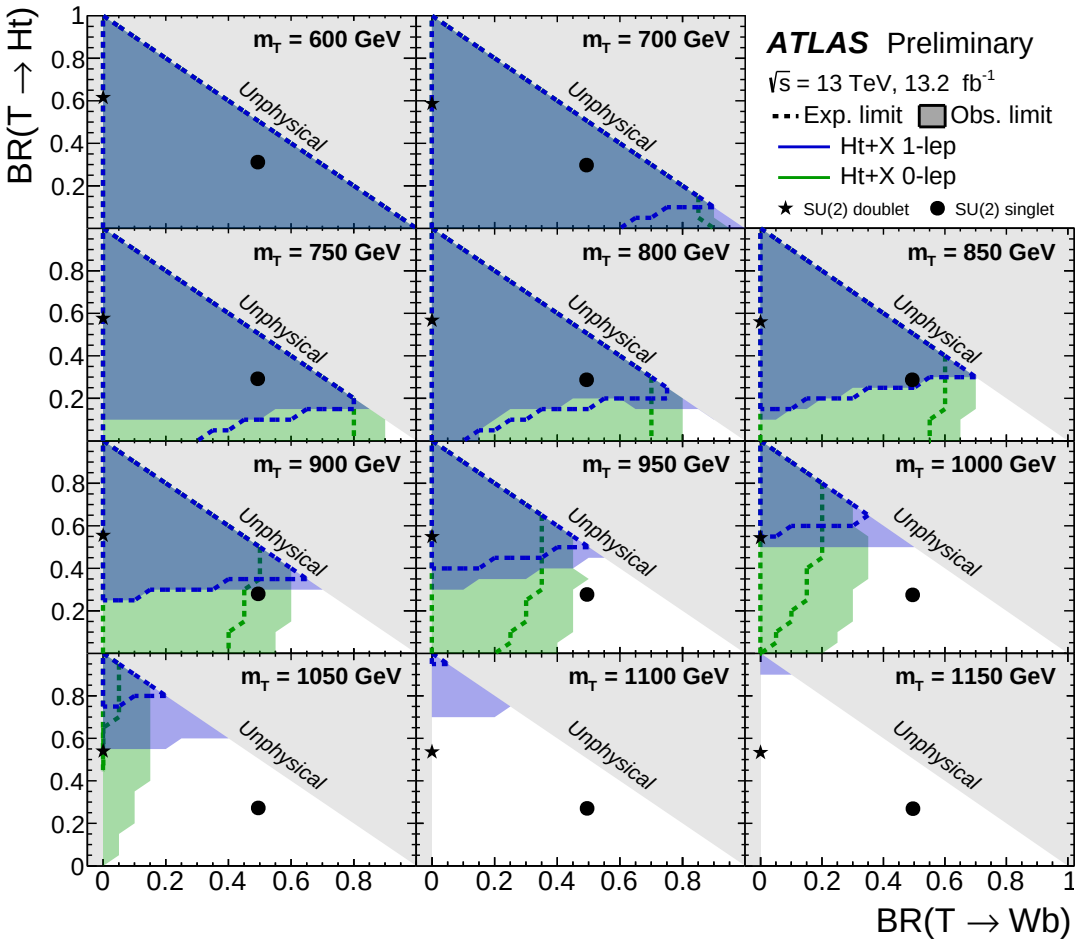

Figure 17: Observed (filled area) and expected dashed line) 95% CL exclusion in the plane of BR($T \to Wb$) versus BR($T \to Ht$), for different values of the vector-like T quark mass, overlaid for the 1-lepton (blue) and 0-lepton (green) searches. The grey (light shaded) area corresponds to the unphysical region where the sum of branching ratios exceeds unity, or is smaller than zero. The default branching ratio values from the Protos event generator for the weak-isospin singlet and doublet cases are shown as plain circle and star symbols respectively.

Additional figures for the individual searches can be found in Appendix B.

10.3. Limits on four-top-quark production

The 1-lepton search is used to set limits on four-top-quark production considering different signal benchmark scenarios: SM $t\bar{t}t\bar{t}$, $t\bar{t}t\bar{t}$ via an EFT model with a four-top-quark contact interaction, and $t\bar{t}t\bar{t}$+X via the 2UED/RPP model (see Sect. 5 for details). In the case of $t\bar{t}t\bar{t}$ production with the SM kinematics, the observed (expected) 95% CL upper limit on the production cross section is 130 fb (110 fb), or 15 (12) times the SM prediction (assumed to be 9.2 fb).

In the case of $t\bar{t}t\bar{t}$ production via an EFT model with a four-top contact interaction, the observed (expected) 95% CL upper limit on the production cross section is 51 fb (54 fb). The improved sensitivity in the case of the EFT model results from the harder m_{eff} spectrum compared to that of SM $t\bar{t}t\bar{t}$ production. The

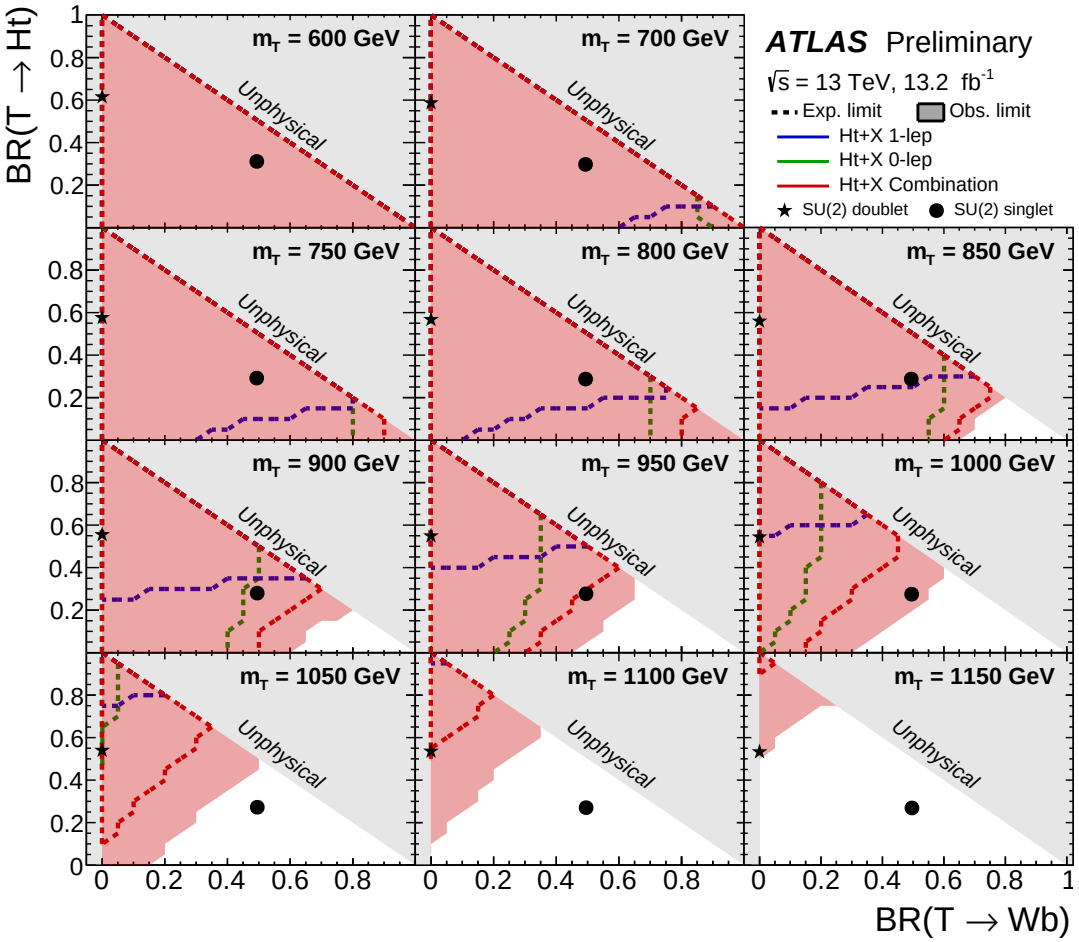

Figure 18: Observed (red filled area) and expected (red dashed line) 95% CL exclusion in the plane of BR($T \to Wb$) versus BR($T \to Ht$), for different values of the vector-like T quark mass for the combination of the 1-lepton and 0-lepton searches. Also shown are the expected exclusions by the individual searches, which can be compared to that obtained through their combination. The grey (light shaded) area corresponds to the unphysical region where the sum of branching ratios exceeds unity, or is smaller than zero. The default branching ratio values from the Protos event generator for the weak-isospin singlet and doublet cases are shown as plain circle and star symbols respectively.

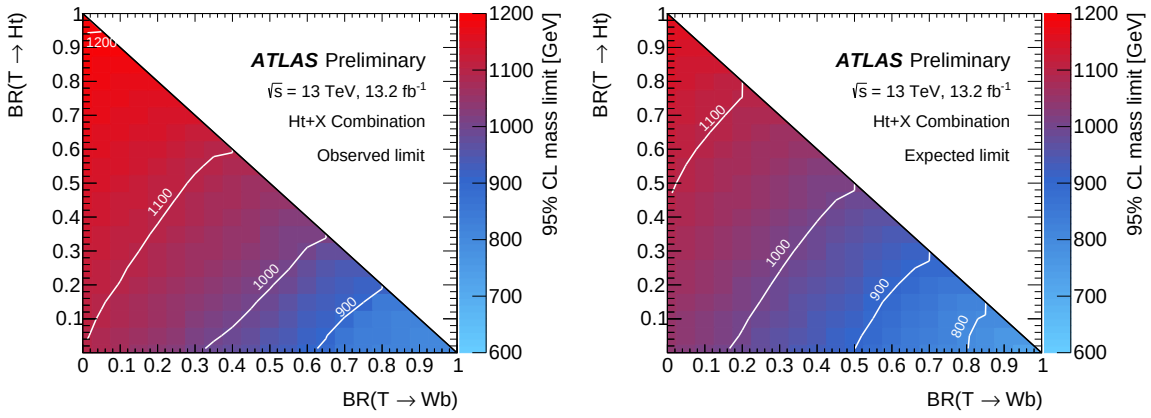

(a) (b)

Figure 19: (a) Observed and (b) expected limit (95% CL) on the mass of the T quark in the plane of BR($T \to Ht$) versus BR($T \to Wb$) for the combination of the 1-lepton and 0-lepton searches. Contour lines are provided to guide the eye.

upper limit on the production cross section can be translated into an observed (expected) limit on the free parameter of the model $|C_{4t}|/\Lambda^2 < 2.9$ TeV^{-2} (3.0 TeV^{-2}).

In the context of the 2UED/RPP model, the observed and expected upper limits on the production cross section times branching ratio are shown in Figure 20 as a function of m_{KK} for the symmetric case ($\xi = R_4/R_5 = 1$), assuming production by tier (1,1) alone. The comparison to the LO theoretical cross section translates into an observed (expected) 95% CL limit on m_{KK} of 1.6 TeV (1.5 TeV).

The current results improve the expected cross section limits obtained by the previous ATLAS analysis based on 3.2 fb^{-1} of data [24] by factors in the range of ~1.6–2.2, depending on the benchmark scenario considered for $t\bar{t}t\bar{t}$ production.

10.4. Limits on associated heavy Higgs boson production

Using the 1-lepton search, 95% CL upper limits on the associated heavy Higgs boson production cross sections times branching ratios are derived for the three signal processes studied, $b\bar{b}H(\to t\bar{t})$, $t\bar{t}H(\to t\bar{t})$, and $tbH^{\pm}(\to tb)$, considering only one signal at a time. As mentioned before, the upper limits on $b\bar{b}H(\to t\bar{t})$ and $t\bar{t}H(\to t\bar{t})$ production can be applied to $b\bar{b}A(\to t\bar{t})$ and $t\bar{t}A(\to t\bar{t})$ production respectively, since there are no significant differences in the kinematic distributions at the reconstructed level. The limits are derived under the assumption that only a single signal process at a time contributes in the signal regions, which makes these limits conservative. Stronger limits would be obtained if simultaneous contributions from four mass-degenerate states (H, A, and $H^{\pm}$) had been considered.

Figure 21 shows the observed and expected upper limits on $\sigma(pp \to b\bar{b}H) \times \mathrm{BR}(H \to t\bar{t})$ as a function of the heavy Higgs boson mass m_H, and they are compared to benchmark theoretical predictions within a Type-I and Type-II 2HDM. In both cases, the obtained limits are more than one order of magnitude above the largest predictions in the alignment limit ($\cos(\beta - \alpha) = 0$), which correspond to tan β values of about 0.1 and 5 respectively. The limited sensitivity of this search is due to the small signal acceptance, since often at least one of the associated b-quarks is not reconstructed and/or b-tagged.

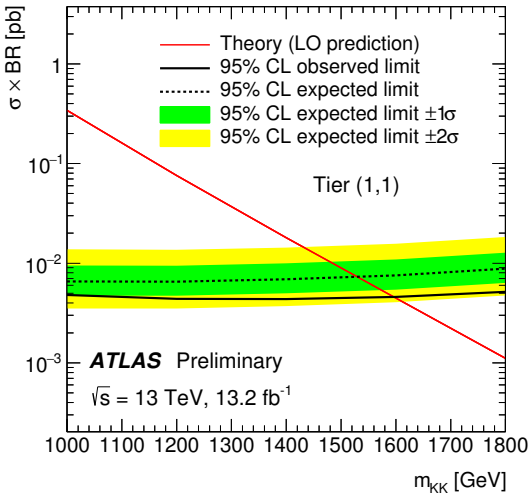

Figure 20: Observed (solid line) and expected (dashed line) 95% CL upper limits on the production cross section times branching ratio of four-top-quark events as a function of the Kaluza–Klein mass (m_{KK}) from tier (1,1) in the symmetric case ($\xi = R_4/R_5 = 1$). The surrounding shaded bands correspond to ±1 and ±2 standard deviations around the expected limit. The thin red line shows the theoretical prediction, computed at LO in QCD, for the production cross section of four-top-quark events by tier (1,1) assuming $\mathrm{BR}(A^{(1,1)} \to t\bar{t}) = 1$, where the heavy photon $A^{(1,1)}$ is the lightest particle of this tier.

Much better sensitivity is achieved in the $t\bar{t}H(\to t\bar{t})$ search, characterised by a large multiplicity of b-tagged jets and mass-tagged jets. The resulting observed and expected upper limits on $\sigma(pp \to t\bar{t}H) \times \mathrm{BR}(H \to t\bar{t})$ as a function of m_H are shown in Figure 22. The comparison to the predictions for a Type-I or Type-II 2HDM[12] in the alignment limit allows the exclusion at the 95% CL of $\tan\beta$ values below 0.17 (0.11) for $m_H = 400$ GeV (1 TeV). The corresponding expected lower limit is 0.23 (0.15).

Finally, Figure 23 shows the observed and expected upper limits on $\sigma(pp \to \bar{t}bH^+) \times \mathrm{BR}(H^+ \to t\bar{b})$ as a function of the heavy Higgs boson mass m_{H^+}. The larger signal production cross section, compared to the neutral Higgs boson case, allows to set more restrictive limits on $\tan\beta$. In this case the 95% CL observed lower limit on $\tan\beta$ for a Type-II 2HDM is 0.65 (0.15) for $m_H = 200$ GeV (1 TeV). The corresponding expected lower limit is 0.55 (0.25).

[12] The ttH couplings have the same value in a Type-I and a Type-II 2HDM.

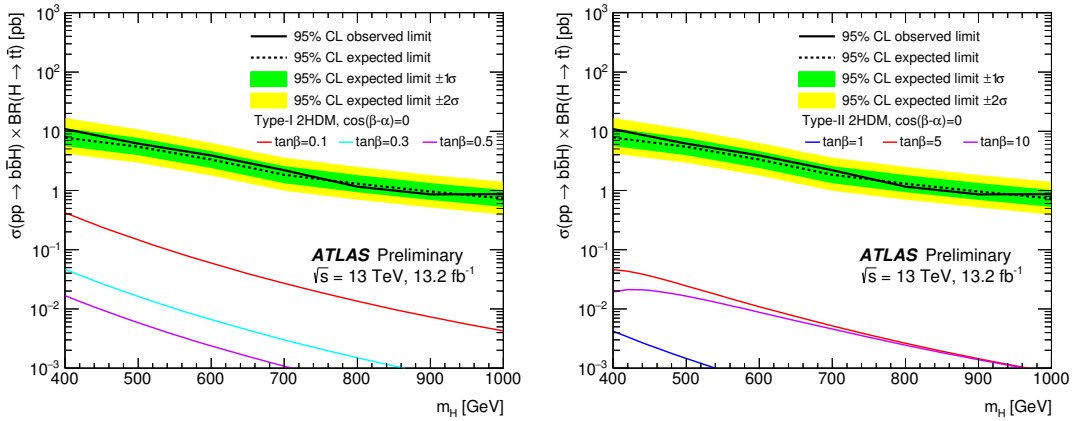

(a) (b)

Figure 21: Observed (solid line) and expected (dashed line) 95% CL upper limits on $\sigma(pp \to b\bar{b}H) \times \mathrm{BR}(H \to t\bar{t})$ as a function of the heavy Higgs boson mass m_H, compared to the theoretical predictions assuming (a) a Type-I 2HDM, and (b) a Type-II 2HDM. The surrounding shaded bands correspond to ±1 and ±2 standard deviations around the expected limit. The coloured thin lines show the theoretical predictions corresponding to different values of tan β, assuming $\cos(\beta - \alpha) = 0$.

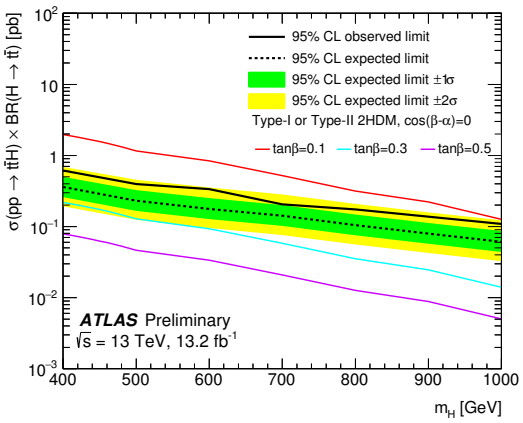

Figure 22: Observed (solid line) and expected (dashed line) 95% CL upper limits on $\sigma(pp \to t\bar{t}H) \times \mathrm{BR}(H \to t\bar{t})$ as a function of the heavy Higgs boson mass m_H, compared to the theoretical predictions assuming a Type-I or Type-II 2HDM. The surrounding shaded bands correspond to ±1 and ±2 standard deviations around the expected limit. The coloured thin lines show the theoretical predictions corresponding to different values of tan β, assuming $\cos(\beta - \alpha) = 0$.

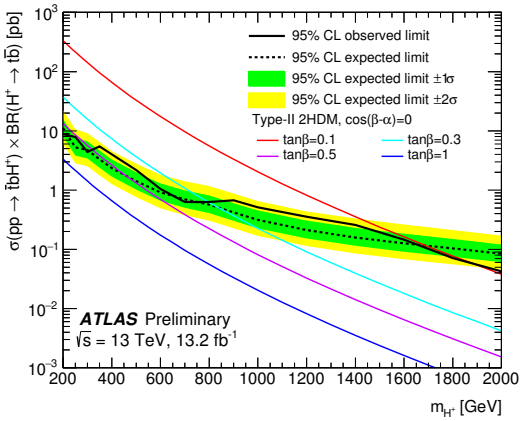

Figure 23: Observed (solid line) and expected (dashed line) 95% CL upper limits on $\sigma(pp \to \bar{t}bH^+) \times \mathrm{BR}(H^+ \to t\bar{b})$ as a function of the heavy Higgs boson mass m_{H^+}, compared to the theoretical predictions assuming a Type-II 2HDM. For the values of tan β displayed, the predictions from a Type-I 2HDM are very close to those from a Type-II 2HDM. The surrounding shaded bands correspond to ± 1 and ± 2 standard deviations around the expected limit. The coloured thin lines show the theoretical predictions corresponding to different values of tan β, assuming $\cos(\beta - \alpha) = 0$.

11. Conclusion

A search for new phenomena in $t\bar{t}$ final states with additional heavy-flavour jets has been presented. The search targets a variety of signals, including the pair production of a vector-like top quark (T) with a significant branching ratio to a top quark and either a Standard Model Higgs boson or a Z boson; four-top-quark production, both within the Standard Model and in several new physics scenarios; and heavy Higgs bosons (neutral and charged) produced in association with, and decaying into, third generation quarks. The analysis uses pp collisions at $\sqrt{s} = 13$ TeV recorded in 2015 and 2016 with the ATLAS detector at the CERN Large Hadron Collider. The dataset corresponds to an integrated luminosity of 13.2 fb^{-1}. Data are analysed in the lepton-plus-jets final state, characterised by an isolated electron or muon with high transverse momentum, large missing transverse momentum and multiple jets, as well as the jets+$E_{\mathrm{T}}^{\mathrm{miss}}$ final state, characterised by multiple jets and large missing transverse momentum. The search exploits the high multiplicity of b-jets, the high scalar sum of transverse momenta of all final state objects, and the presence of boosted, hadronically-decaying resonances reconstructed as large-radius jets characteristic of signal events. In the absence of a significant excess above the Standard Model expectation, 95% CL upper limits are derived for the signal models in a number of benchmark scenarios, in most cases significantly extending the reach of previous searches.

References

[1] ATLAS Collaboration, *Observation of a new particle in the search for the Standard Model Higgs boson with the ATLAS detector at the LHC*, Phys. Lett. B **716** (2012) 1, arXiv: 1207.7214 [hep-ex].

[2] CMS Collaboration, *Observation of a new boson at a mass of 125 GeV with the CMS experiment at the LHC*, Phys. Lett. B **716** (2012) 30, arXiv: 1207.7235 [hep-ex].

[3] L. Susskind, *Dynamics of Spontaneous Symmetry Breaking in the Weinberg-Salam Theory*, Phys. Rev. D **20** (1979) 2619.

[4] P. Fayet, *Spontaneously Broken Supersymmetric Theories of Weak, Electromagnetic and Strong Interactions*, Phys. Lett. B **69** (1977) 489.

[5] A. Djouadi, *The Anatomy of electro-weak symmetry breaking. II. The Higgs bosons in the minimal supersymmetric model*, Phys. Rept. **459** (2008) 1, arXiv: hep-ph/0503173 [hep-ph].

[6] P. Fayet, *Supersymmetry and Weak, Electromagnetic and Strong Interactions*, Phys. Lett. B **64** (1976) 159.

[7] N. Arkani-Hamed et al., *The Littlest Higgs*, JHEP **0207** (2002) 034, arXiv: hep-ph/0206021.

[8] M. Schmaltz and D. Tucker-Smith, *Little Higgs Theories*, Ann. Rev. Nucl. Part. Sci. **55** (2005) 229, arXiv: hep-ph/0502182.

[9] D. B. Kaplan, H. Georgi and S. Dimopoulos, *Composite Higgs Scalars*, Phys. Lett. B **136** (1984) 187.

[10] K. Agashe, R. Contino and A. Pomarol, *The Minimal composite Higgs model*, Nucl. Phys. B **719** (2005) 165, arXiv: hep-ph/0412089.

[11] C. T. Hill and E. H. Simmons, *Strong dynamics and electroweak symmetry breaking*, Phys. Rept. **381** (2003) 235, arXiv: hep-ph/0203079.

[12] F. del Aguila and M. J. Bowick, *The Possibility of New Fermions With $\Delta I = 0$ Mass*, Nucl. Phys. B **224** (1983) 107.

[13] J. A. Aguilar-Saavedra, *Identifying top partners at LHC*, JHEP **0911** (2009) 030, arXiv: 0907.3155 [hep-ph].

[14] J. A. Aguilar-Saavedra, *Mixing with vector-like quarks: constraints and expectations*, EPJ Web Conf. **60** (2013) 16012, arXiv: 1306.4432 [hep-ph].

[15] J. A. Aguilar-Saavedra et al., *Handbook of vectorlike quarks: Mixing and single production*, Phys. Rev. D **88** (2013) 094010, arXiv: 1306.0572 [hep-ph].

[16] A. Atre et al., *Heavy Quarks Above the Top at the Tevatron*, Phys. Rev. D **79** (2009) 054018, arXiv: 0806.3966 [hep-ph].

[17] A. Atre et al., *Model-Independent Searches for New Quarks at the LHC*, JHEP **1108** (2011) 080, arXiv: 1102.1987 [hep-ph].

[18] ATLAS Collaboration, *Search for production of vector-like quark pairs and of four top quarks in the lepton-plus-jets final state in pp collisions at $\sqrt{s} = 8$ TeV with the ATLAS detector*, JHEP **1508** (2015) 105, arXiv: 1505.04306 [hep-ex].

[19] ATLAS Collaboration, *Search for pair and single production of new heavy quarks that decay to a Z boson and a third-generation quark in pp collisions at $\sqrt{s}$ = 8 TeV with the ATLAS detector*, JHEP **1411** (2014) 104, arXiv: 1409.5500 [hep-ex].

[20] ATLAS Collaboration, *Analysis of events with b-jets and a pair of leptons of the same charge in pp collisions at $\sqrt{s}$ = 8 TeV with the ATLAS detector*, JHEP **1510** (2015) 150, arXiv: 1504.04605 [hep-ex].

[21] CMS Collaboration, *Inclusive search for a vector-like T quark with charge $\frac{2}{3}$ in pp collisions at $\sqrt{s}$ = 8 TeV*, Phys. Lett. B **729** (2014) 149, arXiv: 1311.7667 [hep-ex].

[22] CMS Collaboration, *Search for vector-like T quarks decaying to top quarks and Higgs bosons in the all-hadronic channel using jet substructure*, JHEP **1506** (2015) 080, arXiv: 1503.01952 [hep-ex].

[23] CMS Collaboration, *Search for vector-like charge 2/3 T quarks in proton-proton collisions at $\sqrt{s}$ = 8 TeV*, Phys. Rev. D **93** (2016) 012003, arXiv: 1509.04177 [hep-ex].

[24] ATLAS Collaboration, *Search for production of vector-like top quark pairs and of four top quarks in the lepton-plus-jets final state in pp collisions at $\sqrt{s}$ = 13 TeV with the ATLAS detector*, ATLAS-CONF-2016-013 (2016), URL: http://cdsweb.cern.ch/record/2140998.

[25] ATLAS Collaboration, *Search for new physics using events with b-jets and a pair of same charge leptons in 3.2 fb^{-1} of pp collisions at $\sqrt{s}$ = 13 TeV with the ATLAS detector*, ATLAS-CONF-2016-032 (2016), URL: http://cdsweb.cern.ch/record/2161545.

[26] ATLAS Collaboration, *Search for top squarks in final states with one isolated lepton, jets, and missing transverse momentum in $\sqrt{s}$ = 13 TeV pp collisions with the ATLAS detector*, (2016), submitted to Phys. Rev. D, arXiv: 1606.03903 [hep-ex].

[27] CMS Collaboration, *Search for pair production of vector-like T quarks in the lepton plus jets final state*, CMS-PAS-B2G-16-002 (2016), http://cds.cern.ch/record/2141070.

[28] A. Pomarol and J. Serra, *Top Quark Compositeness: Feasibility and Implications*, Phys. Rev. D **78** (2008) 074026, arXiv: 0806.3247 [hep-ph].

[29] B. Lillie, J. Shu and T. M. P. Tait, *Top Compositeness at the Tevatron and LHC*, JHEP **0804** (2008) 087, arXiv: 0712.3057 [hep-ph].

[30] K. Kumar, T. M. P. Tait and R. Vega-Morales, *Manifestations of Top Compositeness at Colliders*, JHEP **0905** (2009) 022, arXiv: 0901.3808 [hep-ph].

[31] G. Cacciapaglia, A. Deandrea and J. Llodra-Perez, *A Dark Matter candidate from Lorentz Invariance in 6D*, JHEP **1003** (2010) 083, arXiv: 0907.4993 [hep-ph].

[32] G. Cacciapaglia et al., *Four tops on the real projective plane at LHC*, JHEP **1110** (2011) 042, arXiv: 1107.4616 [hep-ph].

[33] A. Arbey et al., *Dark Matter in a twisted bottle*, JHEP **1301** (2013) 147, arXiv: 1210.0384 [hep-ph].

[34] CMS Collaboration, *Search for standard model production of four top quarks in the lepton + jets channel in pp collisions at $\sqrt{s}$ = 8 TeV*, JHEP **1411** (2014) 154, arXiv: 1409.7339 [hep-ex].

[35] ATLAS Collaboration,
Search for four-top-quark production in final states with one charged lepton and multiple jets using 3.2 fb^{-1} of proton-proton collisions at $\sqrt{s}$ = 13 TeV with the ATLAS detector at the LHC,
ATLAS-CONF-2016-020 (2016), URL: http://cdsweb.cern.ch/record/2144537.

[36] CMS Collaboration,
Search for standard model production of four top quarks in proton-proton collisions at 13 TeV,
CMS-PAS-TOP-16-016 (2016), URL: http://cdsweb.cern.ch/record/2205265.

[37] G. C. Branco et al., *Theory and phenomenology of two-Higgs-doublet models*,
Phys. Rept. **516** (2012) 1, arXiv: 1106.0034 [hep-ph].

[38] ATLAS Collaboration, *Search for a CP-odd Higgs boson decaying to Zh in pp collisions at $\sqrt{s}$ = 13 TeV with the ATLAS detector*, ATLAS-CONF-2016-015 (2016),
URL: https://cds.cern.ch/record/2141003.

[39] ATLAS Collaboration, *Search for ZZ resonances in the $\ell\ell qq$ final state in pp collisions at $\sqrt{s}$ = 13 TeV with the ATLAS detector*, ATLAS-CONF-2016-016 (2016),
URL: https://cds.cern.ch/record/2141005.

[40] ATLAS Collaboration, *Search for new phenomena in the $Z(\rightarrow \ell^+\ell^-)+E_T^{miss}$ final state at $\sqrt{s}$ = 13 TeV with the ATLAS detector*, ATLAS-CONF-2016-056 (2016),
URL: https://cds.cern.ch/record/2206138.

[41] ATLAS Collaboration, *Search for a high-mass Higgs boson decaying to a pair of W bosons in pp collisions at $\sqrt{s}$ = 13 TeV with the ATLAS detector*, ATLAS-CONF-2016-074 (2016),
URL: https://cds.cern.ch/record/2206243.

[42] ATLAS Collaboration, *Search for Minimal Supersymmetric Standard Model Higgs Bosons H/A in the $\tau\tau$ final state in up to 13.3 fb^{-1} of pp collisions at $\sqrt{s}$ = 13 TeV with the ATLAS Detector*,
ATLAS-CONF-2016-085 (2016), URL: https://cds.cern.ch/record/2206278.

[43] ATLAS Collaboration, *Search for charged Higgs bosons in the τ+jets final state using 14.7 fb^{-1} of pp collision data recorded at $\sqrt{s}$ = 13 TeV with the ATLAS experiment*,
ATLAS-CONF-2016-088 (2016), URL: https://cds.cern.ch/record/2206282.

[44] ATLAS Collaboration, *Search for charged Higgs bosons in the $H^{\pm} \rightarrow tb$ decay channel in pp collisions at $\sqrt{s}$ = 13 TeV using the ATLAS detector*, ATLAS-CONF-2016-089 (2016),
URL: http://cdsweb.cern.ch/record/2206809.

[45] CMS Collaboration,
Search for a heavy scalar boson decaying into a pair of Z bosons in the $2\ell 2\nu$ final state,
CMS-PAS-HIG-16-001 (2016), URL: https://cds.cern.ch/record/2140099.

[46] CMS Collaboration, *Search for a neutral MSSM Higgs boson decaying into $\tau\tau$ at 13 TeV*,
CMS-PAS-HIG-16-006 (2016), URL: https://cds.cern.ch/record/2160252.

[47] CMS Collaboration, *Search for H to $Z(\ell\ell)$ + $A(bb)$ with 2015 data*,
CMS-PAS-HIG-16-010 (2016), URL: https://cds.cern.ch/record/2140613.

[48] CMS Collaboration,
Search for high mass Higgs to WW with fully leptonic decays using 2015 data,
CMS-PAS-HIG-16-023 (2016), URL: https://cds.cern.ch/record/2205151.

[49] CMS Collaboration, *Search for charged Higgs bosons in WZ decays at 13 TeV*,
CMS-PAS-HIG-16-027 (2016), URL: https://cds.cern.ch/record/2204919.

[50] ATLAS Collaboration, *Constraints on new phenomena via Higgs boson couplings and invisible decays with the ATLAS detector*, JHEP **1511** (2015) 206, arXiv: 1509.00672 [hep-ex].

[51] CMS Collaboration, *Summary results of high mass BSM Higgs searches using CMS run-I data*, CMS-PAS-HIG-16-007 (2016), URL: https://cds.cern.ch/record/2142432.

[52] G. C. Dorsch et al., *Hierarchical versus degenerate 2HDM: The LHC run 1 legacy at the onset of run 2*, Phys. Rev. D **93** (2016) 115033, arXiv: 1601.04545 [hep-ph].

[53] R. Frederix and F. Maltoni, *Top pair invariant mass distribution: A Window on new physics*, JHEP **0901** (2009) 047, arXiv: 0712.2355 [hep-ph].

[54] ATLAS Collaboration, *Search for heavy Higgs bosons A/H decaying to a top-quark pair in pp collisions at $\sqrt{s} = 8$ TeV with the ATLAS detector*, ATLAS-CONF-2016-073 (2016), URL: http://cdsweb.cern.ch/record/2206229.

[55] ATLAS Collaboration, *Search for charged Higgs bosons in the $H^{\pm} \to tb$ decay channel in pp collisions at $\sqrt{s} = 8$ TeV using the ATLAS detector*, JHEP **1603** (2016) 127, arXiv: 1512.03704 [hep-ex].

[56] CMS Collaboration, *Search for a charged Higgs boson in pp collisions at $\sqrt{s} = 8$ TeV*, JHEP **1511** (2015) 018, arXiv: 1508.07774 [hep-ex].

[57] N. Craig et al., *The Hunt for the Rest of the Higgs Bosons*, JHEP **1506** (2015) 137, arXiv: 1504.04630 [hep-ph].

[58] J. Hajer et al., *Heavy Higgs Bosons at 14 TeV and 100 TeV*, JHEP **1511** (2015) 124, arXiv: 1504.07617 [hep-ph].

[59] S. Gori et al., *Closing the Wedge: Search Strategies for Extended Higgs Sectors with Heavy Flavor Final States*, Phys. Rev. D **93** (2016) 075038, arXiv: 1602.02782 [hep-ph].

[60] N. Craig et al., *Heavy Higgs Bosons at Low* $\tan\beta$*: from the LHC to 100 TeV*, (2016), arXiv: 1605.08744 [hep-ph].

[61] ATLAS Collaboration, *The ATLAS Experiment at the CERN Large Hadron Collider*, JINST **3** (2008) S08003.

[62] ATLAS Collaboration, *ATLAS Insertable B-Layer Technical Design Report*, ATLAS-TDR-19 (2010), https://cds.cern.ch/record/1291633.

[63] ATLAS Collaboration, *2015 start-up trigger menu and initial performance assessment of the ATLAS trigger using Run-2 data*, ATL-DAQ-PUB-2016-001 (2016), https://cds.cern.ch/record/2136007.

[64] ATLAS Collaboration, *Vertex reconstruction performance of the ATLAS detector at $\sqrt{s} = 13$ TeV*, ATL-PHYS-PUB-2015-026 (2015), http://cds.cern.ch/record/2037717.

[65] ATLAS Collaboration, *Electron reconstruction and identification efficiency measurements with the ATLAS detector using the 2011 LHC proton-proton collision data*, Eur. Phys. J. C **74** (2014) 2941, arXiv: 1404.2240 [hep-ex].

[66] ATLAS Collaboration, *Electron and photon energy calibration with the ATLAS detector using LHC Run 1 data*, Eur. Phys. J. C **74** (2014) 3071, arXiv: 1407.5063 [hep-ex].

[67] ATLAS Collaboration, *Electron efficiency measurements with the ATLAS detector using the 2015 LHC proton-proton collision data*, ATLAS-CONF-2016-024 (2016), http://cds.cern.ch/record/2157687.

[68] ATLAS Collaboration, *Muon reconstruction performance of the ATLAS detector in proton-proton collision data at $\sqrt{s}$ =13 TeV*, Eur. Phys. J. C **76** (2016) 292, arXiv: 1603.05598 [hep-ex].

[69] M. Cacciari, G. P. Salam and G. Soyez, *The anti-k_t jet clustering algorithm*, JHEP **0804** (2008) 063, arXiv: 0802.1189 [hep-ph].

[70] M. Cacciari and G. P. Salam, *Dispelling the N^3 myth for the k_t jet-finder*, Phys. Lett. B **641** (2006) 57, arXiv: hep-ph/0512210 [hep-ph].

[71] M. Cacciari, G. P. Salam and G. Soyez, *FastJet User Manual*, Eur. Phys. J. C **72** (2012) 1896, arXiv: 1111.6097 [hep-ph].

[72] C. Cojocaru et al., *Hadronic calibration of the ATLAS liquid argon end-cap calorimeter in the pseudorapidity region 1.6 < $|\eta|$ < 1.8 in beam tests*, Nucl. Instrum. Meth. A **531** (2004) 481, arXiv: physics/0407009 [physics].

[73] ATLAS Collaboration, *Topological cell clustering in the ATLAS calorimeters and its performance in LHC Run 1*, (2016), submitted to Eur. Phys. J. C, arXiv: 1603.02934 [hep-ex].

[74] ATLAS Collaboration, *Jet calibration and systematic uncertainties for jets reconstructed in the ATLAS detector at $\sqrt{s}$ = 13 TeV*, ATLAS-PHYS-PUB-2015-015 (2015), http://cds.cern.ch/record/2037613.

[75] ATLAS Collaboration, *Monte Carlo Calibration and Combination of In-Situ Measurements of Jet Energy Scale, Jet Energy Resolution and Jet Mass in ATLAS*, ATLAS-CONF-2015-037 (2015), http://cds.cern.ch/record/2044941.

[76] ATLAS Collaboration, *Selection of jets produced in 13 TeV proton-proton collisions with the ATLAS detector*, ATLAS-CONF-2015-029 (2015), http://cds.cern.ch/record/2037702.

[77] ATLAS Collaboration, *Performance of pile-up mitigation techniques for jets in pp collisions at $\sqrt{s}$ = 8 TeV using the ATLAS detector*, (2015), submitted to Eur. Phys. J. C, arXiv: 1510.03823 [hep-ex].

[78] ATLAS Collaboration, *Performance of b-Jet Identification in the ATLAS Experiment*, JINST **11** (2016) P04008, arXiv: 1512.01094 [hep-ex].

[79] ATLAS Collaboration, *Optimisation of the ATLAS b-tagging performance for the 2016 LHC Run*, ATL-PHYS-PUB-2016-012 (2016), http://cds.cern.ch/record/2160731.

[80] B. Nachman et al., *Jets from Jets: Re-clustering as a tool for large radius jet reconstruction and grooming at the LHC*, JHEP **1502** (2015) 075, arXiv: 1407.2922 [hep-ph].

[81] D. Krohn, J. Thaler and L.-T. Wang, *Jet Trimming*, JHEP **1002** (2010) 084, arXiv: 0912.1342 [hep-ph].

[82] ATLAS Collaboration, *Performance of Missing Transverse Momentum Reconstruction in Proton-Proton Collisions at 7 TeV with ATLAS*, Eur. Phys. J. C **72** (2012) 1844, arXiv: 1108.5602 [hep-ex].

[83] ATLAS Collaboration, *Performance of missing transverse momentum reconstruction for the ATLAS detector in the first proton-proton collisions at* $\sqrt{s} = 13$ *TeV*, ATLAS-CONF-2013-082 (2013), http://cds.cern.ch/record/1570993.

[84] J. A. Aguilar-Saavedra, *PROTOS, a PROgram for TOp Simulations*, http://jaguilar.web.cern.ch/jaguilar/protos/.

[85] R. D. Ball et al., *Parton distributions with LHC data*, Nucl. Phys. B **867** (2013) 244, arXiv: 1207.1303 [hep-ph].

[86] T. Sjöstrand, S. Mrenna and P. Z. Skands, *A Brief Introduction to PYTHIA 8.1*, Comput. Phys. Commun. **178** (2008) 852, arXiv: 0710.3820 [hep-ph].

[87] ATLAS Collaboration, *ATLAS Pythia 8 tunes to 7 TeV data*, ATL-PHYS-PUB-2014-021 (2014), https://cds.cern.ch/record/1966419.

[88] M. Czakon and A. Mitov, *Top++: A Program for the Calculation of the Top-Pair Cross-Section at Hadron Colliders*, Comput. Phys. Commun. **185** (2014) 2930, arXiv: 1112.5675 [hep-ph].

[89] M. Cacciari et al., *Top-pair production at hadron colliders with next-to-next-to-leading logarithmic soft-gluon resummation*, Phys. Lett. B **710** (2012) 612, arXiv: 1111.5869 [hep-ph].

[90] P. Bärnreuther, M. Czakon and A. Mitov, *Percent-Level-Precision Physics at the Tevatron: Next-to-Next-to-Leading Order QCD Corrections to* $q\bar{q} \to t\bar{t} + X$, Phys. Rev. Lett. **109** (2012) 132001, arXiv: 1204.5201 [hep-ph].

[91] M. Czakon and A. Mitov, *NNLO corrections to top-pair production at hadron colliders: the all-fermionic scattering channels*, JHEP **1212** (2012) 054, arXiv: 1207.0236 [hep-ph].

[92] M. Czakon and A. Mitov, *NNLO corrections to top pair production at hadron colliders: the quark-gluon reaction*, JHEP **1301** (2013) 080, arXiv: 1210.6832 [hep-ph].

[93] M. Czakon, P. Fiedler and A. Mitov, *Total Top-Quark Pair-Production Cross Section at Hadron Colliders Through* $O(\alpha_S^4)$, Phys. Rev. Lett. **110** (2013) 252004, arXiv: 1303.6254 [hep-ph].

[94] A. D. Martin et al., *Parton distributions for the LHC*, Eur. Phys. J. C **63** (2009) 189, arXiv: 0901.0002 [hep-ph].

[95] A. D. Martin et al., *Uncertainties on* α_S *in global PDF analyses and implications for predicted hadronic cross sections*, Eur. Phys. J. C **64** (2009) 653, arXiv: 0905.3531 [hep-ph].

[96] C. Degrande et al., *Non-resonant New Physics in Top Pair Production at Hadron Colliders*, JHEP **1103** (2011) 125, arXiv: 1010.6304 [hep-ph].

[97] J. Alwall et al., *The automated computation of tree-level and next-to-leading order differential cross sections, and their matching to parton shower simulations*, JHEP **1407** (2014) 079, arXiv: 1405.0301 [hep-ph].

[98] P. Meade and M. Reece, *BRIDGE: Branching ratio inquiry / decay generated events*, (2007), arXiv: hep-ph/0703031.

[99] G. R. Farrar and P. Fayet, *Phenomenology of the Production, Decay, and Detection of New Hadronic States Associated with Supersymmetry*, Phys. Lett. B **76** (1978) 575.

[100] P. Fayet, *Relations Between the Masses of the Superpartners of Leptons and Quarks, the Goldstino Couplings and the Neutral Currents*, Phys. Lett. B **84** (1979) 416.

[101] S. Dimopoulos and H. Georgi, *Softly Broken Supersymmetry and SU(5)*, Nucl. Phys. B **193** (1981) 150.

[102] T. Sjöstrand, S. Mrenna and P. Z. Skands, *PYTHIA 6.4 Physics and Manual*, JHEP **0605** (2006) 026, arXiv: hep-ph/0603175.

[103] J. Pumplin et al., *New generation of parton distributions with uncertainties from global QCD analysis*, JHEP **0207** (2002) 012, arXiv: hep-ph/0201195 [hep-ph].

[104] R. V. Harlander, S. Liebler and H. Mantler, *SusHi: A program for the calculation of Higgs production in gluon fusion and bottom-quark annihilation in the Standard Model and the MSSM*, Comput. Phys. Commun. **184** (2013) 1605, arXiv: 1212.3249 [hep-ph].

[105] R. V. Harlander and W. B. Kilgore, *Next-to-next-to-leading order Higgs production at hadron colliders*, Phys. Rev. Lett. **88** (2002) 201801, arXiv: hep-ph/0201206 [hep-ph].

[106] R. V. Harlander and W. B. Kilgore, *Higgs boson production in bottom quark fusion at next-to-next-to leading order*, Phys. Rev. D **68** (2003) 013001, arXiv: hep-ph/0304035 [hep-ph].

[107] U. Aglietti et al., *Two loop light fermion contribution to Higgs production and decays*, Phys. Lett. B **595** (2004) 432, arXiv: hep-ph/0404071 [hep-ph].

[108] R. Bonciani, G. Degrassi and A. Vicini, *On the Generalized Harmonic Polylogarithms of One Complex Variable*, Comput. Phys. Commun. **182** (2011) 1253, arXiv: 1007.1891 [hep-ph].

[109] R. Harlander and P. Kant, *Higgs production and decay: Analytic results at next-to-leading order QCD*, JHEP **0512** (2005) 015, arXiv: hep-ph/0509189 [hep-ph].

[110] D. Eriksson, J. Rathsman and O. Stal, *2HDMC: Two-Higgs-Doublet Model Calculator Physics and Manual*, Comput. Phys. Commun. **181** (2010) 189, arXiv: 0902.0851 [hep-ph].

[111] R. Harlander, M. Kramer and M. Schumacher, *Bottom-quark associated Higgs-boson production: reconciling the four- and five-flavour scheme approach*, (2011), arXiv: 1112.3478 [hep-ph].

[112] C. Degrande et al., *Heavy charged Higgs boson production at the LHC*, JHEP **1510** (2015) 145, arXiv: 1507.02549 [hep-ph].

[113] M. Flechl et al., *Improved cross-section predictions for heavy charged Higgs boson production at the LHC*, Phys. Rev. D **91** (2015) 075015, arXiv: 1409.5615 [hep-ph].

[114] LHC Higgs Cross Section Working Group, J.R. Andersen et al., *Handbook of LHC Higgs Cross Sections: 3. Higgs Properties*, (2013), arXiv: 1307.1347 [hep-ph].

[115] E. L. Berger et al., *Associated production of a top quark and a charged Higgs boson*, Phys. Rev. D **71** (2005) 115012, arXiv: hep-ph/0312286 [hep-ph].

[116] D. J. Lange, *The EvtGen particle decay simulation package*, Nucl. Instrum. Meth. A **462** (2001) 152.

[117] A. Sherstnev and R. S. Thorne, *Parton Distributions for LO Generators*, Eur. Phys. J. C **55** (2008) 553, arXiv: 0711.2473 [hep-ph].

[118] ATLAS Collaboration, *Further ATLAS tunes of Pythia 6 and Pythia 8*, ATL-PHYS-PUB-2011-014 (2011), https://cds.cern.ch/record/1400677.

[119] ATLAS Collaboration, *The ATLAS Simulation Infrastructure*, Eur. Phys. J. C **70** (2010) 823, arXiv: 1005.4568 [physics.ins-det].

[120] GEANT4 Collaboration, S. Agostinelli et al., *GEANT4: A Simulation toolkit*, Nucl. Instrum. Meth. A **506** (2003) 250.

[121] S. Frixione, P. Nason and G. Ridolfi, *A Positive-weight next-to-leading-order Monte Carlo for heavy flavour hadroproduction*, JHEP **0709** (2007) 126, arXiv: 0707.3088 [hep-ph].

[122] P. Nason, *A New method for combining NLO QCD with shower Monte Carlo algorithms*, JHEP **0411** (2004) 040, arXiv: hep-ph/0409146.

[123] S. Frixione, P. Nason and C. Oleari, *Matching NLO QCD computations with Parton Shower simulations: the POWHEG method*, JHEP **0711** (2007) 070, arXiv: 0709.2092 [hep-ph].

[124] S. Alioli et al., *A general framework for implementing NLO calculations in shower Monte Carlo programs: the POWHEG BOX*, JHEP **1006** (2010) 043, arXiv: 1002.2581 [hep-ph].

[125] H.-L. Lai et al., *New parton distributions for collider physics*, Phys. Rev. D **82** (2010) 074024, arXiv: 1007.2241 [hep-ph].

[126] ATLAS Collaboration, *Comparison of Monte Carlo generator predictions to ATLAS measurements of top pair production at* $\sqrt{s} = 7$ *TeV*, ATL-PHYS-PUB-2015-002 (2015), https://cds.cern.ch/record/1981319.

[127] P. Z. Skands, *Tuning Monte Carlo Generators: The Perugia Tunes*, Phys. Rev. D **82** (2010) 074018, arXiv: 1005.3457 [hep-ph].

[128] M. Bahr et al., *Herwig++ Physics and Manual*, Eur. Phys. J. C **58** (2008) 639, arXiv: 0803.0883 [hep-ph].

[129] ATLAS Collaboration, *Simulation of top quark production for the ATLAS experiment at* $\sqrt{s} = 13$ *TeV*, ATL-PHYS-PUB-2016-004 (2016), https://cds.cern.ch/record/2120417.

[130] ATLAS Collaboration, *Search for the Standard Model Higgs boson produced in association with top quarks and decaying into* $b\bar{b}$ *in pp collisions at* $\sqrt{s} = 8$ *TeV with the ATLAS detector*, Eur. Phys. J. C **75** (2015) 349, arXiv: 1503.05066 [hep-ex].

[131] ATLAS Collaboration, *Search for the Standard Model Higgs boson produced in association with top quarks and decaying into* $b\bar{b}$ *in pp collisions at* $\sqrt{s} = 13$ *TeV with the ATLAS detector*, ATLAS-CONF-2016-080 (2016), URL: http://cdsweb.cern.ch/record/2206255.

[132] M. Czakon, D. Heymes and A. Mitov, *High-precision differential predictions for top-quark pairs at the LHC*, Phys. Rev. Lett. **116** (2016) 082003, arXiv: 1511.00549 [hep-ph].

[133] M. Czakon, D. Heymes and A. Mitov,
Dynamical scales for multi-TeV top-pair production at the LHC, (2016),
arXiv: 1606.03350 [hep-ph].

[134] ATLAS Collaboration, *Measurements of top-quark pair differential cross-sections in the lepton+jets channel in pp collisions at $\sqrt{s}$ = 8 TeV using the ATLAS detector*,
(2015), submitted to Eur. Phys. J. C, arXiv: 1511.04716 [hep-ex].

[135] F. Cascioli et al., *NLO matching for $t\bar{t}b\bar{b}$ production with massive b-quarks*,
Phys. Lett. B **734** (2014) 210, arXiv: 1309.5912 [hep-ph].

[136] T. Gleisberg et al., *Event generation with SHERPA 1.1*, JHEP **0902** (2009) 007,
arXiv: 0811.4622 [hep-ph].

[137] F. Cascioli, P. Maierhofer and S. Pozzorini, *Scattering Amplitudes with Open Loops*,
Phys. Rev. Lett. **108** (2012) 111601, arXiv: 1111.5206 [hep-ph].

[138] R. Frederix, E. Re and P. Torrielli, *Single-top t-channel hadroproduction in the four-flavour scheme with POWHEG and aMC@NLO*, JHEP **1209** (2012) 130, arXiv: 1207.5391 [hep-ph].

[139] S. Frixione et al., *Single-Top Production in MC@NLO*, JHEP **0603** (2006) 092,
arXiv: hep-ph/0512250.

[140] N. Kidonakis, *Next-to-next-to-leading-order collinear and soft gluon corrections for t-channel single top quark production*, Phys. Rev. D **83** (2011) 091503, arXiv: 1103.2792 [hep-ph].

[141] N. Kidonakis, *Two-loop soft anomalous dimensions for single top quark associated production with a W^- or H^-*, Phys. Rev. D **82** (2010) 054018, arXiv: 1005.4451 [hep-ph].

[142] N. Kidonakis, *NNLL resummation for s-channel single top quark production*,
Phys. Rev. D **81** (2010) 054028, arXiv: 1001.5034 [hep-ph].

[143] T. Gleisberg and S. Höche, *Comix, a new matrix element generator*, JHEP **0812** (2008) 039,
arXiv: 0808.3674 [hep-ph].

[144] S. Schumann and F. Krauss,
A Parton shower algorithm based on Catani-Seymour dipole factorisation,
JHEP **0803** (2008) 038, arXiv: 0709.1027 [hep-ph].

[145] S. Höche et al., *QCD matrix elements + parton showers: The NLO case*, JHEP **1304** (2013) 027,
arXiv: 1207.5030 [hep-ph].

[146] C. Anastasiou et al., *High precision QCD at hadron colliders: Electroweak gauge boson rapidity distributions at NNLO*, Phys. Rev. D **69** (2004) 094008, arXiv: hep-ph/0312266 [hep-ph].

[147] R. D. Ball et al., *Parton distributions for the LHC Run II*, JHEP **1504** (2015) 040,
arXiv: 1410.8849 [hep-ph].

[148] R. Raitio and W. W. Wada, *Higgs Boson Production at Large Transverse Momentum in QCD*,
Phys. Rev. D **19** (1979) 941.

[149] W. Beenakker et al., *NLO QCD corrections to $t\bar{t}H$ production in hadron collisions*,
Nucl. Phys. B **653** (2003) 151, arXiv: hep-ph/0211352 [hep-ph].

[150] S. Dawson et al., *Associated Higgs production with top quarks at the large hadron collider: NLO QCD corrections*, Phys. Rev. D **68** (2003) 034022, arXiv: hep-ph/0305087 [hep-ph].

[151] Y. Zhang et al.,
QCD NLO and EW NLO corrections to $t\bar{t}H$ production with top quark decays at hadron collider,
Phys. Lett. B **738** (2014) 1, arXiv: 1407.1110 [hep-ph].

[152] S. Frixione et al.,
Electroweak and QCD corrections to top-pair hadroproduction in association with heavy bosons,
JHEP **1506** (2015) 184, arXiv: 1504.03446 [hep-ph].

[153] A. Djouadi, J. Kalinowski and M. Spira, *HDECAY: A Program for Higgs boson decays in the standard model and its supersymmetric extension*, Comput. Phys. Commun. **108** (1998) 56,
arXiv: hep-ph/9704448 [hep-ph].

[154] ATLAS Collaboration, *Measurement of the top quark-pair production cross section with ATLAS in pp collisions at* $\sqrt{s}$ = 7 *TeV*, Eur. Phys. J. C **71** (2011) 1577, arXiv: 1012.1792 [hep-ex].

[155] ATLAS Collaboration, *Improved luminosity determination in pp collisions at* $\sqrt{s}$ = 7 *TeV using the ATLAS detector at the LHC*, Eur. Phys. J. C **73** (2013) 2518, arXiv: 1302.4393 [hep-ex].

[156] ATLAS Collaboration, *Electron performance measurements with the ATLAS detector using the 2010 LHC proton-proton collision data*, Eur. Phys. J. C **72** (2012) 1909,
arXiv: 1110.3174 [hep-ex].

[157] ATLAS Collaboration, *Measurement of the muon reconstruction performance of the ATLAS detector using 2011 and 2012 LHC proton-proton collision data*, Eur. Phys. J. C **74** (2014) 3130,
arXiv: 1407.3935 [hep-ex].

[158] ATLAS Collaboration, *Measurements of fiducial cross-sections for* $t\bar{t}$ *production with one or two additional b-jets in pp collisions at* $\sqrt{s}$ = 8 *TeV using the ATLAS detector*,
Eur. Phys. J. C **76** (2016) 11, arXiv: 1508.06868 [hep-ex].

[159] CMS Collaboration, *Measurement of* $\mathrm{t\bar{t}}$ *production with additional jet activity, including* b *quark jets, in the dilepton decay channel using pp collisions at* $\sqrt{s}$ = 8 *TeV*,
Eur. Phys. J. C **76** (2016) 379, arXiv: 1510.03072 [hep-ex].

[160] S. Frixione et al., *Single-top hadroproduction in association with a W boson*,
JHEP **0807** (2008) 029, arXiv: 0805.3067 [hep-ph].

[161] J. M. Campbell and R. K. Ellis, *An Update on vector boson pair production at hadron colliders*,
Phys. Rev. D **60** (1999) 113006, arXiv: hep-ph/9905386.

[162] J. Alwall et al., *Comparative study of various algorithms for the merging of parton showers and matrix elements in hadronic collisions*, Eur. Phys. J. C **53** (2008) 473,
arXiv: 0706.2569 [hep-ph].

[163] J. M. Campbell and R. K. Ellis, $t\bar{t}W^{\pm}$ *production and decay at NLO*, JHEP **1207** (2012) 052,
arXiv: 1204.5678 [hep-ph].

[164] M. V. Garzelli et al., $t\bar{t}W^{\pm}$ *and* $t\bar{t}Z$ *Hadroproduction at NLO accuracy in QCD with Parton Shower and Hadronization effects*, JHEP **1211** (2012) 056, arXiv: 1208.2665 [hep-ph].

[165] LHC Higgs Cross Section Working Group, S. Dittmaier et al.,
Handbook of LHC Higgs Cross Sections: 1. Inclusive Observables, (2011),
arXiv: 1101.0593 [hep-ph].

[166] W. Verkerke and D. P. Kirkby, *The RooFit toolkit for data modeling*,
eConf **C0303241** (2003) MOLT007, arXiv: physics/0306116 [physics.data-an].

[167] W. Verkerke and D. Kirkby, *RooFit Users Manual*, http://roofit.sourceforge.net/.

[168] G. Cowan et al., *Asymptotic formulae for likelihood-based tests of new physics*,
Eur. Phys. J. C **71** (2011) 1554, arXiv: 1007.1727 [physics.data-an].

[169] G. Cowan et al., *Erratum to: Asymptotic formulae for likelihood-based tests of new physics*, Eur. Phys. J. C **73** (2013).

[170] T. Junk, *Confidence level computation for combining searches with small statistics*, Nucl. Instrum. Meth. A **434** (1999) 435, arXiv: hep-ex/9902006.

[171] A. L. Read, *Presentation of search results: The CL_S technique*, J. Phys. G **28** (2002) 2693.

Appendix

A. Pre- and post-fit kinematic variables

Figures 24–29 show the comparison between data and prediction, before and after performing the combined fit to data in the 0-lepton and 1-lepton channels, for a number of relevant kinematic variables used to define the analysis strategy.

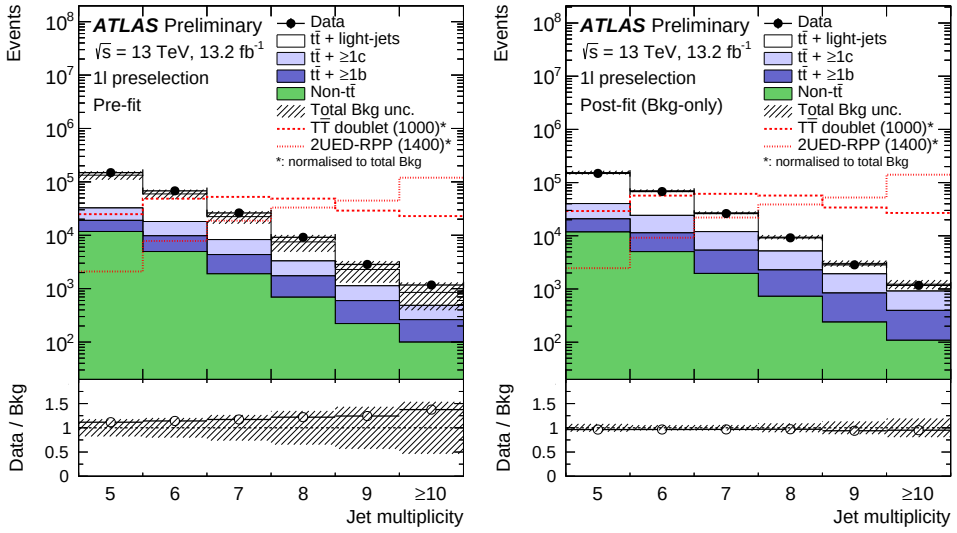

(a) (b)

Figure 24: Comparison between the data and prediction for the jet multiplicity distribution in the 1-lepton channel after preselection, (a) before and (b) after performing the combined fit to data in the 0-lepton and 1-lepton channels ("Pre-fit" and "Post-fit", respectively) under the background-only hypothesis. The small contributions from $t\bar{t}V$, $t\bar{t}H$, single top, W/Z+jets, diboson, and multijet backgrounds are combined into a single background source referred to as "Non-$t\bar{t}$". The expected signal distributions are shown, normalised to the total background prediction, for two scenarios considered in this search: $T\bar{T}$ production in the weak-isospin doublet scenario assuming $m_T = 1000$ GeV (red dashed histogram), and $t\bar{t}t\bar{t}$+X within the 2UED/RPP model assuming $m_{KK} = 1400$ GeV (red dotted histogram). The last bin in all figures contains the overflow. The bottom panels display the ratios of data to the total background prediction ("Bkg"). The hashed area represents the total uncertainty on the background. In the case of the pre-fit background uncertainty, the normalisation uncertainty on the $t\bar{t}+\geq 1b$ background is not included.

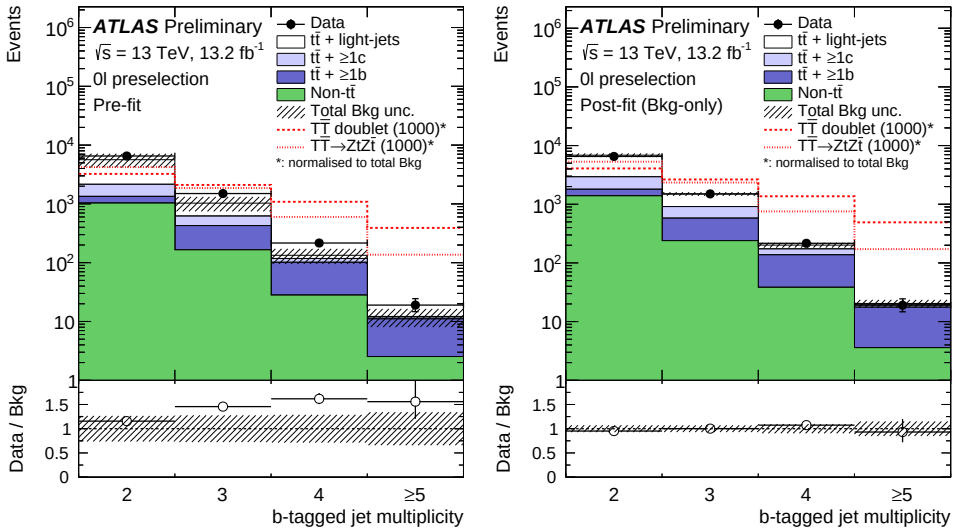

(a) (b)

Figure 25: Comparison between the data and prediction for the b-tag multiplicity distribution in the 0-lepton channel after preselection, (a) before and (b) after performing the combined fit to data in the 0-lepton and 1-lepton channels ("Pre-fit" and "Post-fit", respectively) under the background-only hypothesis. The small contributions from $t\bar{t}V$, $t\bar{t}H$, single top, W/Z+jets, diboson, and multijet backgrounds are combined into a single background source referred to as "Non-$t\bar{t}$". The expected signal distributions are shown, normalised to the total background prediction, for two scenarios considered in this search: $T\bar{T}$ production in the weak-isospin doublet scenario (red dashed histogram), and for BR($T \to Zt$) = 1 (red dotted histogram), both assuming m_T = 1000 GeV. The last bin in all figures contains the overflow. The bottom panels display the ratios of data to the total background prediction ("Bkg"). The blue triangles indicate points that are outside the vertical range of the figure. The hashed area represents the total uncertainty on the background. In the case of the pre-fit background uncertainty, the normalisation uncertainty on the $t\bar{t}+ \geq 1b$ background is not included.

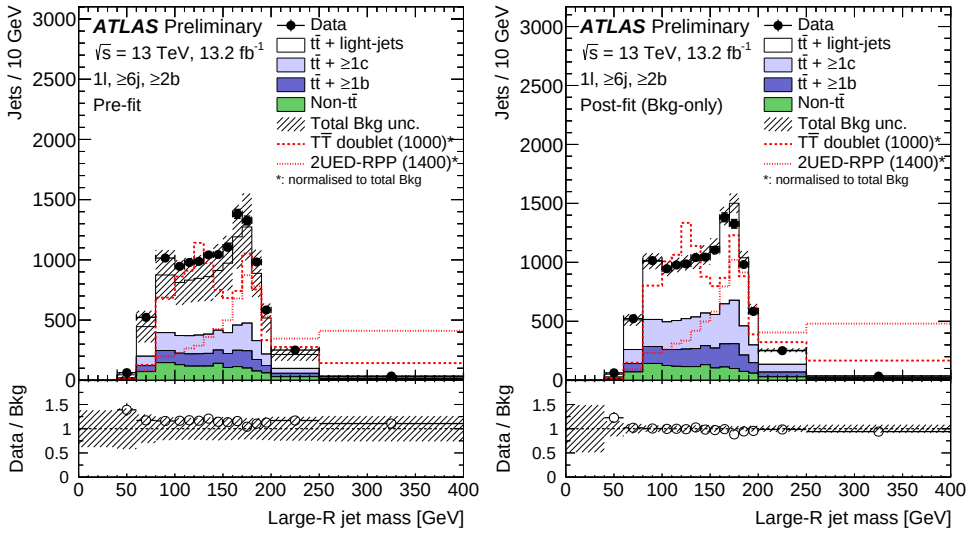

(a) (b)

Figure 26: Comparison between the data and prediction for the invariant mass distribution of selected large-R jets (prior to mass-tagging requirements) in the 1-lepton channel after preselection plus the requirement of ≥6 jets, (a) before and (b) after performing the combined fit to data in the 0-lepton and 1-lepton channels ("Pre-fit" and "Post-fit", respectively) under the background-only hypothesis. The small contributions from $t\bar{t}V$, $t\bar{t}H$, single top, W/Z+jets, diboson, and multijet backgrounds are combined into a single background source referred to as "Non-$t\bar{t}$". The expected signal distributions are shown, normalised to the total background prediction, for two scenarios considered in this search: $T\bar{T}$ production in the weak-isospin doublet scenario assuming $m_T = 1000$ GeV (red dashed histogram), and $t\bar{t}t\bar{t}$+X within the 2UED/RPP model assuming $m_{\mathrm{KK}} = 1400$ GeV (red dotted histogram). The last bin in all figures contains the overflow. The bottom panels display the ratios of data to the total background prediction ("Bkg"). The hashed area represents the total uncertainty on the background. In the case of the pre-fit background uncertainty, the normalisation uncertainty on the $t\bar{t}+ \geq 1b$ background is not included.

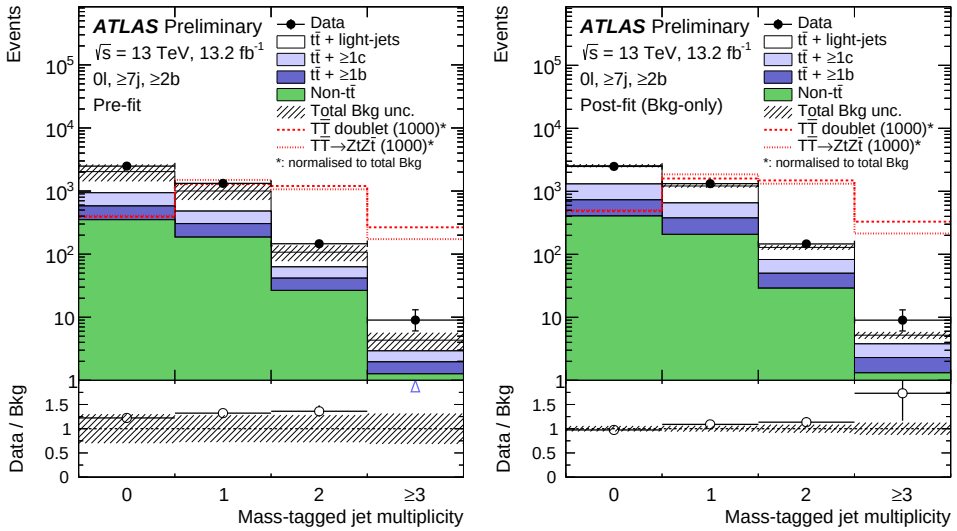

(a) (b)

Figure 27: Comparison between the data and prediction for the mass-tagged jet multiplicity distribution in the 0-lepton channel after preselection plus the requirement of ≥7 jets, (a) before and (b) after performing the combined fit to data in the 0-lepton and 1-lepton channels ("Pre-fit" and "Post-fit", respectively) under the background-only hypothesis. The small contributions from $t\bar{t}V$, $t\bar{t}H$, single top, W/Z+jets, diboson, and multijet backgrounds are combined into a single background source referred to as "Non-$t\bar{t}$". The expected signal distributions are shown, normalised to the total background prediction, for two scenarios considered in this search: $T\bar{T}$ production in the weak-isospin doublet scenario (red dashed histogram), and for BR($T \rightarrow Zt$) = 1 (red dotted histogram), both assuming m_T = 1000 GeV. The last bin in all figures contains the overflow. The bottom panels display the ratios of data to the total background prediction ("Bkg"). The blue triangles indicate points that are outside the vertical range of the figure. The hashed area represents the total uncertainty on the background. In the case of the pre-fit background uncertainty, the normalisation uncertainty on the $t\bar{t}+ \geq 1b$ background is not included.

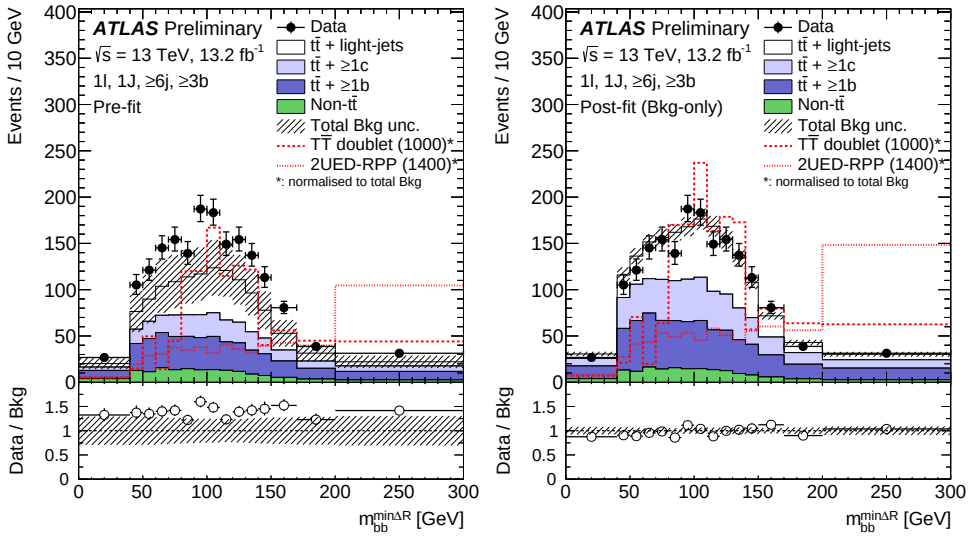

(a) (b)

Figure 28: Comparison between the data and prediction for the invariant mass distribution of the two b-tagged jets with lowest ΔR separation ($m_{bb}^{\min\Delta R}$) in the (1J, ≥6j, ≥3b) region of the 1-lepton channel, (a) before and (b) after performing the combined fit to data in the 0-lepton and 1-lepton channels ("Pre-fit" and "Post-fit", respectively) under the background-only hypothesis. The small contributions from $t\bar{t}V$, $t\bar{t}H$, single top, W/Z+jets, diboson, and multijet backgrounds are combined into a single background source referred to as "Non-$t\bar{t}$". The expected signal distributions are shown, normalised to the total background prediction, for two scenarios considered in this search: $T\bar{T}$ production in the weak-isospin doublet scenario assuming m_T = 1000 GeV (red dashed histogram), and $t\bar{t}t\bar{t}$+X within the 2UED/RPP model assuming m_{KK} = 1400 GeV (red dotted histogram). The last bin in all figures contains the overflow. The bottom panels display the ratios of data to the total background prediction ("Bkg"). The hashed area represents the total uncertainty on the background. In the case of the pre-fit background uncertainty, the normalisation uncertainty on the $t\bar{t}+\geq 1b$ background is not included.

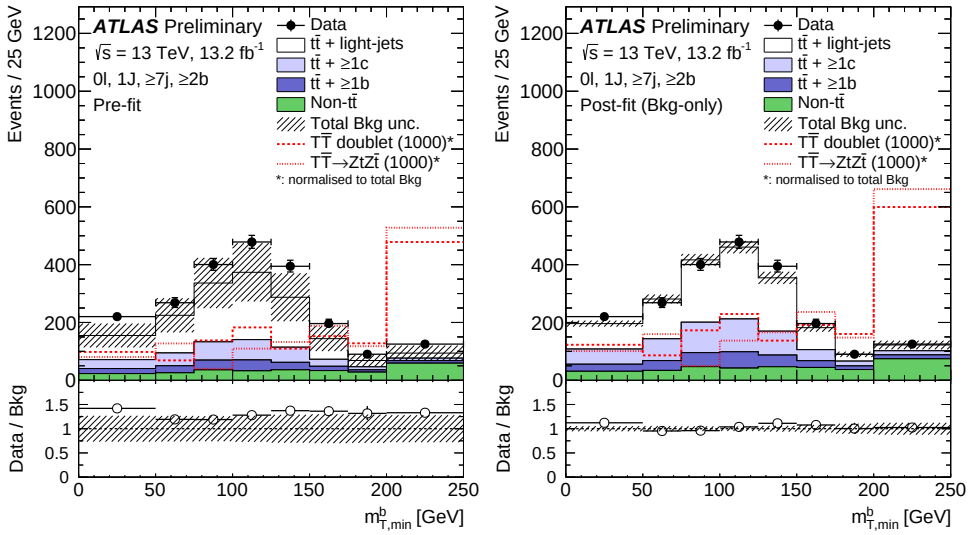

(a) (b)

Figure 29: Comparison between the data and prediction for the distribution of the minimum transverse mass between $E_{\mathrm{T}}^{\mathrm{miss}}$ and any of the three leading b-tagged jets in the event ($m^{b}_{\mathrm{T,min}}$) in the (1J, ≥7j, ≥2b) region of the 0-lepton channel (a) before and (b) after performing the combined fit to data in the 0-lepton and 1-lepton channels ("Pre-fit" and "Post-fit", respectively) under the background-only hypothesis. The small contributions from $t\bar{t}V$, $t\bar{t}H$, single top, W/Z+jets, diboson, and multijet backgrounds are combined into a single background source referred to as "Non-$t\bar{t}$". The expected signal distributions are shown, normalised to the total background prediction, for two scenarios considered in this search: $T\bar{T}$ production in the weak-isospin doublet scenario (red dashed histogram), and for BR($T \rightarrow Zt$) = 1 (red dotted histogram), both assuming m_T = 1000 GeV. The last bin in all figures contains the overflow. The bottom panels display the ratios of data to the total background prediction ("Bkg"). The hashed area represents the total uncertainty on the background. In the case of the pre-fit background uncertainty, the normalisation uncertainty on the $t\bar{t}+ \geq 1b$ background is not included.

B. Limits on $T\bar{T}$ production from individual searches

Figure 30 shows 95% CL upper limits on the $T\bar{T}$ production cross section as a function of the T quark mass obtained by the 1-lepton search for the weak-isospin doublet and singlet scenarios. Figure 31 shows the 95% CL exclusion limits on vector-like T quark production, for different values of m_T and as a function of the two branching ratios BR($T \to Wb$) and BR($T \to Ht$), obtained by the 1-lepton search. The corresponding mass exclusion limits can be found in Figure 32.

Figure 33 shows 95% CL upper limits on the $T\bar{T}$ production cross section as a function of the T quark mass obtained by the 0-lepton search for the weak-isospin doublet and singlet scenarios. Figure 34 shows the 95% CL exclusion limits on vector-like T quark production, for different values of m_T and as a function of the two branching ratios BR($T \to Wb$) and BR($T \to Ht$), obtained by the 0-lepton search. The corresponding mass exclusion limits can be found in Figure 35.

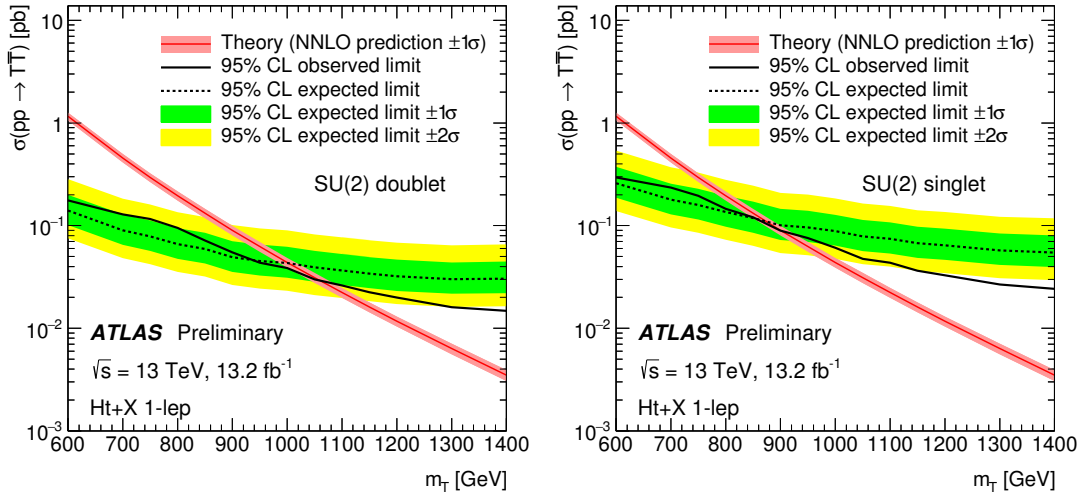

(a) (b)

Figure 30: Observed (solid line) and expected (dashed line) 95% CL upper limits on the $T\bar{T}$ cross section as a function of the T quark mass for the 1-lepton search (a) for a T quark doublet, and (b) for a T quark singlet. The surrounding shaded bands correspond to ±1 and ±2 standard deviations around the expected limit. The thin red line and band show the theoretical prediction and its ±1 standard deviation uncertainty.

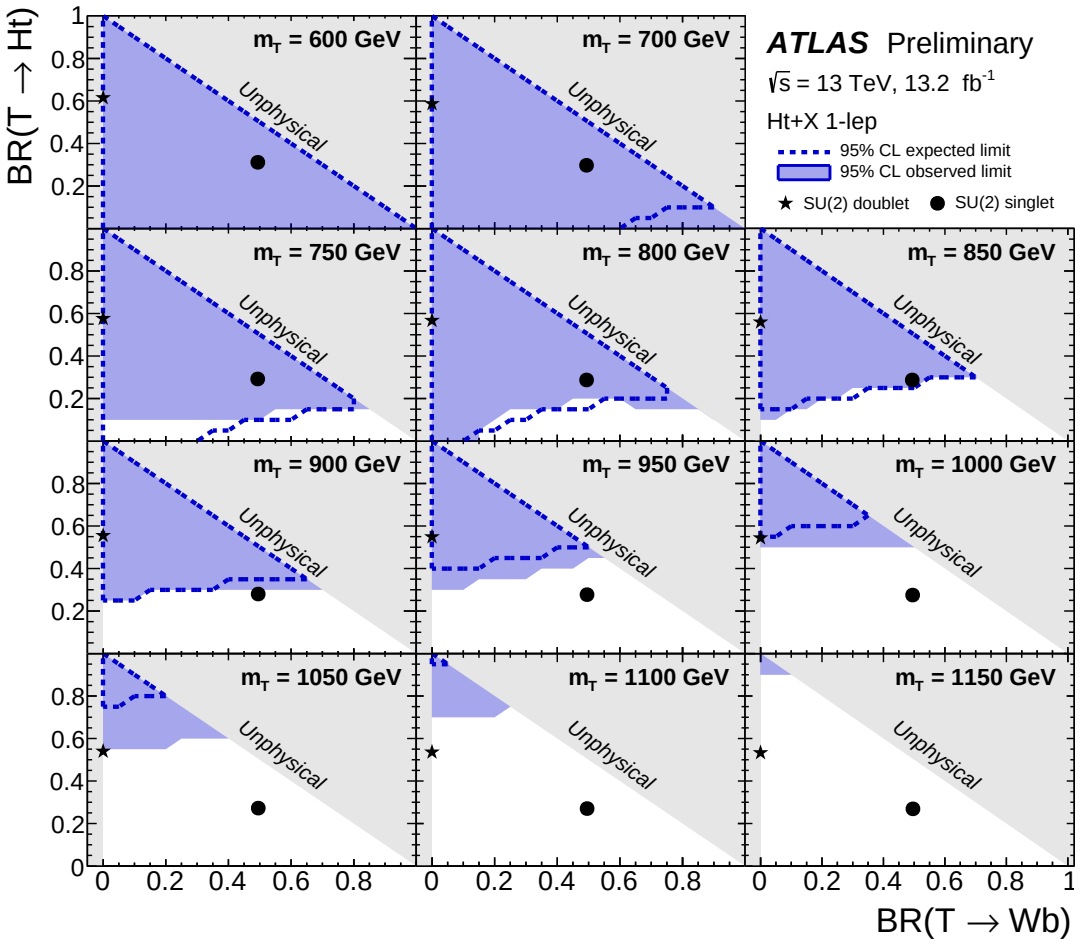

Figure 31: Observed (blue filled area) and expected (blue dashed line) 95% CL exclusion in the plane of BR($T \to Wb$) versus BR($T \to Ht$), for different values of the vector-like T quark mass for the 1-lepton search. The grey (light shaded) area corresponds to the unphysical region where the sum of branching ratios exceeds unity, or is smaller than zero. The default branching ratio values from the Protos event generator for the weak-isospin singlet and doublet cases are shown as plain circle and star symbols respectively.

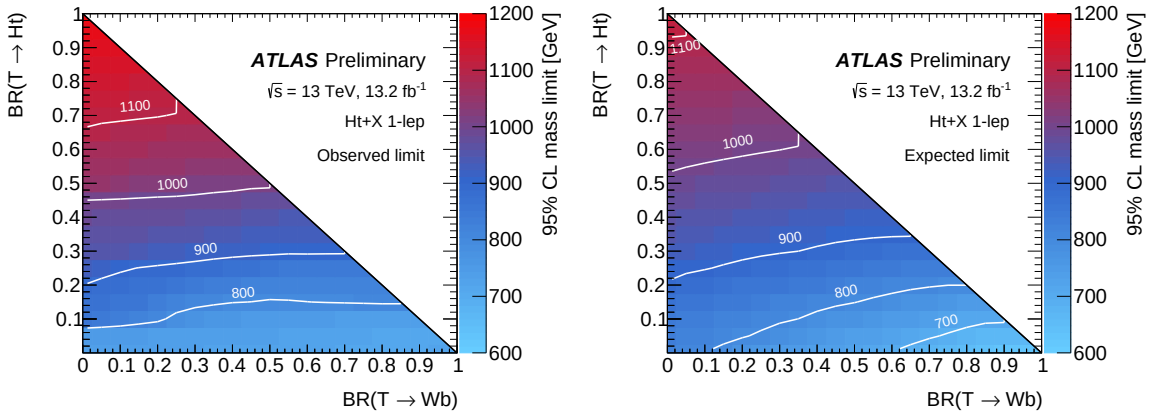

(a) (b)

Figure 32: (a) Observed and (b) expected limit (95% CL) on the mass of the T quark in the plane of BR($T \to Ht$) versus BR($T \to Wb$) for the 1-lepton search. Contour lines are provided to guide the eye.

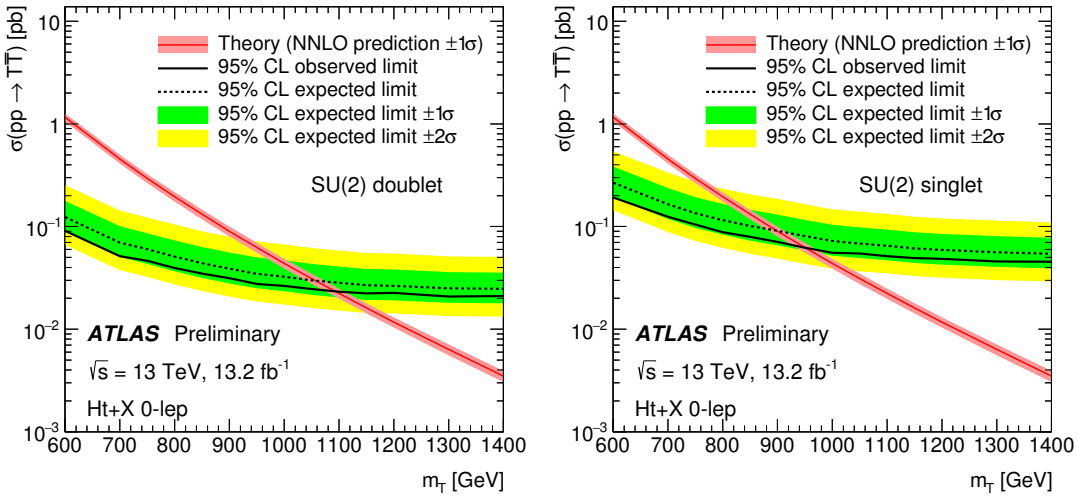

(a) (b)

Figure 33: Observed (solid line) and expected (dashed line) 95% CL upper limits on the $T\bar{T}$ cross section as a function of the T quark mass for the 0-lepton search (a) for a T quark doublet, and (b) for a T quark singlet. The surrounding shaded bands correspond to ±1 and ±2 standard deviations around the expected limit. The thin red line and band show the theoretical prediction and its ±1 standard deviation uncertainty.

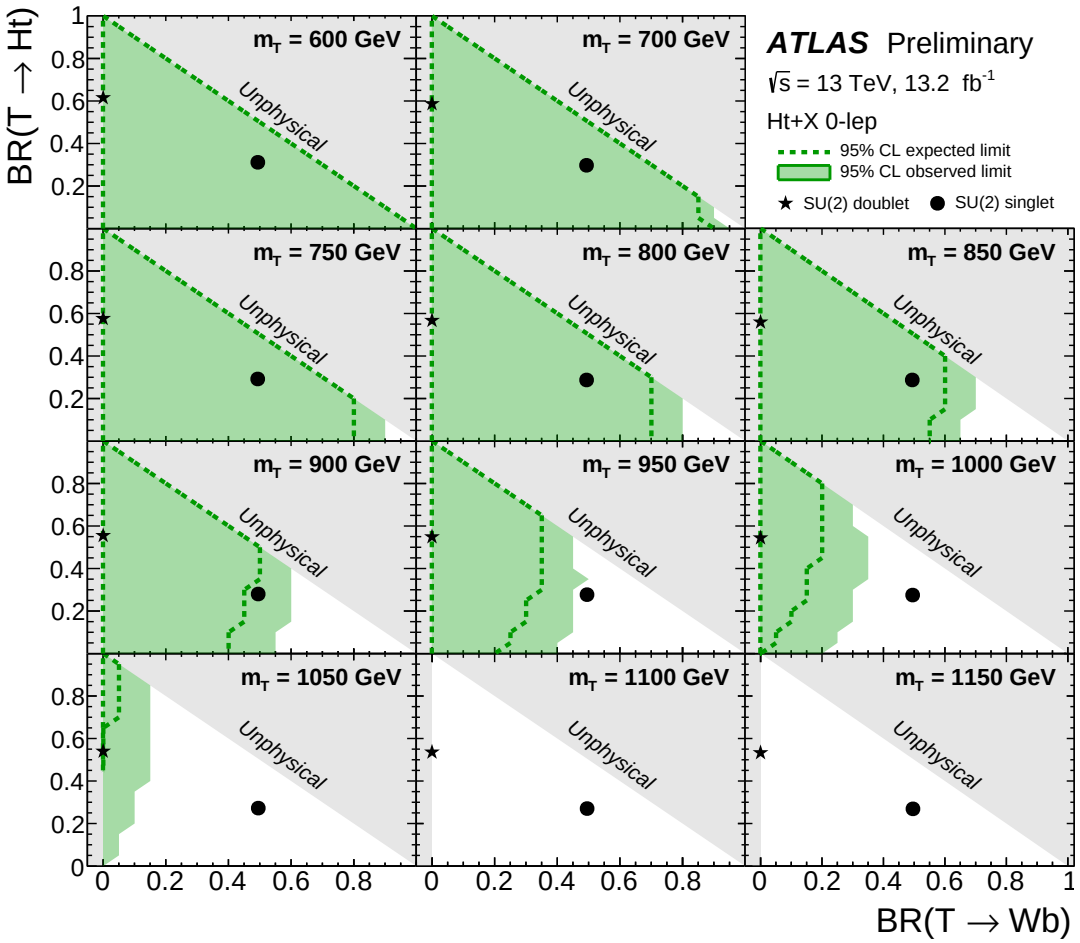

Figure 34: Observed (green filled area) and expected (green dashed line) 95% CL exclusion in the plane of BR($T \to Wb$) versus BR($T \to Ht$), for different values of the vector-like T quark mass for the 0-lepton search. The grey (light shaded) area corresponds to the unphysical region where the sum of branching ratios exceeds unity, or is smaller than zero. The default branching ratio values from the PROTOS event generator for the weak-isospin singlet and doublet cases are shown as plain circle and star symbols respectively.

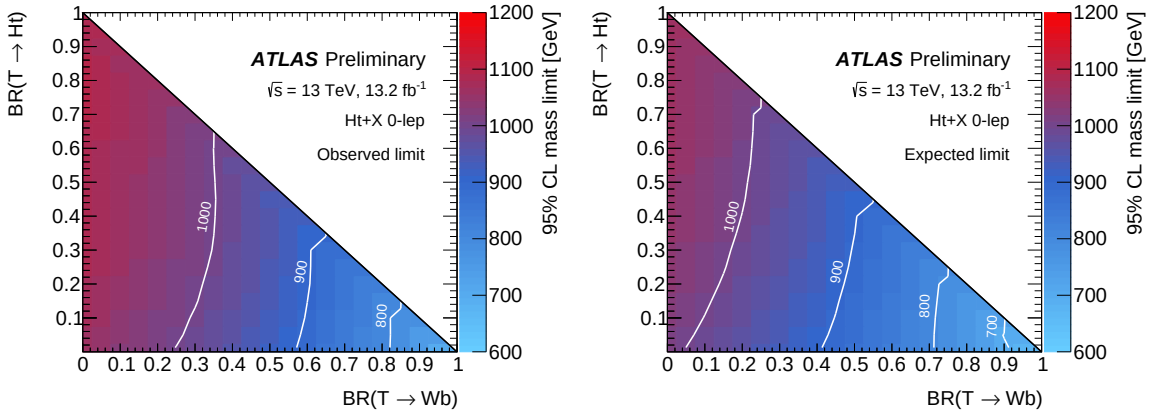

(a) (b)

Figure 35: (a) Observed and (b) expected limit (95% CL) on the mass of the T quark in the plane of BR($T \to Ht$) versus BR($T \to Wb$) for the 0-lepton search. Contour lines are provided to guide the eye.